

OPTIMIZATION OF NANOPARTICLE ARRAYS TO DESIGN EFFICIENT
COUPLERS FOR PLASMONIC NANOWIRE NETWORKS

A THESIS SUBMITTED TO
THE GRADUATE SCHOOL OF NATURAL AND APPLIED SCIENCES
OF
MIDDLE EAST TECHNICAL UNIVERSITY

BY

AŞKIN ALTINOKLU

IN PARTIAL FULFILLMENT OF THE REQUIREMENTS
FOR
THE DEGREE OF MASTER OF SCIENCE
IN
ELECTRICAL AND ELECTRONICS ENGINEERING

SEPTEMBER 2019

Approval of the thesis:

**OPTIMIZATION OF NANOPARTICLE ARRAYS TO DESIGN EFFICIENT
COUPLERS FOR PLASMONIC NANOWIRE NETWORKS**

submitted by **AŞKIN ALTINOKLU** in partial fulfillment of the requirements for the degree of **Master of Science in Electrical and Electronics Engineering Department, Middle East Technical University** by,

Prof. Dr. Halil Kalıpçılar
Dean, Graduate School of **Natural and Applied Sciences** _____

Prof. Dr. İlkay Ulusoy
Head of Department, **Electrical and Electronics Engineering** _____

Assoc. Prof. Dr. Özgür Ergül
Supervisor, **Electrical and Electronics Engineering, METU** _____

Examining Committee Members:

Prof. Dr. Şimşek Demir
Electrical and Electronics Engineering, METU _____

Assoc. Prof. Dr. Özgür Ergül
Electrical and Electronics Engineering, METU _____

Prof. Dr. Vakur Behçet Ertürk
Electrical and Electronics Engineering, Bilkent University _____

Assoc. Prof. Dr. Lale Alatan
Electrical and Electronics Engineering, METU _____

Assoc. Prof. Dr. Fatih Dikmen
Electronics Engineering, Gebze Technical University _____

Date:

I hereby declare that all information in this document has been obtained and presented in accordance with academic rules and ethical conduct. I also declare that, as required by these rules and conduct, I have fully cited and referenced all material and results that are not original to this work.

Name, Surname: Aşkın Altınoklu

Signature :

ABSTRACT

OPTIMIZATION OF NANOPARTICLE ARRAYS TO DESIGN EFFICIENT COUPLERS FOR PLASMONIC NANOWIRE NETWORKS

Altınoklu, Aşkın

M.S., Department of Electrical and Electronics Engineering

Supervisor: Assoc. Prof. Dr. Özgür Ergül

September 2019, 141 pages

In this thesis, a novel optimization strategy for design and optimization of efficient couplers to improve nano-optical links in complex plasmonic nanowire networks is presented. Various cases involving alternative combinations of nanowire transmission lines with different types and lengths are considered. As the optimization environment, a full-wave solver based on surface integral equations and the multilevel fast multipole algorithm (MLFMA) developed for efficient and accurate solutions of plasmonic problems is integrated with a heuristic optimization method based on genetic algorithms. Efficient designs of nano-couplers for different isolated scenarios involving bent and straight nanowires are obtained to build large nano-optical systems and networks involving nanowires and optimized nano-couplers. Usage of multiple couplers and their integration on the same transmission line are studied in detail. The performances of the designed couplers are examined in many aspects, including comparisons with the classical approaches known in the literature. In addition to the design of effective nano-couplers to improve optical transmission via nanowire systems, several guidelines and conclusions are provided for the efficient

usage of the designed nano-couplers while constructing complex nanowire networks and nano-optical links.

Keywords: Plasmonics, Nano-Particle Arrays, Nanowires, Multilevel Fast Multipole Algorithm, Genetic Algorithms

ÖZ

PLAZMONİK NANOTEL İLETİM AĞLARINDA KULLANILABİLECEK ETKİN BAĞLAŞTIRICI TASARIMLARI İÇİN NANOPARÇACIK DİZİSİ OPTİMİZASYONLARI

Altınoklu, Aşkın

Yüksek Lisans, Elektrik ve Elektronik Mühendisliği Bölümü

Tez Yöneticisi: Doç. Dr. Özgür Ergül

Eylül 2019 , 141 sayfa

Bu tezde, karmaşık yapılarıdaki plazmonik nanotel iletim ağlarında bulunan nano-optik bağlantıların iyileştirilmesinde kullanılabilecek verimli bağlaştırmaların tasarım ve optimizasyonları için özgün bir optimizasyon stratejisi sunulmuştur. Farklı tiplerdeki ve uzunluklardaki nanotel iletim hatlarının çeşitli şekillerde bağlandığı durumlar ele alınmıştır. Optimizasyon mekanizması, plazmonik özellikteki elektromanyetik problemlerin etkin ve doğru bir biçimde çözülmesi için özel olarak geliştirilen, yüzey integral denklemleri ve çok seviyeli hızlı çokkutup yöntemine (ÇSHÇY) dayanan bir tam-dalga çözücüsü ile genetik algoritmalara dayalı bir keşifsel optimizasyon metodunun birleştirilmesi sonucu elde edilmiştir. Bükümlü ve düz nanoteller gibi farklı durumlar için elde edilen etkin bağlaştırmaları, farklı tiplerdeki nanotelleri ve optimize edilmiş bağlaştırmaları içeren daha büyük ve karmaşık nano-optik sistemlerin ve ağların oluşturulmasında kullanılmıştır. Farklı durumlar için tasarlanmış olan bağlaştırmaların beraber aynı nanotel iletim ağlarında kullanılmaları detaylı bir şekilde incelenmiştir. Bağlaştırmaların sağladığı performanslar, literatürde bilinen klasik

metotlar ile karřılařtırmaları da içerecek biçimde farklı açılardan detaylı bir şekilde incelenmiştir. Çalışma kapsamında, nanotel sistemlerinde optik iletimin artırılmasını sağlayan etkin bağlařtırıcı tasarımlarının ortaya konmasının yanı sıra, tasarlanan bağlařtırıcıların karmařık nanotel iletim ađları ve nano-optik linklerin oluşturulmasında etkin olarak kullanımları dođrultusunda izlenmesi gereken kurallar belirlenmiştir.

Anahtar Kelimeler: Plazmonik, Nano-Parçacık Dizisi, Nanoteller, Çok Seviyeli Hızlı Çokkutup Yöntemi, Genetik Algoritmalar

To my mother, my father, my brother and my friends...

ACKNOWLEDGMENTS

I would first like to express my profound gratitude to my supervisor Assoc. Prof. Dr. Özgür Ergül. He is the one that shapes my academic career with his invaluable guidance and suggestions during all my undergraduate and graduate studies. His motivation and passion has made me doing my best that I can do. I will be eternally grateful to him for everything that he does for me.

I would like to specially thank Dr. Alper Kürşat Öztürk for everything that he taught me. It was an awesome chance for me to work with a scientist like him as an early career engineer.

I also would like to gratefully thank Assoc. Prof. Fatih Dikmen, Assoc. Prof. Lale Alatan, Prof. Dr. Şimşek Demir and Prof. Dr. Vakur Behçet Ertürk for participating in my thesis committee and for their contributions to my thesis.

I would like to express my deepest gratitude to all my teachers and professors for their invaluable contributions to me during my education journey starting from primary school to university.

I would like to thank former and current researchers of CEMMETU for their cooperation and participation in my studies.

I also thank ASELSAN for providing me constant support throughout my graduate study, and the Scientific and Technical Research Council of Turkey (TUBITAK) for its support to this work through a M.S. scholarship.

I would like to express my heartfelt thanks to Hande İbili and Sena Alkış for their invaluable friendship and unfailing support that makes my life easier while facing the challenges during this work.

Last but not least, I would like to thank my family for making me feel stronger and always being there for me.

TABLE OF CONTENTS

ABSTRACT	v
ÖZ	vii
ACKNOWLEDGMENTS	x
TABLE OF CONTENTS	xi
LIST OF TABLES	xv
LIST OF FIGURES	xvi
LIST OF ABBREVIATIONS	xxiv
CHAPTERS	
1 INTRODUCTION	1
2 FULL-WAVE ELECTROMAGNETIC SOLVER FOR PLASMONIC AP- PLICATIONS	7
2.1 Introduction	7
2.2 General View of the Simulation Environment	7
2.3 Method of Moments and Discretization	9
2.4 MLFMA	11
2.5 Surface Formulations	12
2.6 Iterative Solutions and Preconditioning	21
2.7 Excitation	23

2.8	Field and Power Calculations	23
2.9	Remarks	24
3	OPTIMIZATION MECHANISM FOR THE DESIGN OF NANOPARTICLE ARRAYS	27
3.1	Introduction	27
3.2	Overall Structure	27
3.3	GAs and Related Definitions	30
3.4	Efficient and Integrated Combination of the Full-Wave Solver with GAs for the Optimization of Couplers	33
3.5	Remarks	35
4	OPTIMIZATION OF NANOPARTICLE COUPLERS FOR NANO-OPTICAL NETWORKS	37
4.1	Introduction	37
4.2	Parameters Related to Electromagnetic Simulations	39
4.3	Design of Efficient Input Couplers	42
4.3.1	Power Transmission through Straight Nanowires	45
4.3.2	Design of ICs for Different Layouts	47
4.3.3	Investigation of the Performance of the Optimized IC (IC1)	51
4.3.4	Design of ICs with Symmetrical Configurations	55
4.3.5	Performances of Full Arrays as ICs	58
4.3.6	Compatibility of the Optimized ICs for Different Lengths of Straight Nanowires	59
4.3.7	Frequency Response of the Optimized ICs	60
4.4	Design of Efficient Couplers for Improving Transmission Through Sharp Bends	62

4.4.1	Details Related to Optimization of CCs	63
4.4.2	Power Transmission Abilities of Bent Nanowires with Sharp Bends	64
4.4.3	Design of CCs to Improve Power Transmission Through Sharp Bends	66
4.4.4	Effect of Geometrical Properties on the Performance of CCs	70
4.4.5	Design of CCs by Using Different Types of Nanoparticles	73
4.4.6	Performance of the Optimized CCs for Different Nanowire Lengths	78
4.4.7	Performances of CCs in Comparison to Smooth Bends	79
4.5	Analysis and Optimization of Multiple Couplers	86
4.5.1	Compatibility of Separately Designed Couplers	88
4.5.2	Optimization of ICs for the Bent Nanowires	91
4.5.3	Design of Input and Corner Couplers via a Simultaneous Optimization	96
4.6	Design of Efficient Couplers for Different Types of Junction Problems	98
4.6.1	Details Related to the Optimization of Junction Couplers	99
4.6.2	Design of Couplers for a Three-way Junction with Two Symmetrically Located Outputs	101
4.6.3	Design of Couplers for a Three-way Junction with Two Differently Oriented Outputs	105
4.6.4	Design of Couplers for a Four-way Junction with Three Outputs	108
4.7	Building Complex Nanowire Networks Involving Nanowires and Optimized Couplers	112
4.8	Sensitivity Analysis for the Optimized Couplers	128
4.9	Remarks	131

5 CONCLUSIONS	133
REFERENCES	137

LIST OF TABLES

TABLES

Table 4.1	Parameters Related to the Nanowires and Excitation	41
Table 4.2	Parameters Related to the Full-wave Solver	42
Table 4.3	Parameters Related to GAs	42
Table 4.4	Computational Load For the Optimization of ICs and CCs in Different Scenarios	98
Table 4.5	The Results For the Sensitivity Analysis of IC2	128
Table 4.6	The Results For the Sensitivity Analysis of CC2	129
Table 4.7	The Results For the Sensitivity Analysis of YC1	129
Table 4.8	The Results For the Sensitivity Analysis of TC1	130
Table 4.9	The Results For the Sensitivity Analysis of PC1	130

LIST OF FIGURES

FIGURES

Figure 1.1	Some examples of different nano-link systems.	3
Figure 2.1	Diagram of the constructed simulation environment.	8
Figure 2.2	Diagrams for the main stages of the MLFMA program.	13
Figure 2.3	Boundaries between two dielectric regions.	15
Figure 3.1	Diagram for the stages of the optimization mechanism.	28
Figure 3.2	Block diagram for standard GAs.	31
Figure 3.3	Block diagram for the efficient integration of the MLFMA solver with GAs.	34
Figure 4.1	Coupler design problems and an illustration of their integration to build a large nanowire network.	38
Figure 4.2	Illustration of some parameters related to the electromagnetic simulations and optimization trials.	39
Figure 4.3	A pair of nanowires considered in IC optimization trials and the corresponding measurement (optimization) frame, in which power density values are computed.	44
Figure 4.4	Electric field intensity, magnetic field intensity, and power den- sity for different regions and in the output frames when straight nanowires of 5 μm are excited via Hertzian dipoles at 250 THz.	46

Figure 4.5	Effect of optimization layouts on the designs of ICs. Optimization histories for six different cases and the corresponding layouts are given.	48
Figure 4.6	Power density distributions for different cases involving no coupler (case 0), optimized ICs for six different layouts (cases 1, 2, 4, 5, 6, 7), and a modified version of the optimized coupler of case 2 (case 3).	49
Figure 4.7	Importance graph (effect of each nanoparticle in IC1 on the fitness).	52
Figure 4.8	Power density distributions for two modified couplers corresponding to the inversion of the least and most important bits, in comparison to the original case.	53
Figure 4.9	Power density distributions for six modified couplers obtained either by eliminating some of the nanocubes (cases 1–4) or symmetrizing the array (cases 5 and 6) of IC1.	54
Figure 4.10	Optimization history for the trial performed by enforcing the symmetry of the coupler (IC2), in comparison to the history for IC1 (see Figure 4.6, case 7). Corresponding optimization layouts and the optimized configurations are shown on the right-hand side.	56
Figure 4.11	Power density distributions when IC1 and IC2 are attached to the straight nanowires shown in Figure 4.6, in comparison to the no-coupler case.	57
Figure 4.12	Power density distributions when the full arrays corresponding to the layouts of IC1 and IC2 are used as couplers, in comparison to the no-coupler case.	58
Figure 4.13	Performance of IC2 for different lengths of straight nanowires.	60
Figure 4.14	Performances of IC1 and IC2 in a range of frequencies from 200 THz to 300 THz.	61

Figure 4.15	A pair of nanowires with 90° sharp bends considered in CC optimization trials and the corresponding measurement (optimization) frame, in which the power density values are computed.	64
Figure 4.16	Electric field intensity, magnetic field intensity, and power density distributions in different regions when a pair of 10 μm bent nanowires involving 90° sharp bends is excited via Hertzian dipoles at 250 THz. . .	65
Figure 4.17	Optimization histories for two trials using different cost functions, the optimization layout, and the obtained configurations for the designs after 200 generations.	67
Figure 4.18	Electric field intensity along the nanowire-vacuum interface for different cases involving bent nanowires.	68
Figure 4.19	Power density distributions in different regions, when CC1 and CC2 are integrated into the corner region of the bent nanowires, in comparison to the no-coupler case.	69
Figure 4.20	Power density distributions in different regions, when the height of the particles of CC1 is altered from 90 nm to 30 nm, 60 nm, 120 nm, and 240 nm.	70
Figure 4.21	Power density distributions when the nearby nanoparticles in the optimal design CC1 are combined, in comparison to the original results.	71
Figure 4.22	Power density distributions when the optimal arrangement of CC1 is used for different nanoparticle geometries.	72
Figure 4.23	Starting layouts for the optimization trials, which are performed for four different types of nanoparticles.	74
Figure 4.24	Power density distributions for the optimized couplers using different types of nanoparticles, which are designed with the aim of increasing (a) maximum and (b) mean power density in the output frame.	75

Figure 4.25	Performances of the designed CCs, which involve four different types of nanoparticles to improve the mean power density in the output frame, in a range of frequencies from 200 THz to 300 THz.	76
Figure 4.26	Performance of CC1 with different lengths of nanowires (5 μm , 10 μm , 20 μm). Power density distributions are shown for the cases (a) without a coupler and (b) with CC1.	77
Figure 4.27	Variation of the mean power density in the output frames with respect to the length of the first segment of the bent nanowires for cases without coupler, with CC1, and with CC2.	79
Figure 4.28	(a) A pair of nanowires involving a 90° sharp bend and (b) a pair of nanowires involving a curved bend with a radius of curvature (R). . .	80
Figure 4.29	Variation of the mean and maximum power density in the output (measurement) frame with respect to the bending radius of curved nanowires.	81
Figure 4.30	Power density distributions for different cases involving curved nanowires with different values of bending radius in a range from 0.4 μm to 5.0 μm : (a) Transversal planes bisecting geometries and (b) the output frame.	82
Figure 4.31	Power density distributions in three different frames for curved nanowires with $R= 0.5 \mu\text{m}$, 1.7 μm , 2.8 μm , and 5.0 μm in comparison to the results for nanowires with 90° sharp bends.	83
Figure 4.32	Results regarding the integration of CC1 into the pair of curved nanowires with a bending radius of 0.4 μm	84
Figure 4.33	Geometric details for the curved nanowires with a bending radius of 0.4 μm , on which CCs are designed via optimization.	85
Figure 4.34	Coupler designs with the corresponding power-density results, which are designed for the pair of curved nanowires shown in Figure 4.33.	86

Figure 4.35	A nanowire system involving several coupler regions.	87
Figure 4.36	IC and CC designs used in the tests presented in Figure 4.37. . .	89
Figure 4.37	Power density distributions for different cases corresponding to different combinations of ICs and CCs into the coupler regions of the bent nanowires shown in Figure 4.35.	90
Figure 4.38	The nanowire geometries used for the optimization of different types of ICs, i.e., IC1, IC3, and IC4.	91
Figure 4.39	Couplers IC1, IC2, and IC3 that are designed for different sce- narios. Optimization histories are shown with different levels (empty, full, and the best configuration in the initial pool).	92
Figure 4.40	Power density results for the different cases involving differ- ent combinations of IC1, IC3, IC4, and CC1 into the system of bent nanowires.	93
Figure 4.41	Power density distributions for the cases when IC1, IC3, and IC4 are integrated into the input region of the 5 μm straight nanowires. .	95
Figure 4.42	Layouts and ultimate configurations for IC5 and CC3 when they are designed simultaneously.	96
Figure 4.43	Power density distributions for several cases involving different configurations of ICs and CCs.	97
Figure 4.44	Three different types of junctions involving 5 μm nanowire seg- ments: (a) Three-way junction with two symmetrically located outputs, (b) three-way junction with two differently oriented outputs, and (c) four-way junction with three outputs (dimensions of the geometries are also given).	99
Figure 4.45	T-shaped nanowire system involving a three-way junction with two symmetrically located outputs. Full array layout used for the op- timization of the junction coupler and the final design (TC1) are also shown.	101

Figure 4.46	Performance of TC1 in comparison to the no-coupler and full-array cases. Power density distributions in three different frames and the geometries for all cases are shown.	102
Figure 4.47	Performance of TC1 together with IC1 and IC2.	104
Figure 4.48	Importance graph for TC1. Power density distributions in one of the output frames are also shown for two modified couplers corresponding to the inversion of the least and most important bits, in comparison to the original case.	104
Figure 4.49	Y-shaped nanowire system involving a three-way junction with two differently oriented outputs. Full array layout used for the optimization of the junction coupler and the final design (YC1) are also shown.	105
Figure 4.50	Performance of YC1 in comparison to the no-coupler and full-array cases. Power density distributions in three different frames and the geometries for all cases are shown.	106
Figure 4.51	Performance of YC1 together with IC2.	107
Figure 4.52	Importance graph for YC1. Power density distributions in the output frames are also shown for two modified couplers corresponding to the inversion of the least and most important bits, in comparison to the original case.	108
Figure 4.53	Plus-shaped nanowire system involving a four-way junction with three outputs. Full array layout used for the optimization of the junction coupler and the final design (PC1) are also shown.	109
Figure 4.54	Performance of PC1 in comparison to the no-coupler and full-array cases. Power density distributions in three different frames and the geometries for all cases are shown.	110
Figure 4.55	Performance of PC1 together with IC2. The power density distribution for the entire system involving both PC1 and IC2 is also shown.	111

- Figure 4.56 Results for the first nano-optical system. Power density distributions in different regions and in the output frame for different configurations of three couplers (IC2 and two CC2) are depicted. The geometry of the nanowire system and the used couplers are also shown. 113
- Figure 4.57 Results for the second nano-optical system. Power density distributions in different regions and in the output frames for different configurations of four couplers (IC2, TC1, and two CC2) are shown. The geometry of the nanowire system and the used couplers are also shown. 115
- Figure 4.58 Results for the third nano-optical system. Power density distributions in different regions and in the output frames for different configurations of three couplers (IC2, YC1, and CC2) are shown. The geometry of the nanowire system and the used couplers are also shown. 118
- Figure 4.59 Results for the fourth nano-optical system. Power density distributions in different regions and in the output frames for different configurations of five couplers (IC2, YC1, PC1, TC1, and CC2) are shown. The entire system with the integration of all couplers is shown separately. 120
- Figure 4.60 Results for the fifth nano-optical system. Power density distributions in different regions and in the output frames for different configurations of two couplers (IC2 and YC1) are shown. The entire system with the integration of both couplers is shown separately. 122
- Figure 4.61 Results for the sixth nano-optical system. Power density distributions in different regions and in the output frames for different configurations of four couplers (IC2, TC1, and two YC1) are shown. The entire system with the integration of all couplers is shown separately. . . 123
- Figure 4.62 Results for the seventh nano-optical system. Power density distributions in different regions and in the output frames for different configurations of four couplers (IC2, YC1, and two CC2) are shown. The entire system with the integration of all couplers is shown separately. . . 124

- Figure 4.63 Results for the eighth nano-optical system. Power density distributions in different regions and in the output frames for different configurations of three couplers (IC2, PC1, and TC1) are shown. The entire system with the integration of all couplers is shown separately. 125
- Figure 4.64 Results for the ninth nano-optical system. Power density distributions in different regions and in the output frames for different configurations of three couplers (IC2 and two PC1) are shown. The entire system with the integration of all couplers is shown separately. 126
- Figure 4.65 Results for the tenth nano-optical system. Power density distributions in different regions and in the output frames for different configurations of three couplers (IC2 and two PC1) are shown. The entire system with the integration of all couplers is shown separately. 127

LIST OF ABBREVIATIONS

AMLFMA	Approximate multilevel fast multipole algorithm
CC	Corner coupler
CTF	Combined tangential formulation
EFIE	Electric-field integral equation
FMGRES	Flexible generalized minimal residual (method)
FMM	Fast multipole method
GA	Genetic algorithm
GMRES	Generalized minimal residual (method)
IC	Input coupler
JMCFIE	Electric and magnetic current combined-field integral equation
MCTF	Modified combined tangential formulation
MFIE	Magnetic-field integral equation
MLFMA	Multilevel fast multipole algorithm
MoM	Method of moments
MVM	Matrix-vector multiplication
PC	Plus-shaped junction coupler
PMCHWT	Poggio-Miller-Chang-Harrington-Wu-Tsai
RWG	Rao-Wilton-Glisson (function)
SPP	Surface-plasmon-polariton
TC	T-shaped junction coupler
YC	Y-shaped junction coupler

CHAPTER 1

INTRODUCTION

Nanowires have attracted considerable interest with their enhanced capabilities to transmit electromagnetic power and control information processing throughout complex nano-optical systems. Thanks to the plasmonic properties of metals, nanowires are considered as good alternatives to dielectric structures, whose dimensions are mostly restricted by the wavelength due to the diffraction limit, for a plethora of applications at optical frequencies including visible, infrared, and UV regions of the spectrum [1].

Nanowires composed of metallic materials, such as gold (Au) or silver (Ag), provide efficient transmission of electromagnetic waves for electrically long distances via surface-plasmon-polaritons (SPPs), which are caused by excessive oscillations of free electrons of metals. The evanescent wave nature of SPPs in the direction perpendicular to metal-dielectric interfaces leads to efficiently guided waves along nanowire surfaces with tight confinement. This ability of localizing electromagnetic energy flow in nanometer scales has turned out to be an opportunity for the miniaturization of devices in nano-optical systems. In addition, with plasmonic properties, nanowires can provide efficient transmission, while keeping the cross-talks with the surrounding devices at minimum levels [2, 3]. With all these advantages, plasmonic nanowires, especially with straight geometries, are among the common components of many nano-optical systems constructed for diverse applications, such as communication, energy harvesting, imaging and sensing [1–10].

Working principles of straight and plasmonic nanowires can be explained in four steps. First, they are excited from their tips by one of the well-known methods, such as electron beam focusing [11], laser beam focusing [5, 12] or near-field emitters [13, 14].

Second, as a result of the excitation, depending on the nanowire parameters, such as length, width and height ratios, shape of the cross section, as well as the type of the excitation, the supported propagating modes and evanescent modes of surface plasmons are generated along metallic surfaces. Third, the generated propagating modes of surface plasmons travel along the longitudinal axis of nanowires while wave amplitudes of propagating fields exponentially decay in a direction perpendicular to the surface. Finally, electromagnetic fields transmitted along nanowires are radiated from the end tips [6]. Considering the working principles of straight plasmonic nanowires, several research studies have been performed to improve their electromagnetic performances, such as related to propagation loss, confinement ratio, coupling between source to surface plasmons, and efficiency for the radiation of surface plasmons at the abrupt ends of nanowires [3, 13, 15].

Recently, as the technology advances, the need for scaling down electron devices arises, and the ability of nanowires for efficient transmission and field localization regardless of diffraction limit of optical waves makes them significant components of nano-optical networks, such as plasmonic integrated circuits, modulators, and logic gates [1, 16]. In such types of real-life applications, connections of multiple straight nanowires and bends at some certain points of nanowires have turned out to be inevitable to construct complex networks in more compact and efficient ways. Despite their enhanced abilities to transmit electromagnetic power at optical frequencies, nanowire networks with junctions, which are constructed by using connections and combinations of several straight nanowires or sharp bends, suffer from several major problems due to electromagnetic responses of plasmons at junction and bending regions. Moreover, nano-optical systems with different numbers and types of junctions and bends may be desired to create different numbers of output ports as illustrated in Figure 1.1.

Although bends and junctions may react to propagation modes of SPPs in different ways, they both result in significant deterioration on the electromagnetic power transmission with undesired escape of energy to host media [7, 17]. Moreover, when nanowire systems, such as nanowire pairs are excited for transferring information, bends and junctions may result in corruption of transferred information due to undesired phase differences between propagating waves along several nanowires.

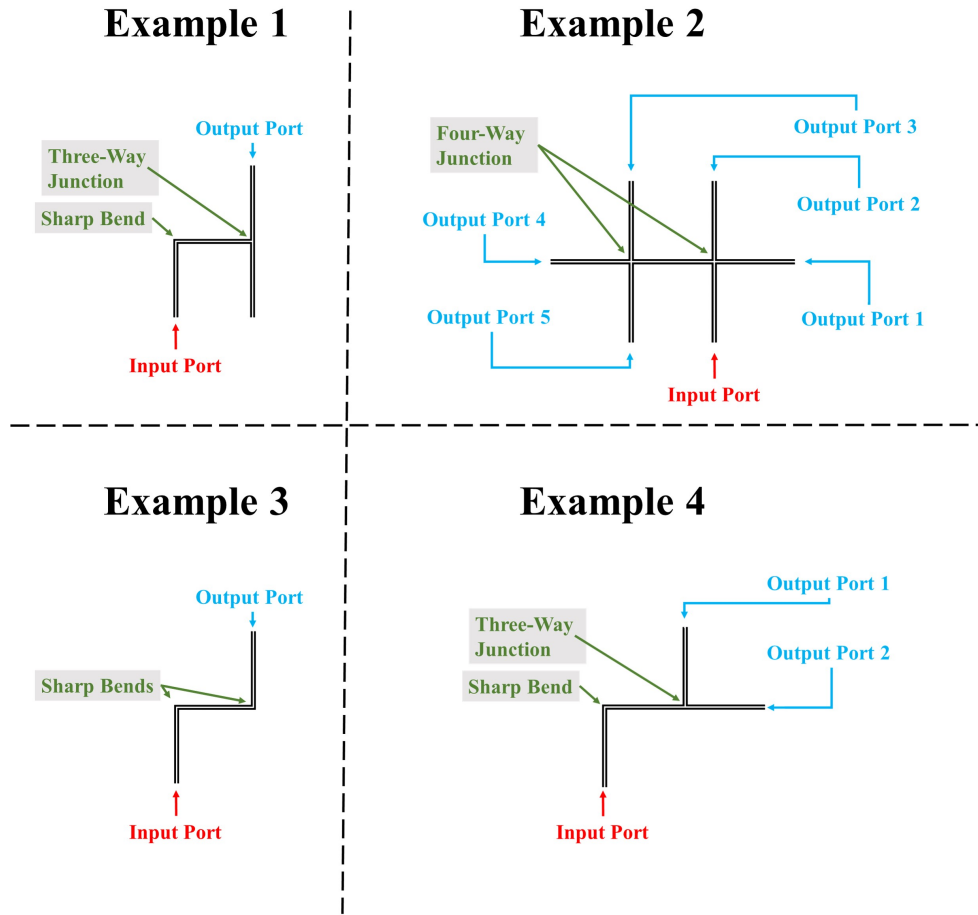


Figure 1.1: Some examples of different nano-link systems.

Previously, it was shown that when nanoparticles are placed close to each other, their strong interior interactions due to plasmonic properties can lead to useful abilities for various applications [17–20]. Considering all their advantages, such types of nanoparticle arrays can be used to design nano-couplers for complex nano-optical links.

The main purpose of this thesis is to present computational design and investigation of nano-optical systems involving nanowires and well-designed nano-couplers to effectively transmit and distribute electromagnetic power in nanometer scales. Designing nano-couplers, which consist of optimal arrangements of nanoparticles, with satisfactory performances for a target parameter is a challenging process that requires the investigation of several parameters related to the electromagnetic problem. There may be plenty of possible solutions for different parameters so that the analysis of all possible solutions to achieve the target properties is not feasible due to lack of

time and computational sources. Therefore, an efficient optimization tool, which is an integrated combination of genetic algorithms (GAs) and the multilevel fast multipole algorithm (MLFMA), is proposed for designing rigorous couplers composed of different arrangements of nanoparticles to control and guide optical waves throughout nanowire networks with complex junctions and bends. The optimization tool is utilized to design different nano-couplers for various scenarios, e.g., nanowire lines with sharp corners and junctions. The designed couplers are investigated in detail in terms of different parameters, and their performances are assessed by comparing them with the classical approaches known in the literature to improve transmission abilities of nanowires. Usage of multiple couplers and their integration within the same system are also studied, and combinations of multiple nano-couplers and nanowires to build larger nano-optical systems with different shapes, inputs, and outputs are considered. The results are interpreted to reach conclusions and guidelines on the design of effective couplers for complex nanowire networks and nano-optical links. The contributions and proposed ideas in this study can be listed as follows:

- An efficient optimization environment is implemented based on GAs supported by fast full-wave solutions to efficiently and accurately obtain effective couplers in alternative scenarios.
- In order to perform electromagnetic solutions efficiently without sacrificing accuracy, a full-wave solver based on surface integral equations and efficient implementation of MLFMA that is particularly developed for plasmonic structures is presented.
- A novel idea is proposed and supported by extensive analysis results to design couplers in order to improve coupling between sources and nanowires, while its advantages against the classical approaches in the literature are also demonstrated.
- Power transmission abilities of bent nanowires involving sharp bends are extensively examined, and novel designs of couplers are generated to improve the power transmission by decreasing electromagnetic losses due to reflections and diffractions at the bend regions. Performances of the couplers are evaluated in comparison to the techniques known in the literature, such as bend curving.

- Coupler designs for different types of junctions of nanowires are investigated to provide efficient and well-balanced transfer of electromagnetic power from one input to the desired output or outputs.
- Different arrangements and combinations of couplers, which are designed for isolated scenarios, are utilized to build larger systems, such as nanowire networks, for efficient transfer of electromagnetic power from input to the desired output or outputs.
- Rules and guidelines are given to achieve efficient connections between nanowire segments with the help of the designed couplers that can be useful while designing complex nanowire networks and nano-optical systems.

The organization of the thesis is as follows: In Chapter 2, a typical electromagnetic problem of this study, and the simulation environment used for fast and accurate solutions of this kind of a problem are presented. In Chapter 3, stages for the optimization of nano-couplers are explained step by step, the optimization tool used for this purpose is presented in detail, and an efficient integration of the optimization module with the full-wave solver is demonstrated. In Chapter 4, the design of effective nano-couplers, followed by various examples for nano-optical systems that consist of different types of nano-couplers and nanowires are demonstrated. The thesis ends with concluding remarks given in Chapter 5.

CHAPTER 2

FULL-WAVE ELECTROMAGNETIC SOLVER FOR PLASMONIC APPLICATIONS

2.1 Introduction

This chapter presents the details regarding the simulation tool that is utilized for full-wave solutions of problems involving plasmonic structures. As the numerical methods for solutions of real-life electromagnetic problems improve and computing technology advances, simulation tools become much more involved in the design processes of complex structures, such as nanoparticle couplers and nanowires. In the study of this thesis, obtaining an ultimate design for the desired nano-plasmonic applications may require 6000–8000 full-wave solutions. Hence, in order to achieve reliable designs in reasonable processing times, the simulation environment should be well-organized. In the following sections, the major parts of the constructed simulation environment are presented.

2.2 General View of the Simulation Environment

Full-wave solutions of the plasmonic problems included in the thesis are carried out via an in-house solver based on surface integral equations and MLFMA, while simulations are performed in the MATLAB environment. In Figure 2.1, a diagram that describes the main stages of the simulation environment is presented. Given that a three-dimensional model for the homogeneous plasmonic structure, such as a system of nano-couplers and nanowire transmission lines, is placed in a host medium together with time-harmonic sources involving incident electric and magnetic fields (\mathbf{E}^{inc} and

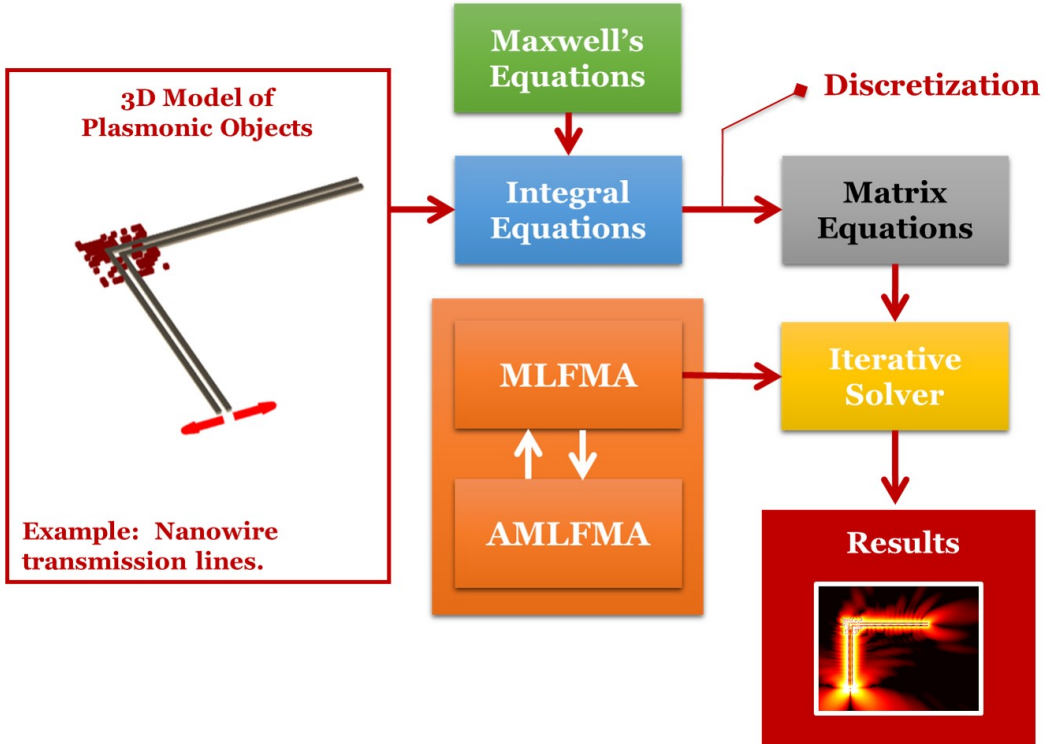


Figure 2.1: Diagram of the constructed simulation environment.

H^{inc}), the electromagnetic problem can be defined as finding its electromagnetic responses. The investigated responses, such as far-zone or near-zone electric and magnetic field intensities, may depend on the application, while their computations require the equivalent currents on the structures. Using the equivalence principle, an equivalent problem representing the problem specified above can be constructed by using equivalent magnetic (M) and electric (J) current densities defined on the surfaces. Then, the solution of the electromagnetic problem corresponds to the computation of these equivalent currents. For this purpose, the mathematical problem is constructed based on surface integral equations, such as the electric-field integral equation (EFIE), the magnetic-field integral equation (MFIE), and their mixed forms, whose derivations are well-known in the literature from the Maxwell's equations and necessary boundary conditions, e.g., the continuity of tangential fields at dielectric interfaces.

For numerical solutions, three-dimensional surface models of the given structures are discretized by using triangular meshes, while surface integral equations are discretized by employing basis and testing functions on these triangular domains. Dis-

cretized integral equations result in dense matrix equations that are solved iteratively by employing an efficient version of MLFMA for accelerating the required matrix-vector multiplications. Moreover, approximate forms of MLFMA (AMLFMA) are also utilized in a multi-layer scheme for effective preconditioning and accelerated solutions. Once a matrix equation is solved, the unknown electric and magnetic current densities corresponding to the solution of the electromagnetic problem can be obtained. At the final step, electromagnetic responses, such as electric and magnetic field intensities and power density distributions can be computed at any desired region via radiation integrals using the corresponding electric and magnetic current densities. In the following sections, the major components of the simulation environment are presented in detail.

2.3 Method of Moments and Discretization

The electromagnetic problems defined in Section 2.2 can be solved with numerical methods based on surface formulations involving EFIE and MFIE [21]. For this purpose, both 3D surface models of metallic nanostructures and surface integral equations are discretized on triangular domains simultaneously and the unknown equivalent surface currents are defined as weighted sums of basis functions, where the weights correspond to the coefficients of the basis functions that need to be solved. Following this idea, dense matrix equations are constructed by using the well-known method of moments (MoM) [22, 23]. To briefly demonstrate MoM, we may consider a general linear equation as

$$\mathcal{L}\{\mathbf{f}\}(\mathbf{r}) = \mathbf{g}(\mathbf{r}), \quad (2.1)$$

where $\mathbf{g}(\mathbf{r})$ is the known vector function defined by the incident electric (\mathbf{E}^{inc}) and magnetic (\mathbf{H}^{inc}) fields due to the external sources, \mathcal{L} is the linear operator that represents the used surface formulation, and $\mathbf{f}(\mathbf{r})$ is the unknown vector function. For numerical solutions, $\mathbf{f}(\mathbf{r})$ can be expressed in terms of known basis functions $\mathbf{b}_n(\mathbf{r})$ and coefficients $\mathbf{a}[n]$ as

$$\mathbf{f}(\mathbf{r}) \approx \sum_{n=1}^N \mathbf{a}[n] \mathbf{b}_n(\mathbf{r}), \quad (2.2)$$

where N is the number of unknowns and $\mathbf{a}[n]$ represents the n th unknown coefficient. Since the number of unknowns is equal to N , the solution of Equation 2.1 requires N linearly independent equations that can be obtained as

$$\int d\mathbf{r} \mathbf{t}_m(\mathbf{r}) \cdot \sum_{n=1}^N \mathbf{a}[n] \mathcal{L}\{\mathbf{b}_n\}(\mathbf{r}) = \int d\mathbf{r} \mathbf{t}_m(\mathbf{r}) \cdot \mathbf{g}(\mathbf{r}), \quad (2.3)$$

by testing Equation 2.1 with test functions $\mathbf{t}_m(\mathbf{r})$ for $m = 1, 2, \dots, N$. The order of the integration and summation can be changed as

$$\sum_{n=1}^N \mathbf{a}[n] \int d\mathbf{r} \mathbf{t}_m(\mathbf{r}) \cdot \mathcal{L}\{\mathbf{b}_n\}(\mathbf{r}) = \int d\mathbf{r} \mathbf{t}_m(\mathbf{r}) \cdot \mathbf{g}(\mathbf{r}) \quad (2.4)$$

so that the matrix equation is obtained as

$$\sum_{n=1}^N \mathbf{a}[n] \bar{\mathbf{Z}}[m, n] = \mathbf{w}[m], \quad m = 1, 2, \dots, N, \quad (2.5)$$

where $\bar{\mathbf{Z}}[m, n]$ (namely the elements of the impedance matrix) and $\mathbf{w}[m]$ (namely the elements of the excitation vector) can be written as

$$\bar{\mathbf{Z}}[m, n] = \int d\mathbf{r} \mathbf{t}_m(\mathbf{r}) \cdot \mathcal{L}\{\mathbf{b}_n\}(\mathbf{r}), \quad (2.6)$$

and

$$\mathbf{w}[m] = \int d\mathbf{r} \mathbf{t}_m(\mathbf{r}) \cdot \mathbf{g}(\mathbf{r}). \quad (2.7)$$

Numerical analysis of an electromagnetic problem requires the solution of Equation 2.5, where the impedance matrix is multiplied with the surface current coefficients (that need to be solved) and the right-hand-side vector represents the excitation. In this study, three-dimensional objects are discretized by using small planar triangles, while first-order functions called the Rao-Wilton-Glisson (RWG) functions, whose efficiency was demonstrated for a plenty of numerical problems involving three-dimensional objects [24], are used for the discretization of surface integral equations. Applying a Galerkin scheme, the RWG functions are used for both basis and testing functions. An RWG function defined on an adjacent triangle pair can be written as

$$\mathbf{b}_n^{\text{RWG}}(\mathbf{r}) = \begin{cases} \frac{l_n}{2A_{n1}}(\mathbf{r} - \mathbf{r}_{n1}), & \mathbf{r} \in S_{n1} \\ \frac{l_n}{2A_{n2}}(\mathbf{r}_{n2} - \mathbf{r}), & \mathbf{r} \in S_{n2} \\ 0, & \mathbf{r} \notin S_n, \end{cases} \quad (2.8)$$

where l_n is the length of the main edge, and A_{n1} and A_{n2} are areas of triangles S_{n1} and S_{n2} , respectively ($S_{n1} \cup S_{n2} = S_n$). In computational electromagnetics point of view, entry $\bar{\mathbf{Z}}[m, n]$ represents the electromagnetic interaction between the m th testing function (\mathbf{t}_m) and the n th basis function (\mathbf{b}_n). Depending on the distance between \mathbf{t}_m and \mathbf{b}_n , some of the interactions correspond to near-field interactions, while some of them are far-field interactions.

2.4 MLFMA

When MoM matrices involving $\mathcal{O}(N)$ unknowns are constructed as in Equation 2.5, they can be solved iteratively rather than using direct methods in order to decrease the required computational sources. However, only using iterative methods is usually not enough to efficiently solve electromagnetic problems, since iterative solutions require large numbers of matrix-vector multiplications (MVMs), each of which corresponds to the computations of interactions between all basis and testing functions. Such direct computations of interactions lead to $\mathcal{O}(N^2)$ complexity per MVM in terms of both time and memory. A more efficient method, namely the fast multipole method (FMM) was proposed to reduce the computational complexity from $\mathcal{O}(N^2)$ to $\mathcal{O}(N^{3/2})$ for the solutions of complex radiation and scattering problems [25, 26]. The idea behind FMM was further extended with a recursive clustering scheme, leading to MLFMA that reduces the computational complexity to $\mathcal{O}(N \log N)$ [27].

The matrix equation in Equation 2.5 can be written shortly as

$$\mathbf{w} = \bar{\mathbf{Z}} \cdot \mathbf{x}. \quad (2.9)$$

In MLFMA, $\bar{\mathbf{Z}}$ can be separated into two parts as

$$\bar{\mathbf{Z}} = \bar{\mathbf{Z}}^{NF} + \bar{\mathbf{Z}}^{FF}, \quad (2.10)$$

where $\bar{\mathbf{Z}}^{NF}$ and $\bar{\mathbf{Z}}^{FF}$ correspond to the near-field and far-field interactions. Elements of $\bar{\mathbf{Z}}^{NF}$ are calculated directly and stored in memory, while the far-field interactions ($\bar{\mathbf{Z}}^{FF}$) are calculated on the fly without being stored in memory. In MLFMA, computational clusters are obtained in a multilevel scheme by dividing a cubic box including the object into eight boxes and recursively dividing all constructed boxes into smaller

boxes until the desired level of clustering is achieved. In this clustering method, the boxes containing none of the discretization elements are eliminated, while the boxes containing the discretization elements remain. Then, far-field interactions in $\bar{\mathbf{Z}}^{FF}$ are calculated in a group-by-group manner using the factorization and diagonalization of the homogeneous-space Green's function in three major stages, namely, aggregation, translation, and disaggregation [21]. In the aggregation stage, radiated fields of boxes are computed from bottom to top. At the lowest level, radiation patterns of basis functions are used to compute radiated fields of the lowest level boxes. Computation for higher-level boxes are performed by shifting and combining radiation patterns of lower-level boxes between corresponding box centers. In the translation stage, radiated fields of boxes are converted into incoming fields for other boxes in the far-zone at the same level. Finally, in the disaggregation stage, total incoming fields for boxes are calculated from top to bottom. Consequently, a part of the MVM corresponding to $\bar{\mathbf{Z}}^{FF} \cdot \mathbf{x}_i$, where \mathbf{x}_i is the proposed solution vector at the i th iteration, is computed without generating or storing $\bar{\mathbf{Z}}^{FF}$. Using the described multilevel structure, the computation complexity is reduced from $\mathcal{O}(N^2)$ to $\mathcal{O}(N \log N)$ since far-zone interactions are not performed for each basis and testing functions one by one, but instead they are performed in group-by-group manner.

MLFMA program used in this study can be divided into two main parts, i.e., the setup and solution parts, as depicted in Figure 2.2. In the setup part, the required matrices and information for the solution part are computed. In the simulation part, MVMs for both far-zone and near-zone interactions are performed as explained above. It should be noted that the MVM cycle is repeated for each candidate solution vector (\mathbf{x}_i) at each iteration (i) until the normalized residual error between the calculated MVM ($\bar{\mathbf{Z}} \cdot \mathbf{x}_i$) and the right-hand-side vector (\mathbf{w}) is smaller than a previously defined threshold value.

2.5 Surface Formulations

Surface integral equations are among popular methods for the solutions of problems involving dielectric objects. Depending on the method to apply boundary conditions, surface integral equations can be formulated in different ways to define the prob-

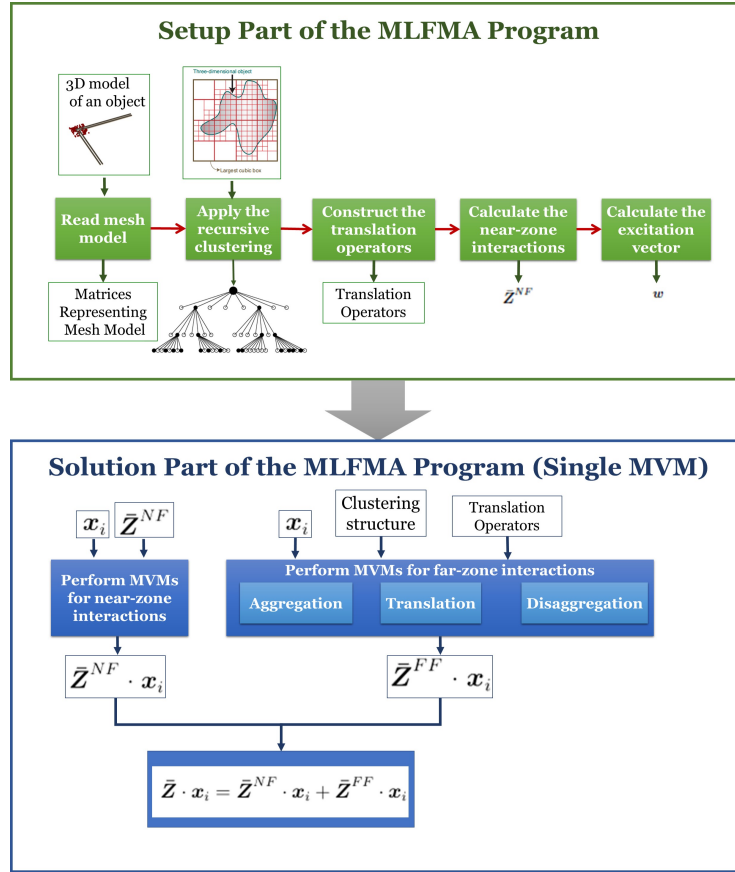


Figure 2.2: Diagrams for the main stages of the MLFMA program.

lems numerically. There is not a unique formulation to solve all kinds of dielectric problems, since the selection of a suitable formulation strongly depends on the problem parameters, such as the excitation frequency and the material of the object to be solved. Some of the conventional formulations for simulations of penetrable bodies are the Poggio-Miller-Chang-Harrington-Wu-Tsai (PMCHWT) formulation, the electric and magnetic current combined-field integral equation (JMCIE), and the combined tangential formulation (CTF). Considering that plasmonic structures, such as metals at optical frequencies, have effective permittivity values with large negative real parts, the conventional formulations listed above are not suitable to simulate such structures with satisfactory efficiency and/or reliable accuracy [28]. Among these, PMCHWT is the one that provides the slowest convergence, but the best accuracy (if converges) for the solution of plasmonic structures. As an alternative, CTF provides solutions with iteratively better convergence in comparison to PMCHWT, while the accuracy of solutions is not as good as that obtained with PMCHWT. Among

these three formulations, JMCFIE is the one that provides solutions with the fastest iterative convergence, but with the poorest accuracy. As an alternative to these conventional formulations, the modified combined tangential formulation (MCTF) was proposed in [28]. This formulation provides solutions for plasmonic problems with much better accuracy in comparison to CTF and JMCFIE, and with much faster iterative convergence rates in comparison to PMCHWT. Moreover, it was shown that MCTF provides reliable solutions in wide ranges of optical frequencies. Considering these earlier findings and after performing numerical tests to measure the accuracy and efficiency of different formulations in the scope of this thesis, MCTF is selected as the main formulation for the analysis of nano-optical structures.

For the solution of electromagnetic problems in this thesis, the required surface formulations can be derived in several steps based on the well-known Maxwell's equations and Helmholtz equations for potentials [21]. Helmholtz equations can be solved for point sources, leading to the homogeneous-space Green's function, i.e.,

$$g(\mathbf{r}, \mathbf{r}') = \frac{\exp(ik|\mathbf{r} - \mathbf{r}'|)}{4\pi|\mathbf{r} - \mathbf{r}'|}, \quad (2.11)$$

where $k = \omega\sqrt{\epsilon\mu}$ represents the wavenumber, \mathbf{r} is the observation point, and \mathbf{r}' is the source point. Equation 2.11 can be utilized as a kernel for the solution of potentials. Then, the electric and magnetic fields (\mathbf{E} and \mathbf{H}) can be written in terms of the electric and magnetic current densities (\mathbf{J} and \mathbf{M}) as

$$\begin{aligned} \mathbf{E}(\mathbf{r}) &= ik\eta \int d\mathbf{r}' \left[\mathbf{J}(\mathbf{r}') + \frac{1}{k^2} \nabla' \cdot \mathbf{J}(\mathbf{r}') \nabla \right] g(\mathbf{r}, \mathbf{r}') \\ &\quad - \int d\mathbf{r}' \nabla g(\mathbf{r}, \mathbf{r}') \times \mathbf{M}(\mathbf{r}') \end{aligned} \quad (2.12)$$

$$\begin{aligned} \mathbf{H}(\mathbf{r}) &= ik\eta^{-1} \int d\mathbf{r}' \left[\mathbf{M}(\mathbf{r}') + \frac{1}{k^2} \nabla' \cdot \mathbf{M}(\mathbf{r}') \nabla \right] g(\mathbf{r}, \mathbf{r}') \\ &\quad + \int d\mathbf{r}' \nabla g(\mathbf{r}, \mathbf{r}') \times \mathbf{J}(\mathbf{r}'), \end{aligned} \quad (2.13)$$

where $\eta = \sqrt{\mu/\epsilon}$ is the intrinsic impedance [21]. Equations 2.12 and 2.13 can be simplified by defining integro-differential operators \mathcal{T} and \mathcal{K} as

$$\mathcal{T}\{\mathbf{X}\}(\mathbf{r}) = ik \int d\mathbf{r}' \left[\mathbf{X}(\mathbf{r}') + \frac{1}{k^2} \nabla' \cdot \mathbf{X}(\mathbf{r}') \nabla \right] g(\mathbf{r}, \mathbf{r}') \quad (2.14)$$

$$\mathcal{K}\{\mathbf{X}\}(\mathbf{r}) = \int d\mathbf{r}' \mathbf{X}(\mathbf{r}') \times \nabla' g(\mathbf{r}, \mathbf{r}'), \quad (2.15)$$

and employing them to obtain

$$\mathbf{E}(\mathbf{r}) = \eta \mathcal{T}\{\mathbf{J}\}(\mathbf{r}) - \mathcal{K}\{\mathbf{M}\}(\mathbf{r}) \quad (2.16)$$

$$\mathbf{H}(\mathbf{r}) = \eta^{-1} \mathcal{T}\{\mathbf{M}\}(\mathbf{r}) + \mathcal{K}\{\mathbf{J}\}(\mathbf{r}). \quad (2.17)$$

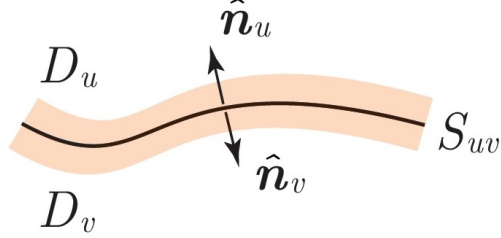


Figure 2.3: Boundaries between two dielectric regions.

Equations 2.16 and 2.17 can be used to derive surface integral equations by applying the operators on currents and enforcing boundary conditions for the tangential components of electromagnetic fields. For this purpose, the problem under focus can be divided into equivalent problems using the equivalence principle. In the electromagnetic simulations of this thesis, we consider problems involving two dielectric regions, e.g., D_u enclosed by a surface S_u and D_v enclosed by a surface S_v as depicted in Figure 2.3. Then, the boundary conditions using equivalent electric and magnetic currents on surfaces due to the continuity of tangential electric and magnetic field intensities can be written as

$$\mathbf{J}_u(\mathbf{r}) = -\mathbf{J}_v(\mathbf{r}) = \mathbf{J}(\mathbf{r}) = \hat{\mathbf{n}} \times \mathbf{H}(\mathbf{r}) \quad (2.18)$$

$$\mathbf{M}_u(\mathbf{r}) = -\mathbf{M}_v(\mathbf{r}) = \mathbf{M}(\mathbf{r}) = -\hat{\mathbf{n}} \times \mathbf{E}(\mathbf{r}), \quad (2.19)$$

where $\hat{\mathbf{n}} = \hat{\mathbf{n}}_u$, and $\mathbf{J}_p(\mathbf{r})$ and $\mathbf{M}_p(\mathbf{r})$ represent equivalent electric and magnetic currents induced on surface S_p for $\{p\}=\{u,v\}$. Considering that $\mathbf{E}(\mathbf{r})$ and $\mathbf{H}(\mathbf{r})$ are total electric and magnetic fields, i.e.,

$$\mathbf{E}(\mathbf{r}) = \mathbf{E}^{inc}(\mathbf{r}) + \mathbf{E}^{sec}(\mathbf{r}) \quad (2.20)$$

$$\mathbf{H}(\mathbf{r}) = \mathbf{H}^{inc}(\mathbf{r}) + \mathbf{H}^{sec}(\mathbf{r}), \quad (2.21)$$

where $\mathbf{E}^{inc}(\mathbf{r})$ and $\mathbf{H}^{inc}(\mathbf{r})$ are incident electric and magnetic fields created by external sources, and $\mathbf{E}^{sec}(\mathbf{r})$ and $\mathbf{H}^{sec}(\mathbf{r})$ are secondary electric and magnetic fields

due to the equivalence currents, basic integral equations can be derived for S_u (i.e., $\mathbf{r} \in S_u$) as

$$\mathbf{J}_u(\mathbf{r}) = \hat{\mathbf{n}}_u \times \mathbf{H}(\mathbf{r}) = \hat{\mathbf{n}}_u \times \mathbf{H}_u^{inc}(\mathbf{r}) + \hat{\mathbf{n}}_u \times \mathbf{H}_u^{sec}(\mathbf{r}) \quad (2.22)$$

$$= \hat{\mathbf{n}}_u \times \mathbf{H}_u^{inc}(\mathbf{r}) + \eta_u^{-1} \hat{\mathbf{n}}_u \times \mathcal{T}_u\{\mathbf{M}_u\}(\mathbf{r}) + \hat{\mathbf{n}}_u \times \mathcal{K}_u\{\mathbf{J}_u\}(\mathbf{r}) \quad (2.23)$$

$$-\mathbf{M}_u(\mathbf{r}) = \hat{\mathbf{n}}_u \times \mathbf{E}(\mathbf{r}) = \hat{\mathbf{n}}_u \times \mathbf{E}_u^{inc}(\mathbf{r}) + \hat{\mathbf{n}}_u \times \mathbf{E}_u^{sec}(\mathbf{r}) \quad (2.24)$$

$$= \hat{\mathbf{n}}_u \times \mathbf{E}_u^{inc}(\mathbf{r}) + \eta_u \hat{\mathbf{n}}_u \times \mathcal{T}_u\{\mathbf{J}_u\}(\mathbf{r}) - \hat{\mathbf{n}}_u \times \mathcal{K}_u\{\mathbf{M}_u\}(\mathbf{r}). \quad (2.25)$$

In Equations 2.23 and 2.25, the limit part of \mathcal{K}_u can be extracted and it can be expressed in terms of its limit part and principal value ($\mathcal{K}_u^{PV}\{\mathbf{X}\}(\mathbf{r})$) as

$$\mathcal{K}_u\{\mathbf{X}\}(\mathbf{r}) = \mathcal{K}_u^{PV}\{\mathbf{X}\}(\mathbf{r}) - \frac{4\pi - \Omega_u}{4\pi} \hat{\mathbf{n}}_u \times \mathbf{X}(\mathbf{r}), \quad (2.26)$$

where $0 \leq \Omega_u \leq 4\pi$ is the internal solid angle. Then, N-EFIE and N-MFIE can be obtained as

$$\begin{aligned} \eta_u \hat{\mathbf{n}}_u \times \mathcal{T}_u\{\mathbf{J}_u\}(\mathbf{r}) - \hat{\mathbf{n}}_u \times \mathcal{K}_u^{PV}\{\mathbf{M}_u\}(\mathbf{r}) \\ + \frac{\Omega_u}{4\pi} \mathbf{M}_u(\mathbf{r}) = -\hat{\mathbf{n}}_u \times \mathbf{E}_u^{inc}(\mathbf{r}) \end{aligned} \quad (2.27)$$

$$\begin{aligned} \eta_u^{-1} \hat{\mathbf{n}}_u \times \mathcal{T}_u\{\mathbf{M}_u\}(\mathbf{r}) + \hat{\mathbf{n}}_u \times \mathcal{K}_u^{PV}\{\mathbf{J}_u\}(\mathbf{r}) \\ - \frac{\Omega_u}{4\pi} \mathbf{J}_u(\mathbf{r}) = -\hat{\mathbf{n}}_u \times \mathbf{H}_u^{inc}(\mathbf{r}). \end{aligned} \quad (2.28)$$

Moreover, multiplying both sides of Equations 2.27 and 2.28 with $-\hat{\mathbf{n}}_u$, T-EFIE and T-MFIE can be obtained as

$$\begin{aligned} -\eta_u \hat{\mathbf{n}}_u \times \hat{\mathbf{n}}_u \times \mathcal{T}_u\{\mathbf{J}_u\}(\mathbf{r}) + \hat{\mathbf{n}}_u \times \hat{\mathbf{n}}_u \times \mathcal{K}_u^{PV}\{\mathbf{M}_u\}(\mathbf{r}) \\ - \frac{\Omega_u}{4\pi} \hat{\mathbf{n}}_u \times \mathbf{M}_u(\mathbf{r}) = \hat{\mathbf{n}}_u \times \hat{\mathbf{n}}_u \times \mathbf{E}_u^{inc}(\mathbf{r}) \end{aligned} \quad (2.29)$$

$$\begin{aligned} -\eta_u^{-1} \hat{\mathbf{n}}_u \times \hat{\mathbf{n}}_u \times \mathcal{T}_u\{\mathbf{M}_u\}(\mathbf{r}) - \hat{\mathbf{n}}_u \times \hat{\mathbf{n}}_u \times \mathcal{K}_u^{PV}\{\mathbf{J}_u\}(\mathbf{r}) \\ + \frac{\Omega_u}{4\pi} \hat{\mathbf{n}}_u \times \mathbf{J}_u(\mathbf{r}) = \hat{\mathbf{n}}_u \times \hat{\mathbf{n}}_u \times \mathbf{H}_u^{inc}(\mathbf{r}). \end{aligned} \quad (2.30)$$

N-EFIE, N-MFIE, T-EFIE, and T-MFIE can be used in different forms and combinations to obtain various surface formulations. In this thesis, dielectric objects with homogeneous material properties are considered in the electromagnetic simulations. Surface formulations for such type of problems can be derived by properly combining

the equations obtained for the inner and outer media of the given problem. Assuming that incident fields exist outside the object, integral equations for inner and outer problems can be written as

$$\begin{aligned} \mathbf{N}\text{-EFIE-I} : \eta_i \hat{\mathbf{n}} \times \mathcal{T}_i\{\mathbf{J}\}(\mathbf{r}) - \hat{\mathbf{n}} \times \mathcal{K}_i^{PV}\{\mathbf{M}\}(\mathbf{r}) \\ - \frac{\Omega_i}{4\pi} \mathbf{M}(\mathbf{r}) = 0 \end{aligned} \quad (2.31)$$

$$\begin{aligned} \mathbf{N}\text{-MFIE-I} : \eta_i^{-1} \hat{\mathbf{n}} \times \mathcal{T}_i\{\mathbf{M}\}(\mathbf{r}) + \hat{\mathbf{n}} \times \mathcal{K}_i^{PV}\{\mathbf{J}\}(\mathbf{r}) \\ + \frac{\Omega_i}{4\pi} \mathbf{J}(\mathbf{r}) = 0 \end{aligned} \quad (2.32)$$

$$\begin{aligned} \mathbf{T}\text{-EFIE-I} : -\eta_i \hat{\mathbf{n}} \times \hat{\mathbf{n}} \times \mathcal{T}_i\{\mathbf{J}\}(\mathbf{r}) + \hat{\mathbf{n}} \times \hat{\mathbf{n}} \times \mathcal{K}_i^{PV}\{\mathbf{M}\}(\mathbf{r}) \\ + \frac{\Omega_i}{4\pi} \hat{\mathbf{n}} \times \mathbf{M}(\mathbf{r}) = 0 \end{aligned} \quad (2.33)$$

$$\begin{aligned} \mathbf{T}\text{-MFIE-I} : -\eta_i^{-1} \hat{\mathbf{n}} \times \hat{\mathbf{n}} \times \mathcal{T}_i\{\mathbf{M}\}(\mathbf{r}) - \hat{\mathbf{n}} \times \hat{\mathbf{n}} \times \mathcal{K}_i^{PV}\{\mathbf{J}\}(\mathbf{r}) \\ - \frac{\Omega_i}{4\pi} \hat{\mathbf{n}} \times \mathbf{J}(\mathbf{r}) = 0 \end{aligned} \quad (2.34)$$

$$\begin{aligned} \mathbf{N}\text{-EFIE-O} : \eta_o \hat{\mathbf{n}} \times \mathcal{T}_o\{\mathbf{J}\}(\mathbf{r}) - \hat{\mathbf{n}} \times \mathcal{K}_o^{PV}\{\mathbf{M}\}(\mathbf{r}) \\ + \frac{\Omega_o}{4\pi} \mathbf{M}(\mathbf{r}) = -\hat{\mathbf{n}} \times \mathbf{E}^{inc}(\mathbf{r}) \end{aligned} \quad (2.35)$$

$$\begin{aligned} \mathbf{N}\text{-MFIE-O} : \eta_o^{-1} \hat{\mathbf{n}} \times \mathcal{T}_o\{\mathbf{M}\}(\mathbf{r}) + \hat{\mathbf{n}} \times \mathcal{K}_o^{PV}\{\mathbf{J}\}(\mathbf{r}) \\ - \frac{\Omega_o}{4\pi} \mathbf{J}(\mathbf{r}) = -\hat{\mathbf{n}} \times \mathbf{H}^{inc}(\mathbf{r}) \end{aligned} \quad (2.36)$$

$$\begin{aligned} \mathbf{T}\text{-EFIE-O} : -\eta_o \hat{\mathbf{n}} \times \hat{\mathbf{n}} \times \mathcal{T}_o\{\mathbf{J}\}(\mathbf{r}) + \hat{\mathbf{n}} \times \hat{\mathbf{n}} \times \mathcal{K}_o^{PV}\{\mathbf{M}\}(\mathbf{r}) \\ - \frac{\Omega_o}{4\pi} \hat{\mathbf{n}} \times \mathbf{M}(\mathbf{r}) = \hat{\mathbf{n}} \times \hat{\mathbf{n}} \times \mathbf{E}^{inc}(\mathbf{r}) \end{aligned} \quad (2.37)$$

$$\begin{aligned} \mathbf{T}\text{-MFIE-O} : -\eta_o^{-1} \hat{\mathbf{n}} \times \hat{\mathbf{n}} \times \mathcal{T}_o\{\mathbf{M}\}(\mathbf{r}) - \hat{\mathbf{n}} \times \hat{\mathbf{n}} \times \mathcal{K}_o^{PV}\{\mathbf{J}\}(\mathbf{r}) \\ + \frac{\Omega_o}{4\pi} \hat{\mathbf{n}} \times \mathbf{J}(\mathbf{r}) = \hat{\mathbf{n}} \times \hat{\mathbf{n}} \times \mathbf{H}^{inc}(\mathbf{r}), \end{aligned} \quad (2.38)$$

where $\hat{\mathbf{n}}$ is the outward normal unit vector of the inner medium, while $\Omega_i = 4\pi - \Omega_o$ and Ω_o are internal and external solid angles. By using Equations 2.31–2.38, a generalized form of surface-integral-equation formulations can be written as

$$\begin{bmatrix} a\mathbf{T}\text{-EFIE-O} + b\mathbf{T}\text{-EFIE-I} + e\mathbf{N}\text{-MFIE-O} - f\mathbf{N}\text{-MFIE-I} \\ c\mathbf{T}\text{-MFIE-O} + d\mathbf{T}\text{-MFIE-I} - g\mathbf{N}\text{-EFIE-O} + h\mathbf{N}\text{-EFIE-I} \end{bmatrix}. \quad (2.39)$$

Based on Equation 2.39, matrix equations representing an electromagnetic problem

can be written as

$$\begin{bmatrix} \mathcal{Z}_{11} & \mathcal{Z}_{12} \\ \mathcal{Z}_{21} & \mathcal{Z}_{22} \end{bmatrix} \cdot \begin{bmatrix} \mathbf{J} \\ \mathbf{M} \end{bmatrix}(\mathbf{r}) = \begin{bmatrix} \mathbf{w}_1 \\ \mathbf{w}_2 \end{bmatrix}(\mathbf{r}), \quad (2.40)$$

where

$$\begin{aligned} \mathcal{Z}_{11} &= -a\eta_o \hat{\mathbf{n}} \times \hat{\mathbf{n}} \times \mathcal{T}_o - b\eta_i \hat{\mathbf{n}} \times \hat{\mathbf{n}} \times \mathcal{T}_i \\ &\quad + e\hat{\mathbf{n}} \times \mathcal{K}_o^{PV} - f\hat{\mathbf{n}} \times \mathcal{K}_i^{PV} - (e+f)\mathcal{I}/2 \end{aligned} \quad (2.41)$$

$$\begin{aligned} \mathcal{Z}_{12} &= a\hat{\mathbf{n}} \times \hat{\mathbf{n}} \times \mathcal{K}_o^{PV} + b\hat{\mathbf{n}} \times \hat{\mathbf{n}} \times \mathcal{K}_i^{PV} \\ &\quad - (a-b)\hat{\mathbf{n}} \times \mathcal{I}/2 + e\eta_o^{-1}\hat{\mathbf{n}} \times \mathcal{T}_o - f\eta_i^{-1}\hat{\mathbf{n}} \times \mathcal{T}_i \end{aligned} \quad (2.42)$$

$$\begin{aligned} \mathcal{Z}_{21} &= -c\hat{\mathbf{n}} \times \hat{\mathbf{n}} \times \mathcal{K}_o^{PV} - d\hat{\mathbf{n}} \times \hat{\mathbf{n}} \times \mathcal{K}_i^{PV} \\ &\quad + (c-d)\hat{\mathbf{n}} \times \mathcal{I}/2 - g\eta_o \hat{\mathbf{n}} \times \mathcal{T}_o - h\eta_i \hat{\mathbf{n}} \times \mathcal{T}_i \end{aligned} \quad (2.43)$$

$$\begin{aligned} \mathcal{Z}_{22} &= -c\eta_o^{-1}\hat{\mathbf{n}} \times \hat{\mathbf{n}} \times \mathcal{T}_o + d\eta_i^{-1}\hat{\mathbf{n}} \times \hat{\mathbf{n}} \times \mathcal{T}_i \\ &\quad + g\hat{\mathbf{n}} \times \mathcal{K}_o^{PV} - h\hat{\mathbf{n}} \times \mathcal{K}_i^{PV} - (g+h)\mathcal{I}/2 \end{aligned} \quad (2.44)$$

and

$$\mathbf{w}_1 = a\hat{\mathbf{n}} \times \hat{\mathbf{n}} \times \mathbf{E}^{inc}(\mathbf{r}) - e\hat{\mathbf{n}} \times \mathbf{H}^{inc}(\mathbf{r}) \quad (2.45)$$

$$\mathbf{w}_2 = c\hat{\mathbf{n}} \times \hat{\mathbf{n}} \times \mathbf{H}^{inc}(\mathbf{r}) + g\hat{\mathbf{n}} \times \mathbf{E}^{inc}(\mathbf{r}). \quad (2.46)$$

In the above, \mathcal{I} is the identity operator. Different selections of constants $\{a, b, c, d, e, f, g, h\}$ lead to different surface formulations as shown in the literature [28]. Selecting them as $a = b = 1$, $c = d = \eta_o \eta_i$, and $e = f = g = h = 0$ leads to MCTF, which is the main formulation used in this thesis.

Employing RWG functions defined in Equation 2.8, the discretized operators can be written as

$$-\hat{\mathbf{n}} \times \hat{\mathbf{n}} \times \mathcal{T}_u \rightarrow \bar{\mathbf{T}}_u^T[m, n] \quad (2.47)$$

$$\hat{\mathbf{n}} \times \mathcal{T}_u \rightarrow \bar{\mathbf{T}}_u^N[m, n] \quad (2.48)$$

$$-\hat{\mathbf{n}} \times \hat{\mathbf{n}} \times \mathcal{K}_u^{PV} \rightarrow \bar{\mathbf{K}}_{PV,u}^T[m, n] \quad (2.49)$$

$$\hat{\mathbf{n}} \times \mathcal{K}_u^{PV} \rightarrow \bar{\mathbf{K}}_{PV,u}^N[m, n] \quad (2.50)$$

$$\mathcal{I} \rightarrow \bar{\mathbf{I}}^T[m, n] \quad (2.51)$$

$$\mathcal{I}^{\times n} \rightarrow \bar{\mathbf{I}}^N[m, n], \quad (2.52)$$

where

$$\begin{aligned}\bar{\mathbf{T}}_u^T[m, n] &= ik_u \int_{S_m} d\mathbf{r} \mathbf{t}_m(\mathbf{r}) \cdot \int_{S_n} d\mathbf{r}' g_u(\mathbf{r}, \mathbf{r}') \mathbf{b}_n(\mathbf{r}') \\ &\quad + \frac{i}{k_u} \int_{S_m} d\mathbf{r} \mathbf{t}_m(\mathbf{r}) \cdot \int_{S_n} d\mathbf{r}' \nabla g_u(\mathbf{r}, \mathbf{r}') \nabla' \cdot \mathbf{b}_n(\mathbf{r}')\end{aligned}\quad (2.53)$$

$$\begin{aligned}\bar{\mathbf{T}}_u^N[m, n] &= ik_u \int_{S_m} d\mathbf{r} \mathbf{t}_m(\mathbf{r}) \cdot \hat{\mathbf{n}} \times \int_{S_n} d\mathbf{r}' g_u(\mathbf{r}, \mathbf{r}') \mathbf{b}_n(\mathbf{r}') \\ &\quad + \frac{i}{k_u} \int_{S_m} d\mathbf{r} \mathbf{t}_m(\mathbf{r}) \cdot \hat{\mathbf{n}} \times \int_{S_n} d\mathbf{r}' \nabla g_u(\mathbf{r}, \mathbf{r}') \nabla' \cdot \mathbf{b}_n(\mathbf{r}')\end{aligned}\quad (2.54)$$

$$\bar{\mathbf{K}}_{PV,u}^T[m, n] = \int_{S_m} d\mathbf{r} \mathbf{t}_m(\mathbf{r}) \cdot \int_{PV, S_n} d\mathbf{r}' \mathbf{b}_n(\mathbf{r}') \times \nabla' g_u(\mathbf{r}, \mathbf{r}') \quad (2.55)$$

$$\bar{\mathbf{K}}_{PV,u}^N[m, n] = \int_{S_m} d\mathbf{r} \mathbf{t}_m(\mathbf{r}) \cdot \hat{\mathbf{n}} \times \int_{PV, S_n} d\mathbf{r}' \mathbf{b}_n(\mathbf{r}') \times \nabla' g_u(\mathbf{r}, \mathbf{r}') \quad (2.56)$$

$$\bar{\mathbf{I}}^T[m, n] = \int_{S_m} d\mathbf{r} \mathbf{t}_m(\mathbf{r}) \cdot \mathbf{b}_n(\mathbf{r}) \quad (2.57)$$

$$\bar{\mathbf{I}}^N[m, n] = \int_{S_m} d\mathbf{r} \mathbf{t}_m(\mathbf{r}) \cdot \hat{\mathbf{n}} \times \mathbf{b}_n(\mathbf{r}), \quad (2.58)$$

for $u = o, i$. Moreover, discretized right-hand-side vectors involving directly and rotationally tested incident electric and magnetic fields can be written as

$$\mathbf{w}_1[m] = -a \int_{S_m} d\mathbf{r} \mathbf{t}_m(\mathbf{r}) \cdot \mathbf{E}^{inc}(\mathbf{r}) - e \int_{S_m} d\mathbf{r} \mathbf{t}_m(\mathbf{r}) \cdot \hat{\mathbf{n}} \times \mathbf{H}^{inc}(\mathbf{r}) \quad (2.59)$$

$$\mathbf{w}_2[m] = -c \int_{S_m} d\mathbf{r} \mathbf{t}_m(\mathbf{r}) \cdot \mathbf{H}^{inc}(\mathbf{r}) + g \int_{S_m} d\mathbf{r} \mathbf{t}_m(\mathbf{r}) \cdot \hat{\mathbf{n}} \times \mathbf{E}^{inc}(\mathbf{r}). \quad (2.60)$$

Using Equations 2.53–2.60, and inserting the corresponding weighting coefficients, the discretized form of MCTF can be written as

$$\begin{bmatrix} \eta_o \bar{\mathbf{T}}_o^T + \eta_i \bar{\mathbf{T}}_i^T & -\bar{\mathbf{K}}_{PV,o}^T - \bar{\mathbf{K}}_{PV,i}^T \\ \eta_o \eta_i (\bar{\mathbf{K}}_{PV,o}^T + \bar{\mathbf{K}}_{PV,i}^T) & \eta_i \bar{\mathbf{T}}_o^T + \eta_o \bar{\mathbf{T}}_i^T \end{bmatrix} \cdot \begin{bmatrix} \boldsymbol{\alpha}_J \\ \boldsymbol{\alpha}_M \end{bmatrix} = \begin{bmatrix} \mathbf{w}_1 \\ \mathbf{w}_2 \end{bmatrix}, \quad (2.61)$$

where

$$\mathbf{w}_1[m] = - \int_{S_m} d\mathbf{r} \mathbf{t}_m(\mathbf{r}) \cdot \mathbf{E}^{inc}(\mathbf{r}) \quad (2.62)$$

$$\mathbf{w}_2[m] = -\eta_o \eta_i \int_{S_m} d\mathbf{r} \mathbf{t}_m(\mathbf{r}) \cdot \mathbf{H}^{inc}(\mathbf{r}). \quad (2.63)$$

In the electromagnetic simulations of this thesis, metallic structures, such as nanowires, are modeled as nonmagnetic ($\mu_o = 4\pi \times 10^{-7}$ H/m permeability) penetrable bodies with their permittivity values having large negative real parts, i.e., $\epsilon_i = (-\epsilon_{Re} + i\epsilon_{Im})$

with $\epsilon_{Re} \gg 1$. All structures are placed in a host medium, i.e., vacuum, where $\epsilon_o=1/(c^2\mu_o)$ and $c = 299792458$ m/s. They are excited by external sources, such as dipoles creating incident electric and magnetic fields (\mathbf{E}^{inc} and \mathbf{H}^{inc}). Using the corresponding parameters for the given problem, 2×2 matrix blocks representing the discretized MCTF can be written as

$$\begin{bmatrix} \bar{\mathbf{Z}}_{11} & \bar{\mathbf{Z}}_{12} \\ \bar{\mathbf{Z}}_{21} & \bar{\mathbf{Z}}_{22} \end{bmatrix} \cdot \begin{bmatrix} \boldsymbol{\alpha}_J \\ \boldsymbol{\alpha}_M \end{bmatrix} = \begin{bmatrix} \mathbf{w}_1 \\ \mathbf{w}_2 \end{bmatrix}, \quad (2.64)$$

where

$$\begin{aligned} \bar{\mathbf{Z}}_{11}[m, n] &= i\omega\mu_o \int_{S_m} d\mathbf{r} \mathbf{t}_m(\mathbf{r}) \cdot \int_{S_n} d\mathbf{r}' \mathbf{b}_n(\mathbf{r}') [g_o(\mathbf{r}, \mathbf{r}') + g_i(\mathbf{r}, \mathbf{r}')] \\ &+ \frac{i}{\omega} \int_{S_m} d\mathbf{r} \mathbf{t}_m(\mathbf{r}) \cdot \int_{S_n} d\mathbf{r}' \nabla' \cdot \mathbf{b}_n(\mathbf{r}') \left[\frac{1}{\epsilon_o} \nabla g_o(\mathbf{r}, \mathbf{r}') + \frac{1}{\epsilon_i} \nabla g_i(\mathbf{r}, \mathbf{r}') \right] \end{aligned} \quad (2.65)$$

$$\begin{aligned} \bar{\mathbf{Z}}_{12}[m, n] &= - \int_{S_m} d\mathbf{r} \mathbf{t}_m(\mathbf{r}) \cdot \int_{PV, S_n} d\mathbf{r}' \mathbf{b}_n(\mathbf{r}') \\ &\times [\nabla' g_o(\mathbf{r}, \mathbf{r}') + \nabla' g_i(\mathbf{r}, \mathbf{r}')] \end{aligned} \quad (2.66)$$

$$\bar{\mathbf{Z}}_{21}[m, n] = - \frac{\mu_o}{\sqrt{\epsilon_o} \sqrt{\epsilon_i}} \bar{\mathbf{Z}}_{12}[m, n] \quad (2.67)$$

$$\begin{aligned} \bar{\mathbf{Z}}_{22}[m, n] &= i\omega\mu_o \int_{S_m} d\mathbf{r} \mathbf{t}_m(\mathbf{r}) \cdot \int_{S_n} d\mathbf{r}' \mathbf{b}_n(\mathbf{r}') \left[\frac{\sqrt{\epsilon_o}}{\sqrt{\epsilon_i}} g_o(\mathbf{r}, \mathbf{r}') + \frac{\sqrt{\epsilon_i}}{\sqrt{\epsilon_o}} g_i(\mathbf{r}, \mathbf{r}') \right] \\ &+ \frac{i}{\omega \sqrt{\epsilon_o} \sqrt{\epsilon_i}} \int_{S_m} d\mathbf{r} \mathbf{t}_m(\mathbf{r}) \cdot \int_{S_n} d\mathbf{r}' \nabla' \cdot \mathbf{b}_n(\mathbf{r}') [\nabla g_o(\mathbf{r}, \mathbf{r}') + \nabla g_i(\mathbf{r}, \mathbf{r}')] \end{aligned} \quad (2.68)$$

and

$$\mathbf{w}_1[m] = - \int_{S_m} d\mathbf{r} \mathbf{t}_m(\mathbf{r}) \cdot \mathbf{E}^{inc}(\mathbf{r}) \quad (2.69)$$

$$\mathbf{w}_2[m] = - \frac{\mu_o}{\sqrt{\epsilon_o} \sqrt{\epsilon_i}} \int_{S_m} d\mathbf{r} \mathbf{t}_m(\mathbf{r}) \cdot \mathbf{H}^{inc}(\mathbf{r}). \quad (2.70)$$

In order to solve Equation 2.64 using MLFMA as explained in Section 2.4, MVMs can be split into two parts as

$$\begin{bmatrix} \mathbf{w}_1 \\ \mathbf{w}_2 \end{bmatrix} = \begin{bmatrix} \bar{\mathbf{Z}}_{11}^{NF} & \bar{\mathbf{Z}}_{12}^{NF} \\ \bar{\mathbf{Z}}_{21}^{NF} & \bar{\mathbf{Z}}_{22}^{NF} \end{bmatrix} \cdot \begin{bmatrix} \boldsymbol{\alpha}_J \\ \boldsymbol{\alpha}_M \end{bmatrix} + \begin{bmatrix} \bar{\mathbf{Z}}_{11}^{FF} & \bar{\mathbf{Z}}_{12}^{FF} \\ \bar{\mathbf{Z}}_{21}^{FF} & \bar{\mathbf{Z}}_{22}^{FF} \end{bmatrix} \cdot \begin{bmatrix} \boldsymbol{\alpha}_J \\ \boldsymbol{\alpha}_M \end{bmatrix}, \quad (2.71)$$

where $\bar{\mathbf{Z}}_{ab}^{NF}$ for $\{a,b\}=\{1,2\}$ corresponds to the near-field interactions between the basis and testing functions that stay in the near-zone region of each other. We note that

each $\bar{\mathbf{Z}}_{ab}^{NF}$ contains $\mathcal{O}(N)$ nonzero elements. Hence, most of interactions in MVMs are performed in the context of the far-field matrices using MLFMA, as explained in Section 2.4. In the setup part, the operators required for translation, aggregation, and disaggregation operations are computed separately for the inner and outer media, and MVMs in the solution part are performed for the inner and outer media separately by using the corresponding operators. After then, the results are combined to obtain the overall result ($\bar{\mathbf{Z}}_{ab}^{FF} \cdot \mathbf{x}_i$) corresponding to far-zone interactions.

In the context of plasmonic simulations, MVMs can further be accelerated with a systematical reduction of far-zone interactions without sacrificing the accuracy by considering rapid decays in plasmonic media [29]. The Green's functions in a plasmonic medium decays rapidly with the distance $|\mathbf{r} - \mathbf{r}'|$. Hence, the inner interactions between the basis and testing functions that are far from each other with considerably long distances weakly contribute to the results of MVMs. Then, computations of some interactions can be omitted without decreasing the accuracy if the contributions by the corresponding interactions are not significant in comparison to the error introduced by MLFMA itself. A safe distance, above which interactions can be omitted, can be determined analytically by estimating the value of the Green's function for the inner media before the iterations. By using this strategy, the number of operations can significantly be reduced and the computation of $\bar{\mathbf{Z}}_{ab}^{FF} \cdot \mathbf{x}_i$ can considerably be accelerated without deteriorating the accuracy since the eliminations are carried out for weak interactions whose contributions do not change the results within error thresholds.

2.6 Iterative Solutions and Preconditioning

MCTF presented in Section 2.5 provides accurate solutions of plasmonic problems involving complex nanowire networks in a wide optical regime. However, matrix equations representing the discretized MCTF often have worse conditioning than those obtained by using other formulations, such as JMCIE. Ill-conditioning leads to slower convergences in iterative solutions, which need to be accelerated by preconditioning. For this purpose, a flexible generalized minimal residual (FGMRES) method is used for main solutions and preconditioning is achieved via inner solutions with generalized minimal residual (GMRES) method employing approximate forms

of MLFMA [30].

The efficiency and accuracy of MLFMA are based on two major mechanisms, factorization (i.e., expressing homogeneous-space Green's function in terms of an infinite summation of spherical harmonics) and diagonalization (i.e., expansion of spherical harmonics in terms of plane waves). There exists a tradeoff between the efficiency and accuracy in the computation of interactions employing MLFMA based on the number of harmonics, which can be controlled via the excess bandwidth formula [31]. Using this formula, the number of harmonics required for a given worst-case error can be determined. In this study, the numbers of harmonics for the factorization and diagonalization are determined such that MVMs for the computation of interactions are performed with two digits of accuracy. It is also possible to accelerate iterations by employing approximate forms of MLFMA, which can perform the computation of interactions by using less numbers of harmonics; but, an approximation leads to less accurate results. Therefore, MLFMA and its approximate forms are employed in a multi-layer scheme for effective preconditioning and accelerated solutions, rather than solely using approximate forms of MLFMA for simulations.

Using a full MLFMA, the cost of an $N \times N$ matrix-vector multiplication can be written as

$$C = c_0 N_{\text{near}} + \sum_{l=1}^L c_l N_l (\tau_l + 1)^2, \quad (2.72)$$

where c_0, c_1, \dots, c_L are constants, $L = \mathcal{O}(N \log N)$ is the number of active levels, $N_{\text{near}} = \mathcal{O}(N)$ is the number of near-zone interactions, N_l represents the number of nonempty boxes, and τ_l is the truncation number (number of harmonics) at level l . In general, $N_1 = \mathcal{O}(N)$, $N_l \approx N_{l-1}/4$ for $l > 1$, $\tau_L = \mathcal{O}(\sqrt{N})$, and $\tau_{l-1} \approx \tau_l/2$ for $l < L$. Therefore, $N_l(\tau_l + 1)^2 = \mathcal{O}(N)$ and $C = \mathcal{O}(N \log N)$. For an approximate form, the truncation numbers can be simply written as $\tau_l^\alpha \approx \alpha \tau_l$ for $\alpha \in [0, 1)$ and the cost becomes

$$C \approx c_0 N_{\text{near}} + \alpha^2 \sum_{l=1}^L c_l N_l (\tau_l + 1)^2, \quad (2.73)$$

where the approximation factor α is the parameter that affects the total time required to perform MVMs in the inner solutions. For our study, α is selected in the range of $[0, 0.2]$ since such a selection provides significant acceleration for the solution of the

interested problems. It should be noted that MVMs for the near-zone interactions are not approximated since their cost is not much as the cost of the far-zone interactions due to sparsity of the $\bar{\mathbf{Z}}^{NF}$ and they are more critical in terms of accuracy.

2.7 Excitation

The right-hand-side in Equation 2.64 corresponds to the excitation vector, which can be obtained as given in Equations 2.69 and 2.70 by testing the incident electric and magnetic fields created by electromagnetic sources. In this study, Hertzian dipoles are used as main excitations. For a Hertzian dipole located at \mathbf{r}' , the electric and magnetic field intensities can be written as

$$\begin{aligned} \mathbf{E}^{inc}(\mathbf{r}) = i\omega\mu_o \frac{\exp(ik_oR)}{4\pi R} \left\{ \mathbf{I}_D \left(1 + \frac{i}{k_oR} - \frac{1}{k_o^2R^2} \right) \right. \\ \left. - \mathbf{I}_D \cdot \hat{\mathbf{R}}\hat{\mathbf{R}} \left(1 + \frac{3i}{k_oR} - \frac{3}{k_o^2R^2} \right) \right\}, \end{aligned} \quad (2.74)$$

and

$$\mathbf{H}^{inc}(\mathbf{r}) = \mathbf{I}_D \times \hat{\mathbf{R}} \frac{\exp(ik_oR)}{4\pi R} \left(\frac{1}{R} - ik_o \right), \quad (2.75)$$

respectively, where $\mathbf{R} = \mathbf{r} - \mathbf{r}' = \hat{\mathbf{R}}R$ and \mathbf{I}_D is the dipole moment.

2.8 Field and Power Calculations

Once the matrix equation in Equation 2.64 is solved by employing MLFMA, α_J and α_M that correspond to the coefficients of the surface currents are obtained. Then, the surface current densities \mathbf{J} and \mathbf{M} at any observation point \mathbf{r} on the surface can be written as

$$\mathbf{J}(\mathbf{r}) \approx \sum_{n=1}^N \alpha_J[n] \mathbf{b}_n(\mathbf{r}) \quad (2.76)$$

and

$$\mathbf{M}(\mathbf{r}) \approx \sum_{n=1}^N \alpha_M[n] \mathbf{b}_n(\mathbf{r}), \quad (2.77)$$

respectively, where \mathbf{b}_n represents the n th basis function associated with the n th edge. After then, the desired electromagnetic responses of the investigated structures can be computed by using \mathbf{J} and \mathbf{M} . In this study, near-zone electric and magnetic fields are particularly considered to understand nano-optical systems. Secondary fields \mathbf{E}^{sec} and \mathbf{H}^{sec} , which are created by the equivalent currents \mathbf{J} and \mathbf{M} on the surface of the object, can be calculated in the desired regions as

$$\begin{aligned} \mathbf{E}^{sec}(\mathbf{r}) &= i\omega\mu_o \int d\mathbf{r}' \mathbf{J}(\mathbf{r}') g_u(\mathbf{r}, \mathbf{r}') + \frac{i}{\omega\epsilon_u} \int d\mathbf{r}' \nabla' \cdot \mathbf{J}(\mathbf{r}') \nabla g_u(\mathbf{r}, \mathbf{r}') \\ &\quad - \int d\mathbf{r}' \nabla g_u(\mathbf{r}, \mathbf{r}') \times \mathbf{M}(\mathbf{r}') \end{aligned} \quad (2.78)$$

$$\begin{aligned} \mathbf{H}^{sec}(\mathbf{r}) &= i\omega\epsilon_u \int d\mathbf{r}' \mathbf{M}(\mathbf{r}') g_u(\mathbf{r}, \mathbf{r}') + \frac{i}{\omega\mu_o} \int d\mathbf{r}' \nabla' \cdot \mathbf{M}(\mathbf{r}') \nabla g_u(\mathbf{r}, \mathbf{r}') \\ &\quad + \int d\mathbf{r}' \mathbf{J}(\mathbf{r}') \times \nabla' g_u(\mathbf{r}, \mathbf{r}'), \end{aligned} \quad (2.79)$$

where the integrals can be used for the outer ($u = o$) or inner ($u = i$) media. Based on the equivalence principle, the integration for the inner medium should lead to zero fields for the outer region, while the integration for the outer medium should result in zero fields for the inner region. In fact, by using this, the accuracy of a solution can be tested. Near-zone field distributions over a region involving nanowires, couplers, and the host medium must be calculated for the inner and outer media separately, and the results must be superimposed to obtain the overall distributions in the entire region. Moreover, for the outer-medium calculations, incident fields \mathbf{E}^{inc} and \mathbf{H}^{inc} are added to the secondary fields \mathbf{E}^{sec} and \mathbf{H}^{sec} to obtain total field intensities, while this is not required for inner-medium calculations. Once the field intensities are obtained, the associated power density $\mathbf{S}(\mathbf{r})$ values can be calculated as

$$\mathbf{S}(\mathbf{r}) = \frac{1}{2} \mathbf{E}(\mathbf{r}) \times \mathbf{H}^*(\mathbf{r}), \quad (2.80)$$

where $*$ is the conjugate operation. Equation 2.80 corresponds to the calculation of the Poynting vector, where the real part is the time-averaged power density.

2.9 Remarks

In this chapter, the main components of a full-wave solver proposed for efficient and accurate solutions of complex plasmonic problems involving nanowires and couplers are presented. To sum up, the solver is based on surface integral equations

and MLFMA that has been developed for plasmonic structures. As surface formulations, among different alternatives, MCTF is used to model the problems since it provides relatively accurate and efficient solutions. The standart RWG functions are used for the discretization. Iterative solutions are further accelerated by using FGMRES, where preconditioning is achieved via inner solutions with GMRES employing approximate forms of MLFMA.

In the next chapter, the integration of this full-wave solver with an optimization tool is presented.

CHAPTER 3

OPTIMIZATION MECHANISM FOR THE DESIGN OF NANOPARTICLE ARRAYS

3.1 Introduction

This chapter is devoted to the details of the optimization tool that is used in the design of efficient couplers to improve optical transmission in complex nanowire networks. Designing structures with satisfactory performances is a challenging process that requires the investigation of several parameters related to the electromagnetic problem under investigation. Specifically, there may be a plenty of possible solutions for different parameters. Finding the ultimate design among all possible solutions that satisfies the desired electromagnetic response requires a well-organized optimization tool integrated with a full-wave solver that provides fast and accurate simulations. In the following sections, the main stages of the optimization tool developed for the optimization of nanoparticle arrays, which are used as couplers to improve nano-optical networks, are explained. In addition, efficient integration of the optimization tool with the full-wave solver developed for rigorous solutions of plasmonic problems is presented.

3.2 Overall Structure

In this thesis, couplers are designed by considering array arrangements of plasmonic nanoparticles in order to improve the optical power transmission through different types of nanowires, where the existences of the particles on a predetermined regular grid are the optimization parameters. As it is given in Figure 3.1, the overall opti-

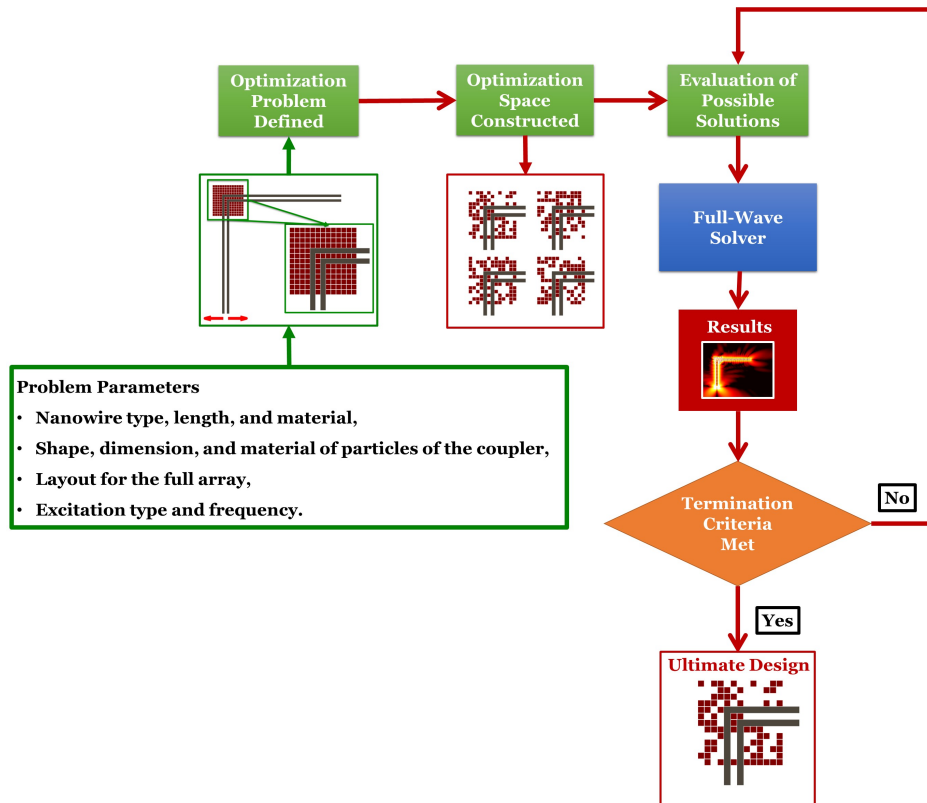


Figure 3.1: Diagram for the stages of the optimization mechanism.

mization process starts by defining the optimization problem with properly selected initial problem parameters. Given a target, which is usually improving/balancing power transmission through corners, junctions, etc., nanowire segments representing the optimization problem are selected. For example, nanowires with 90° sharp bends are chosen to design a coupler for improving power transmission through a sharp corner, while straight nanowires are used to design a coupler to improve coupling between external sources and nanowires. A full array corresponding to the initial coupler (when all nanoparticles exist on a predetermined grid with constant distances between consecutive elements) is placed at the optimization location, where the power transmission typically deteriorates. Starting with the full array, an optimization problem can be defined as finding the elements of the full array that should be extracted such that the rest of the nanoparticles can provide efficient coupling for the power transmission. The optimal set and the configuration for the coupler are searched with an optimization method, where possible designs are selected from an optimization space involving different configurations of particles and evaluated based on their full-

wave solutions provided by the electromagnetic solver introduced in Chapter 2. This cycle of optimization continues until predetermined termination criteria are met.

The optimization problem defined above can be considered as challenging due to several reasons. First, a typical coupler in this study involves an arrangement of 140–200 nanoparticles so that an optimization space can be as large as $2^{200} \approx 10^{60}$ candidate solutions, while it may be even larger when simultaneous optimization of multiple couplers is considered. Second, the cost function, which defines the target parameter desired to be improved by an optimization, may involve single or multiple design parameters that do not have closed-form derivatives. This inhibits the use of well-known optimization methods based on gradients. Third, considering huge optimization spaces, a good starting point becomes crucial to achieve globally optimized solutions, while such initial designs are not available for the considered set of problems. Finally, the design of efficient couplers may involve optimization problems for multi-purpose applications or problems with multiple solutions, leading to challenges for the convergence of optimization trials. Considering all these challenges, evolutionary-type heuristic algorithms, such as genetic algorithms (GAs), can provide optimized solutions with satisfactory performances thanks to their ability to handle huge optimization spaces, multi-purpose cost functions, problems with multiple solutions, and challenges regarding the starting point of optimization problems. The efficiency and flexibility of GAs are well-known in the literature for different types of electromagnetic problems [32–37]. Especially, their flexibility in defining cost functions and ability to show progress regardless of a starting point in huge optimization spaces make GAs favorable against gradient-based local-search optimization methods. In general, gradient-based methods require differentiable and continuous cost functions, as well as good initial values, while having difficulty in handling huge optimization spaces [38–40]. Considering all of these, in this work, optimization problems defined above are solved by an optimization module that employs an efficient in-house implementation of GAs and the full-wave solver developed for plasmonic problems as introduced in Chapter 2. In the next section, details related to the implementation of GAs are given.

3.3 GAs and Related Definitions

GAs are among the heuristic optimization methods based on a natural selection process with bio-inspired operations, such as mutation, crossover, and selection, and they are especially useful for problems in which the objective function is discontinuous, non-differentiable, stochastic, and/or highly nonlinear. Starting with an initial guess for the ultimate solution, GAs are based on the evaluation of trials such that a particular function, namely fitness or cost function, can be maximized or minimized. In general, fitness functions are designed based on the target of the optimization problem. Despite their random nature for the selection of individuals, efficient and systematic usages of operations that imitate the biological processes of reproduction and natural selection, such as mutation, crossover, and selection, make GAs much more useful and powerful than random search algorithms [41–43]. Moreover, in GAs, randomness for the evaluation of individuals is controlled by inherent parameters, such as mutation and crossover rates, which provide controllability and efficiency for an effective optimization.

In Figure 3.2, a block diagram of standard GAs is presented. Since they are inspired by Charles Darwin's theory of evolution, most of the terms in GAs, some of which are given in Figure 3.2, are taken from their biological counterparts. In general, GAs work on chromosomes, where candidate values of design parameters are encoded. In other words, each chromosome refers to a possible solution, while its small segments correspond to different design parameters of the overall solution. Design parameters desired to be included in an optimization can be encoded into chromosomes in different ways, while a common approach is using strings of binary numbers (sequence of 1's and 0's). Depending on the problem, a single parameter can be represented by either a string of several bits or only a single bit. Once the way of parameter encoding is defined, a set of chromosomes can be randomly generated, and an initial population involving a set of possible solutions, namely individuals, can be constructed.

Chromosome representation and initialization of the first population have crucial roles in the success of a GA optimization. Depending on the number of parameters involved in the optimization and the length of chromosomes, the optimum size for the pool may differ. There exists a tradeoff in the selection of the pool size, i.e., increas-

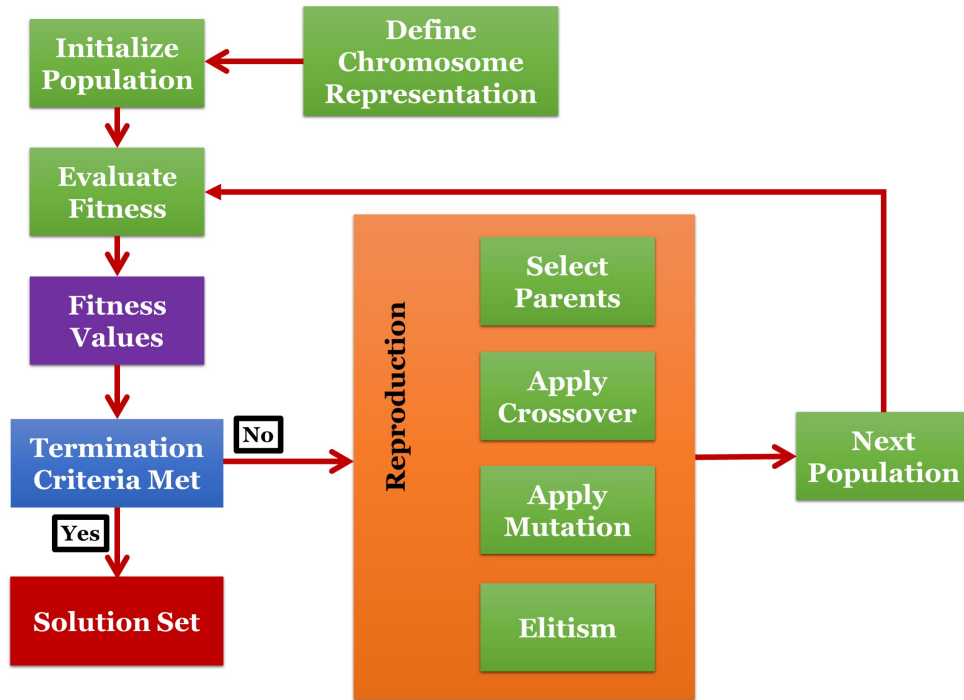


Figure 3.2: Block diagram for standard GAs.

ing the pool size increases the optimization time, but it may also increase the quality of the optimization result thanks to the higher diversity, and vice versa. Starting an optimization with a small population of chromosomes may yield high-quality solutions with a fast convergence history, whereas it may be stuck at a poor solution. On the other hand, optimization trials with relatively small populations may successfully achieve superior individuals in short times, especially for optimization problems involving small numbers of design parameters. Therefore, the size and diversity of a population should be well-chosen to achieve satisfactory results with good stability such that different trials of the optimization can provide similar results with satisfactory performances in terms of the optimization target.

Once the initial population is constructed based on randomly generated chromosomes, the next stage of a standard GA optimization is to evaluate the fitness value of each individual in the population, which represents the quality of the corresponding individual in terms of the target of the optimization problem. Defining a proper fitness (cost) function is a critical issue for a successful optimization trial, since the selection of individuals and the evaluation of solutions mainly depend on fitness values.

Basically, in GAs, fitness values are used for grading the individuals to measure how much they satisfy the target of the optimization problem. After the individuals in the current population are evaluated with their fitness values, their chromosomes are manipulated in different ways to construct the chromosomes for the next generation. For this purpose, pairs of individuals are selected from the population as parents based on their fitness values. There are several selection strategies to determine parents, while a brute-force way is choosing the best pairs of individuals as parents, which may decrease the diversity of the population. In this study, the tournament selection method is used for the selection of parents since its efficiency for complex optimization problems involving large numbers of design parameters is already demonstrated in the literature [41, 42]. Once the parents are selected, the individuals of the next population are created by using major operators of GAs, such as crossover and mutation. The crossover operator generates the child chromosomes by mixing of the parent chromosomes, while mutations are applied to randomly change the bits with a user-defined probability rate, namely the mutation rate. Mutations are essential to increase the diversity in the population, while their randomness may lead to loss of successful solutions with relatively good fitness values. To increase the stability, mutations are applied on the individual chromosomes with different probability rates, which are determined based on their fitness values. Specifically, successful individuals are less likely to mutate, while aggressive mutations are applied on the chromosomes of unsuccessful individuals. In addition to mutation and crossover, another mechanism in GAs is the elitism strategy, which means transferring the best individuals of the current population to the next population such that the best fitness value always increases monotonically as the optimization continues. Elitism guarantees that the overall quality of the pool never deteriorates. By performing all these operations, chromosomes corresponding to the individuals of the next population are generated. The cycle of fitness evaluation, selection, and reproduction in GAs continues until the best individual in a population satisfies the design criteria and the ultimate design for the optimization problem is obtained.

3.4 Efficient and Integrated Combination of the Full-Wave Solver with GAs for the Optimization of Couplers

In this study, coupler designs are obtained by employing an efficient and integrated combination of the implemented GAs and the full-wave solver presented in Chapter 2. As described in Section 3.2, starting with a regular grid, each nanoparticle is extracted or kept independently to reach the optimal set and configuration. Then, the optimization parameter can be stated as the existence of each nanoparticle on the predetermined grid. Hence, binary chromosomes involving 0 (off/extract) and 1 (on/keep) bit values are used so that the chromosome length corresponds to the number of initial particles in the designed coupler. In order to improve the convergence and stability of the optimization trials, powerful GAs operations introduced in Section 3.2, such as success-based mutations and elitism, are applied.

The GA module and the electromagnetic solver developed for the solution of plasmonic problems are integrated into a single mechanism. There are several ways for the combination of optimization and simulation modules. A brute-force way can be assuming the full-wave solver as a black-box, where the solution of each individual is carried out as an independent electromagnetic problem including both setup and solution parts. In this study, a more efficient and integrated combination of optimization and electromagnetic solver modules is implemented, as depicted in Figure 3.3. In this mechanism, setup computations, such as reading mesh model, obtaining tree structure for clustering, calculating translation operators for the MLFMA solver, computing near-zone interactions, and constructing the right-hand-side vector, are performed once before the optimization starts. We note that these calculations are performed for the full problem that involves the integration of the full array (coupler) with the investigated nanowire system. As an example, in Figure 3.3, a full problem for the optimization of corner couplers with 90° -bent nanowires is presented. Once initial computations are carried out, the outputs can be stored in either external storage or primary memory to keep them available during the evaluation of fitness values. For each individual of the optimization, the particles that should be extracted from the full array are determined based on bits of the corresponding chromosomes. Then, necessary row/column deletions on the full matrix equation are performed considering the

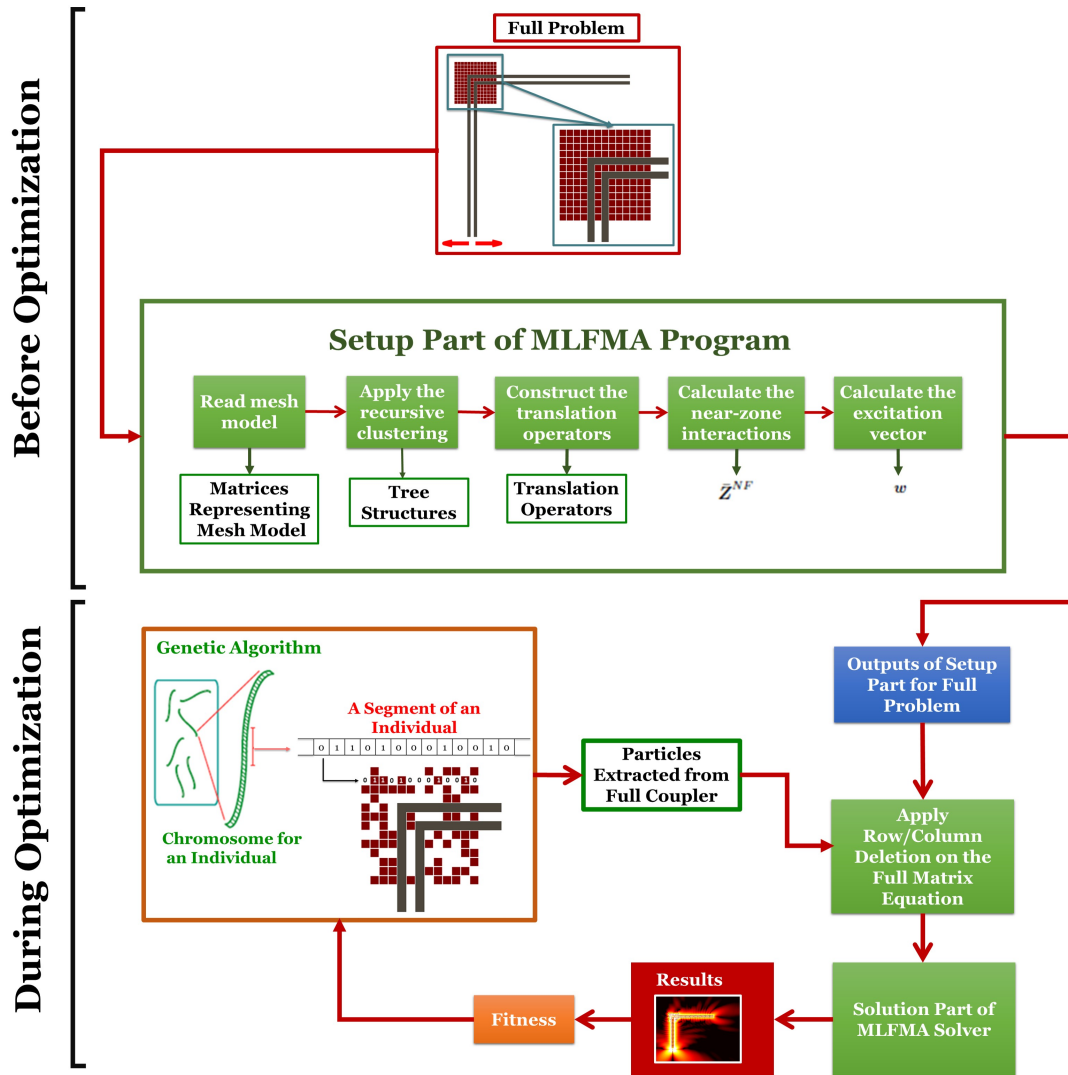


Figure 3.3: Block diagram for the efficient integration of the MLFMA solver with GAs.

equations corresponding to off elements. This efficient integration yields significant reductions in the processing times required to evaluate the fitness of the individuals since the computations in the setup part do not have to be repeated.

3.5 Remarks

In this chapter, the optimization problems involving the design of efficient couplers for different types of nanowire transmission lines are defined, and the optimization tool proposed and used for this purpose is explained in detail. To sum up, a robust mechanism involving an efficient and integrated combination of GAs and the full-wave solver developed for accurate solutions of plasmonic problems is proposed to design effective couplers via on-off optimization. The performance of GAs is further improved by using novel operations, such as success-based mutations.

In the next chapter, the application of the optimization mechanism introduced in this chapter to design various types of couplers for different scenarios is presented. The designed couplers are rigorously investigated to demonstrate the efficiency of the optimization mechanism, as well as the effectiveness of the designs.

CHAPTER 4

OPTIMIZATION OF NANOPARTICLE COUPLERS FOR NANO-OPTICAL NETWORKS

4.1 Introduction

In this chapter, the optimization tool presented in Chapter 3 is utilized for rigorous designs of couplers composed of different arrangements of nanoparticles to control and guide optical waves throughout nanowire networks with complex junctions and bends. Depending on the complexity of nano-optical links, different arrangements of nanoparticle arrays may be necessary to eliminate power losses due to diffractions and multiple reflections at junctions and bending regions, and to provide efficient guidance of plasmonic waves within nanowire-vacuum interfaces. On the other side, such nanowire networks may occupy large areas in terms of wavelength with their diverse nanowire segments, junctions, and bends. Hence, optimization of nano-couplers that work only for a specific nanowire network may not be a feasible approach considering the increase in the computational load. Instead, dividing the given problem into sub-problems and designing couplers for smaller scenarios representing junctions, bends, or input tips of larger nanowire networks can provide the required designs of different types of couplers with less computational sources. An important issue about this approach is the compatibility of couplers with nanowire segments that are different than those used during the optimization of the corresponding couplers. To elaborate on this issue, besides the design of couplers for specific nanowires, their abilities to build more complex nanowire networks involving connections of several nanowire segments with multiple junctions, bends, and outputs are examined in detail. The results are interpreted to reach conclusions and guidelines for the efficient use of couplers, which are designed in different and isolated scenarios, while building larger

nanowire networks.

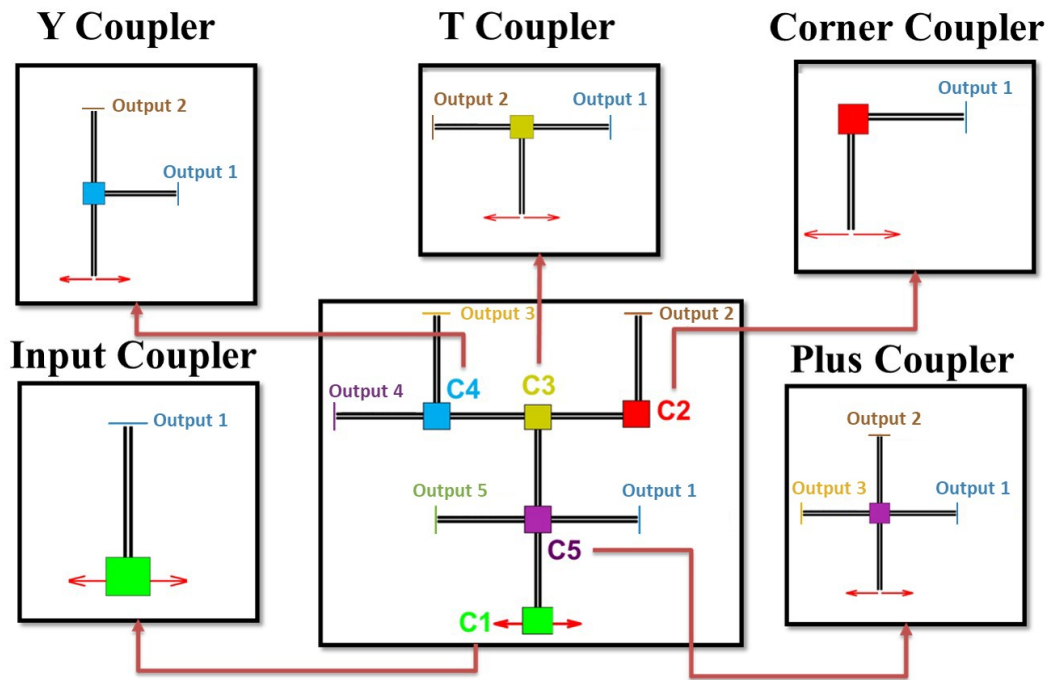


Figure 4.1: Coupler design problems and an illustration of their integration to build a large nanowire network.

Specifically, in this thesis, five different types of couplers, i.e., input, plus, corner, Y, and T types are investigated. Design of each coupler is obtained for a specific nanowire sub-system, as illustrated in Figure 4.1. For example, the input coupler is optimized by using a straight nanowire, while the corner coupler is designed for 90°-bent nanowires. The nanowire sub-systems used for the design of plus, Y, and T couplers are clearly described in Figure 4.1. Extensive details regarding the optimization and analysis of each coupler are presented in different sections of this chapter. Moreover, different scenarios including the optimization of couplers in nanowire systems composed of multiple coupler regions are also discussed. As another section, performance of the designed couplers and their compatibility in complex and large nanowire networks are presented. Finally in the last section, sensitivity of the couplers to possible fabrication errors is presented.

4.2 Parameters Related to Electromagnetic Simulations

This chapter presents design and simulation for various type of couplers that are aimed to improve power transmissions along different nanowire sub-systems, such as straight nanowires, 90°-bent nanowires, nanowires with junctions, etc. While performing optimization trials and post-process simulations, some parameters related to the geometrical shape, number, and material of the nanowires and some other parameters related to the excitation type and the frequency are fixed unless stated otherwise. In this section, these parameters are introduced, some of which are also illustrated in Figure 4.2. Straight nanowires are used for this illustration. Same values of these parameters are also valid for other types of nanowire sub-systems that are investigated throughout this chapter.

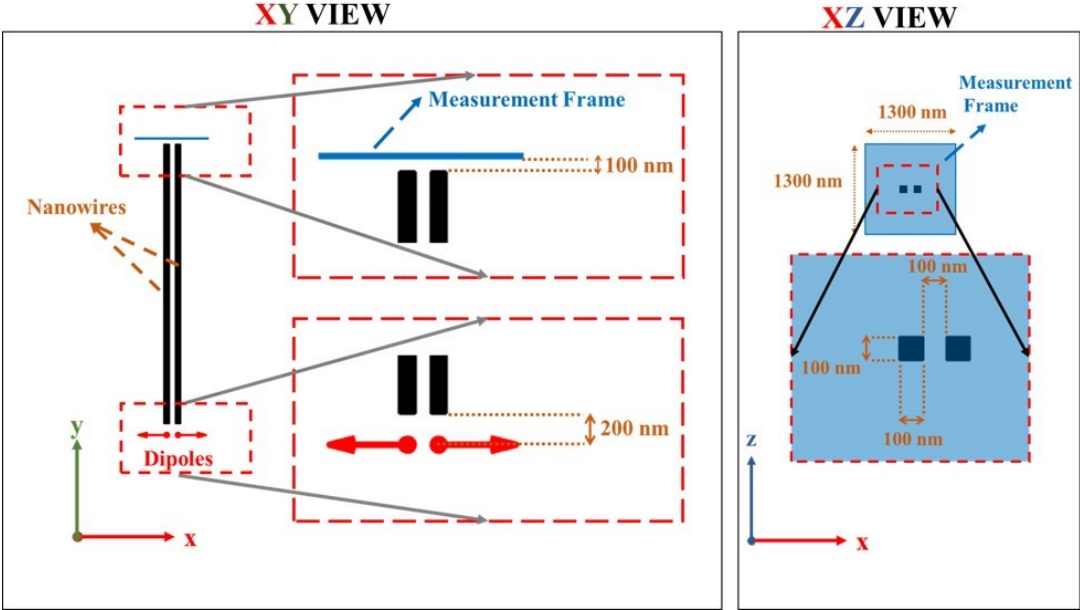


Figure 4.2: Illustration of some parameters related to the electromagnetic simulations and optimization trials.

Several research studies have been performed on the effects of shape and cross sections to the propagation of SPPs along nanowires [1, 2, 5, 8, 10]. More specifically, it was shown that the shape of a nanowire has major effects on the modes of SPPs initiated over the nanowire surface, propagation losses, and confinement radius [5]. The size of a nanowire is shown to be one of the critical parameters, which affect the

coupling efficiency between near-field emitters and propagating SPPs, as well as the out-coupling efficiency of SPPs at nanowires' output tips to the far-zone in the host media [13]. Moreover, it has been also revealed that the use of nanowire arrays with plasmonic materials can provide significant improvements on the power transmission, in comparison to the utilization of a single nanowire [10].

Considering the outcomes of research studies, pairs of nanowires in close proximity can be utilized for the construction of nanowire networks with various arrangements, including different numbers of outputs. The use of double nanowires for the transmission of electromagnetic energy rather than using nanowire arrays expanding in two or three directions provides additional compactness, while the required power levels at outputs can be achieved by the integration of efficient couplers at necessary regions as investigated in this thesis. The cross sections of nanowires are chosen to be square with the edge length of 100 nm so that a nanowire covers an area of $100 \text{ nm} \times 100 \text{ nm}$. Moreover, the face-to-face distance between a nanowire pair is also fixed to 100 nm, as shown in the x - z view of Figure 4.2. In numerical analyses, the nanowires are excited by Hertzian dipole pairs with unit dipole moments, while \mathbf{E}^{inc} and \mathbf{H}^{inc} created by a single dipole are as given in Equations 2.74 and 2.75, respectively. Dipoles are placed 200 nm away from the nanowires and oriented in opposite directions such that surface plasmons propagating along the longitudinal axes of the nanowires can be generated, while symmetrical patterns for both field and power distributions can be achieved at the outputs. As the target frequency of the optimization problems, 250 THz that is in the range of the near-infrared region of the electromagnetic spectrum is selected, while extensive analysis on the performance of couplers and nanowire networks have also been performed in a range of frequencies. Among different alternatives for the material of couplers and nanowires, silver, whose permittivity has a relatively large negative real part and considerably small imaginary part, is chosen. Specifically, the relative complex permittivity of the silver at 250 THz can be chosen approximately as $-60.7546+4.3097i$ based on the Lorentz-Drude model [44]. The permeability of the silver is assumed to be equal to the permeability of vacuum due to its non-magnetic behavior. All analysis and designs involving various arrangements of nanowires and couplers are performed by selecting the host media as vacuum such that high-contrast problems need to be solved. Transmission

Table 4.1: Parameters Related to the Nanowires and Excitation

Parameter	Value/Type
Nanowire Configuration	Double nanowires in close proximity
Spacing Between the Adjacent Nanowires	100 nm
Cross Sections of the Nanowires	100 nm \times 100 nm square
Material of the Nanowires	Ag ($\epsilon_r = -60.7546 + 4.3097i$, $\mu_r = 1$)
Excitation	Dipole pairs that are placed 100 nm away from the nanowires
Frequency	250 THz
Host Media	Vacuum
Measurement Frames	1300 nm \times 1300 nm square frames placed symmetrically at 100 nm distances from the output tips of the nanowires

abilities of nanowire systems for different scenarios are examined and compared with each other by using the corresponding near-zone power density values, which are calculated as explained in Section 2.8. For this purpose, the power density for each case is calculated in a 1300 nm \times 1300 nm square frame (called measurement frame in Figure 4.2), which is placed symmetrically at 100 nm distance from the output tips of the nanowire pairs. Each output of nanowire networks involves the tips of double nanowires, as illustrated in Figure 4.2. The fixed parameters related to nanowires and their excitations are summarized in Table 4.1.

The solver introduced in Chapter 2 is utilized with the parameters given in Table 4.2 for efficient and accurate full-wave solutions of the nano-optical links and networks involving different arrangements of nanowire segments and couplers. Designs of the couplers for different problems are obtained with the optimization tool introduced in Chapter 3 by using the parameters in Table 4.3. The parameters listed in Tables 4.1, 4.2, 4.3 are fixed unless stated otherwise. Couplers considered in this study are mostly designed by using cubic particles that have edges of 90 nm. Depending on the

performance of the coupler, configurations using particles with various shapes, such as spheres and cylinders, are also investigated in the scope of the study. Moreover, the sensitivity of the couplers' performances to the sizes of the individual particles is under interest.

Table 4.2: Parameters Related to the Full-wave Solver

Name	Value/Type
Solver	MLFMA
Formulation	MCTF
Residual Error	0.0001
Preconditioner	AMLFMA with $\alpha \in [0, 0.2]$
Discretization Size	$\lambda/15 - \lambda/20$

Table 4.3: Parameters Related to GAs

Name	Value
Mutation Rate for Successful Individuals	5%
Mutation Rate for Unsuccessful Individuals	70%
Crossover Rate	85%
Individuals Per Generation (Pool Size)	40

4.3 Design of Efficient Input Couplers

One of the crucial parameters for a satisfactory electromagnetic energy flow through a complex nanowire network is the efficiency of the generation of SPPs along nanowires with the excitation by an external source. Among different excitation types, it was shown in [6] that high-quality coupling to plasmonic nanowires can be achieved via near-field emitters, such as a dipole emitter. However, the excitation of propagating SPPs by such types of emitters is still a challenging design problem to achieve an adequate level of power transmission for the target applications. Fields radiated by an emitter tend to attenuate in free space rather than being coupled to guided modes of SPPs along nanowires, unless the design parameters of the nanowires, such as the

shape and size of the cross section, are properly selected.

Several research studies regarding geometry-related parameters have been conducted to achieve improvement in the coupling between propagating plasmons confined to outer surfaces of nanowires and external sources [1, 2, 13, 14]. For example, in [13], it was shown that the width of the nanowires has a major effect for the generation of SPPs over metallic surfaces. Typically, as nanowires become narrower, the coupling from an emitter to SPPs significantly deteriorates and the power transmitted by them decreases. However, selection of nanowires with larger widths has been naturally limited by the radiation ability of SPPs from the end tips into host media. Specifically, as the width becomes larger, despite the increase in the coupling between the emitter and SPPs, the radiation ability of SPPs from the abrupt end of the nanowire into the host media can be considerably deteriorated. Hence, the tradeoff in the selection of an optimum value of the width of nanowires can result in a challenging problem to achieve reasonable coupling levels on both input and output sides.

Designing compact structures that increase interactions of emitters and nanowire systems by means of efficient coupling can be stated as a favorable alternative when the tradeoff regarding the proper selection of nanowire parameters is considered. In this section, we present the design of arrays of nanoparticles to effectively couple power radiated by sources to nanowire systems. In this strategy, multiple reflections of optical waves trapped in a cavity composed of suitable arrangements of nanoparticles around the input tips of nanowires and emitters can be utilized to boost SPPs generated along nanowires. From one perspective, the favorable features and properties of optical microcavities, such as presented in [45], are combined with the extraordinary interactions of nanoparticles to achieve satisfactory coupling and transmission levels. Optimal arrangements of arrays, namely input couplers (ICs), are designed with the optimization tool described in Chapter 3.

In the following, optimization of ICs for various cases is considered to increase the power transmitted via a pair of straight nanowires with $5 \mu\text{m}$ lengths when they are excited by Hertzian dipoles. Parameters that are fixed during the optimization trials related to the nanowires and the excitation are listed in Table 4.1. Considering that each nanowire occupies $100 \text{ nm} \times 5000 \text{ nm} \times 100 \text{ nm}$ volume and they are placed

with 100 nm surface-to-surface distance, the overall structure (nanowire pairs) occupies $300 \text{ nm} \times 5000 \text{ nm} \times 100 \text{ nm}$ volume. At the frequency of optimization (250 THz), this corresponds to $0.25\lambda \times 4.1667\lambda \times 0.0833\lambda$ in terms of wavelength. The pair of straight nanowires considered in the optimization problems is shown in Figure 4.3. In this figure, the region of IC, in which optimal configurations of nanoparticle arrays are sought, is also illustrated with a representative rectangle. Couplers are designed by considering array arrangements of cubic particles made of Ag. Nanocubes have edges of 90 nm and they are placed with 10 nm surface-to-surface distances. Choosing nanocubes with edge lengths not larger than the height and width of the nanowires is desired to avoid increasing the dimensions of the overall system. Optimization trials are performed to find the nanocubes to be extracted from the starting full-grid array of the optimization layout. Thus, the size the optimized coupler and the location of the individual nanoparticles are restricted by the optimization layout, which is itself an optimization parameter to be examined.

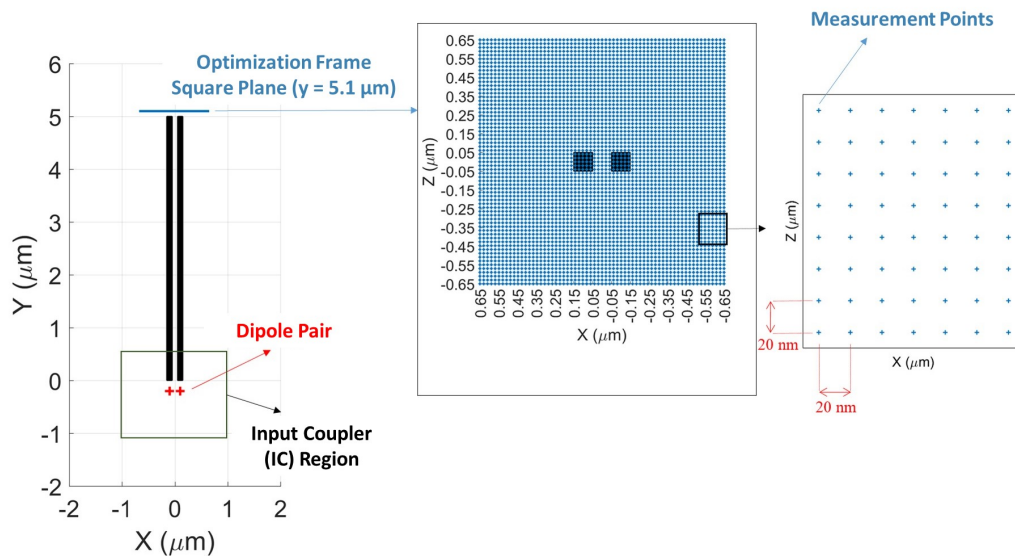


Figure 4.3: A pair of nanowires considered in IC optimization trials and the corresponding measurement (optimization) frame, in which power density values are computed.

While designing an IC, it is aimed to improve the coupling between the emitter and SPPs on the nanowires. Considering this aim, the cost function of the optimization is selected as the mean of the power density values calculated at the grid points of the optimization frame ($1.3 \mu\text{m} \times 1.3 \mu\text{m}$). The optimization (measurement) frame is

selected as lying in the x - z plane at $y = 5.1 \mu\text{m}$ such that measurements of the power density values are performed at a plane parallel to the end surfaces of the nanowires. Given that the Poynting vector (W/m^2) (whose calculation is explained in Section 2.8) is defined as

$$\mathbf{S}(x_i, y_i, z_i) = [S_x(x_i, y_i, z_i), S_y(x_i, y_i, z_i), S_z(x_i, y_i, z_i)] \quad (4.1)$$

in terms of its components along x axis (S_x), y axis (S_y), and z axis (S_z), the cost function of the problem can be defined as

$$CF = \frac{\sum_{i=1}^N \sqrt{|S_x(x_i, y_i, z_i)|^2 + |S_y(x_i, y_i, z_i)|^2 + |S_z(x_i, y_i, z_i)|^2}}{N}, \quad (4.2)$$

where x_i , y_i , and z_i are the coordinates of the sampling points for the measurements as illustrated in Figure 4.3. The distance between the consecutive sampling points is chosen as 20 nm (0.0167λ) for both x and z directions, which is determined to be enough for the consistency and convergence of the mean power density in the frame. Optimization trials presented in this section are carried out using the optimization tool proposed in Chapter 3 with the optimization parameters given in Table 4.3, while the full-wave solutions of the individuals are performed by using the MLFMA solver introduced in Chapter 2 with the solver parameters in Table 4.2.

4.3.1 Power Transmission through Straight Nanowires

The need for ICs can be understood by examining electromagnetic responses of straight nanowires without integrating any coupler. For this purpose, the pair of straight nanowires with $5 \mu\text{m}$ lengths, whose other geometrical parameters are given in Table 4.1, is excited as explained in Section 4.3. Electric field intensity, magnetic field intensity, and power density in different regions, including the output frames are shown in Figure 4.4. Distributions in the first column, namely in the output frame, correspond to field and power plots in the measurement frame, which is transverse to the propagation direction of SPPs. Distributions in the second and third columns are the results obtained when field and power density calculations are performed at a plane lying on the x - y plane and bisecting the geometry. By examining the results in Figure 4.4, it can be assessed that SPPs are successfully generated on the outer surfaces of the nanowire pair thanks to the coupling of optical waves emitted by dipoles

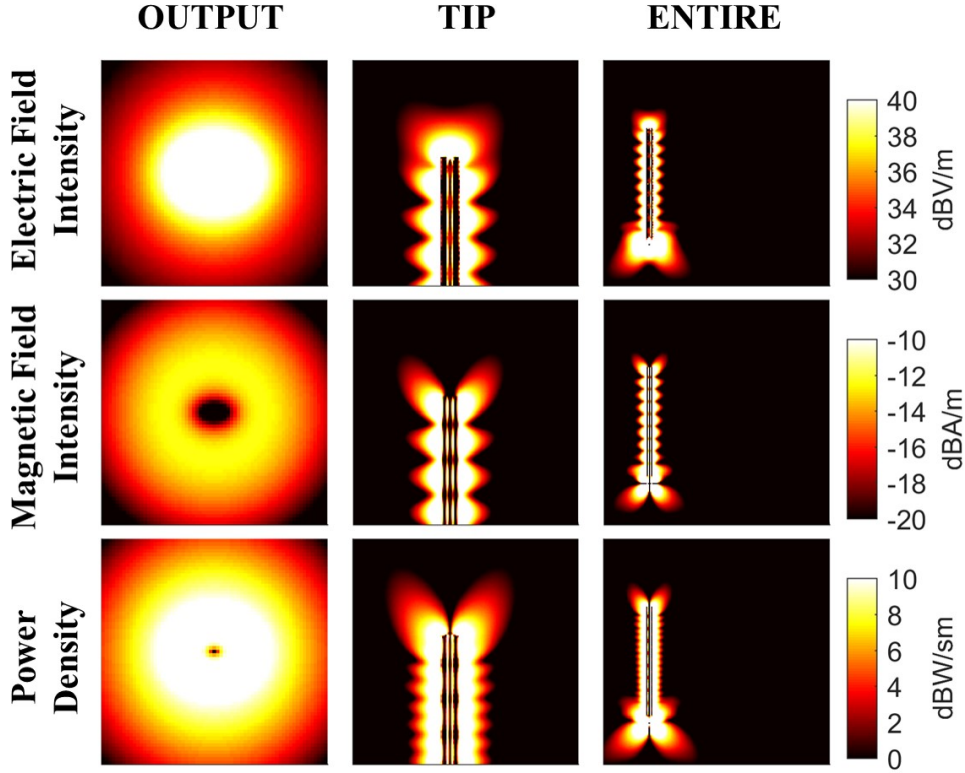


Figure 4.4: Electric field intensity, magnetic field intensity, and power density for different regions and in the output frames when straight nanowires of $5 \mu\text{m}$ are excited via Hertzian dipoles at 250 THz.

to the metallic surfaces of the nanowires. Moreover, the waves transmitted through the nanowires are strongly confined in the vicinity of metallic surfaces. This confinement provides both efficiency for power transmission by avoiding the dispersion of waves and opportunity for placing other optical devices nearby the nanowire pair with minimum cross-talks. As can be seen in field and power distributions in the output frame, the symmetric pattern created by dipoles at the input tips of the nanowires is successfully transmitted to their output tips, which can be considered as a useful property in terms of information transfer. Considering the power transmission ability, guidance of SPPs along nanowires leads to a significant transmission, as it is apparent at the end tips of the nanowires. Specifically, mean and maximum values of the power density in the output frames are equal to 7.908 dBW/m^2 and 12.84 dBW/m^2 , respectively, thanks to the propagation of SPPs along nanowires. It should be noted that the mean and maximum values of the incident power density in the output frame

are measured as -21.541 dBW/m^2 and -17.192 dBW/m^2 , respectively. Considering that the optical waves emitted by the source tend to attenuate in vacuum until they are captured by the nanowires and strong diffractions occur at the input, the power transmission ability of straight nanowires is open to improvement via efficient ICs. In the following sections, IC designs for various cases involving the straight nanowires in Figure 4.3 (with the electromagnetic response given in Figure 4.4) are examined, while the results shown in Figure 4.4 are considered as reference for the evaluation of the designed couplers.

4.3.2 Design of ICs for Different Layouts

Dimensions and the array configuration of the optimized coupler, and accordingly the number of used cubes are crucial parameters that affect the coupling of emitted waves to nanowires. One can expect that performing optimization trials with larger layouts of nanocube distributions provides an opportunity to find an individual with a better fitness value thanks to the enlarged optimization space. However, as the optimized coupler involves more particles, it becomes more complex, and the compactness of the overall system diminishes. Considering these, optimization trials using six different layouts of nanocube distributions shown in Figure 4.5 are performed to investigate the relationship between the coupler size and the performance of the designed IC. At the same time, efficiency of the optimization tool introduced in Chapter 3 is analyzed for various cases of IC optimization. Optimization trials are performed for the pair of straight nanowires illustrated in Figure 4.3, whose results are presented in Figure 4.4.

In Figure 4.5, optimization histories (fitness values with respect to generations) for six different cases and the corresponding layouts are shown. Numbers of particles in these layouts are gradually increased by adding outer layers. Nanocubes are distributed around nanowire tips and in the gap between them. This way, a cavity is constructed around the source and nanowire tips. The smallest layout contains only 26 nanocubes (case 1), five of which are distributed in the gap between the nanowires and the others are placed around the tips with a single layer. Layouts with 51 cubes (case 2), 80 cubes (case 5), and 113 cubes (case 6) are obtained by consecutively

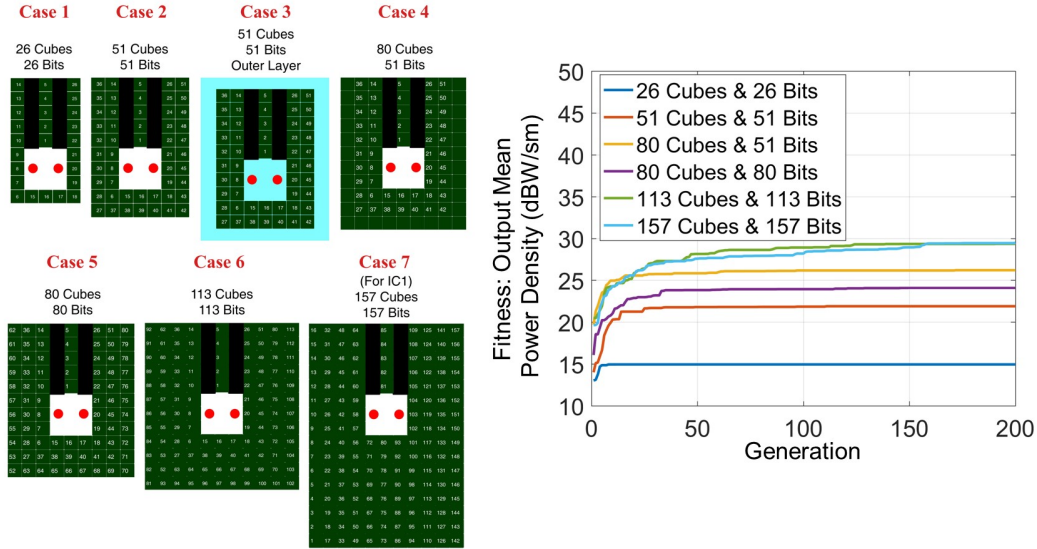


Figure 4.5: Effect of optimization layouts on the designs of ICs. Optimization histories for six different cases and the corresponding layouts are given.

adding one, two, and three outer layers to the layout of 26 cubes. Another layout containing 157 cubes, namely case 7, is constructed by adding four rows of nanocubes at the bottom of the layout in case 6. Optimization trials are performed separately for each layout of these five cases (case 1, 2, 5, 6, and 7) to analyze the effect of the number and arrangement of cubes on the performance of IC. The optimization trial named case 4 is conducted by using a layout of 80 cubes represented by 51 bits, i.e., the outermost layer in the layout is kept fixed for all individuals and the on-off optimization is conducted only for 51 nanocubes in the interior of this layer. It should be noted that the IC configuration called case 3 does not correspond to a separate optimization trial. It is a modified version of the coupler design obtained in case 2 by adding an outer layer to the optimized configuration.

Figure 4.6 depicts the final coupler configurations for seven different cases and the corresponding power density distributions, in comparison to the no-coupler case, namely case 0. To examine the performance of each case, power density distributions along the entire nanowire system including the sources, in the optimization frame (see Figure 4.3), and at around the tips of the nanowires are presented. In addition to the power density distributions, mean and maximum power density values measured in the optimization frame in each case are given in Figure 4.6. The results

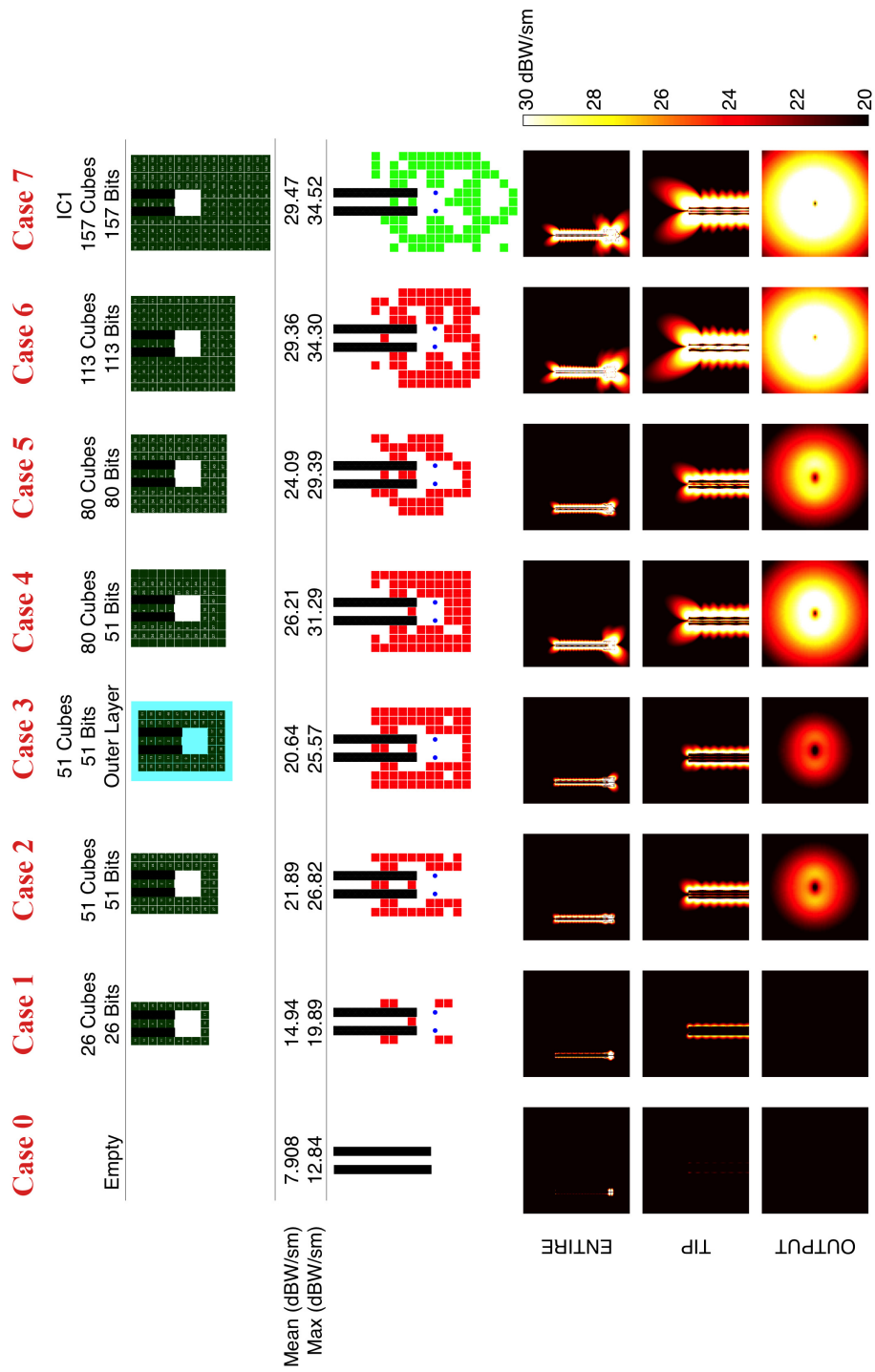


Figure 4.6: Power density distributions for different cases involving no coupler (case 0), optimized ICs for six different layouts (cases 1, 2, 4, 5, 6, 7), and a modified version of the optimized coupler of case 2 (case 3).

demonstrate the efficiency of the optimization tool that enables significant improvements with respect to the no-coupler case when the optimized couplers for various layouts are integrated into the nanowire system. Specifically, starting with a layout of 26 nanocubes (case 1), the optimized coupler configuration involving only 9 nanocubes achieves 14.94 dBW/m^2 mean power density and 19.89 dBW/m^2 maximum power density in the optimization frame. These correspond to 7.03 dBW/m^2 and 7.05 dBW/m^2 increases in the mean and maximum power density values, respectively, in comparison to the no-coupler case. As the optimization trials are carried out using larger layouts, such as case 2 (51 cubes), case 5 (80 cubes), case 6 (113 cubes), and case 7 (157 cubes), the coupler designs provide much better power transmission. Using the layout with two layers (51 cubes, case 2) around the nanowire pair, the optimized coupler provides 13.98 dBW/m^2 improvement in the mean power density, while the coupler optimized by using the layout with three layers (80 cubes, case 5) achieves a significant improvement of approximately 16.18 dBW/m^2 , in comparison to the no-coupler case. Among all these cases, superior transmission abilities are obtained with the optimization trials carried out by using the layouts of case 6 and case 7, containing 113 cubes and 157 cubes, respectively. Specifically, using 157 nanocubes, the fitness value (mean power density) reaches 29.47 dBW/m^2 , while the coupler with 113 nanocubes provides 29.36 dBW/m^2 . These correspond to improvements of nearly 21.5 dBW/m^2 for the mean power density with respect to the no-coupler case. Although the numbers of particles included in the final designs are different for these two cases (cases 6 and 7), the mean power density values measured in the output frame are very close to each other, as stated above. Using these two couplers, the amplitudes of the waves transmitted along the nanowires are considerably enhanced, in comparison to the amplitudes obtained with the other couplers. These results reveal that including more particles in the optimization layout may provide couplers with better transmission abilities due to the enlarged optimization spaces. However, after some certain size, expanding the layout may not be feasible due to the additional manufacturing costs and reduced compactness.

Regarding the effect of the optimization space and the size of the initial layout on the performance of the optimized coupler, further observations can be made by comparing the results presented in Figures 4.5 and 4.6 related to the cases 2, 3, 4, and 5.

When an outer layer is added to the optimized coupler of case 2, although the size of the coupler is increased, a significant deterioration is observed at its performance, i.e., the power density transmitted to the output frame decreases from 21.89 dBW/m² to 20.64 dBW/m² in terms of the mean value. More interestingly, the optimization trial in case 4, which is carried out for 51 bits by using a layout of 80 nanocubes (with 29 cubes at the fixed outermost layer), the designed coupler provides much better transmission in comparison to the couplers of cases 2 and 3. Specifically, the mean power density obtained in case 4 is 4.32 dB larger than that in case 2 and 5.57 dB larger than that in case 3. By considering these, the efficiency of IC can be said to be more related to the proper selection of the array configuration rather than simply the size of the optimization space. This proves the necessity of a rigorous optimization for finding an adequate array configuration for an IC that provides satisfactory performance.

4.3.3 Investigation of the Performance of the Optimized IC (IC1)

To investigate the performances and operating principles of the optimized ICs, the coupler corresponding to the layout of 157 nanocubes, called IC1, is analyzed further. Once the optimization trial is finalized, the specific nanocube arrangement for the optimized coupler is obtained such that it can provide efficient coupling between the sources and nanowires. This is mainly due to two major factors, i.e., the interaction of each particle with the waves radiated by the emitter and the extraordinary interactions between the particles due to their enhanced plasmonic properties.

To examine the effect of each particle, an importance graph is generated as depicted in Figure 4.7. In this analysis, each bit in the finalized chromosome of IC1 is inverted one by one (e.g., inversion from one to zero corresponds to the extraction of the related cube, while inversion from zero to one corresponds to the addition of the related nanocube) and the modified coupler is analyzed to measure the effect of the converted bit on the transmission ability of the overall system. Hence, a total of 157 analyses, each corresponding to the inversion of a bit, are performed by integrating the modified couplers into the nanowire system and calculating the updated fitness values. For each nanocube, the fitness value represents its importance on the overall performance

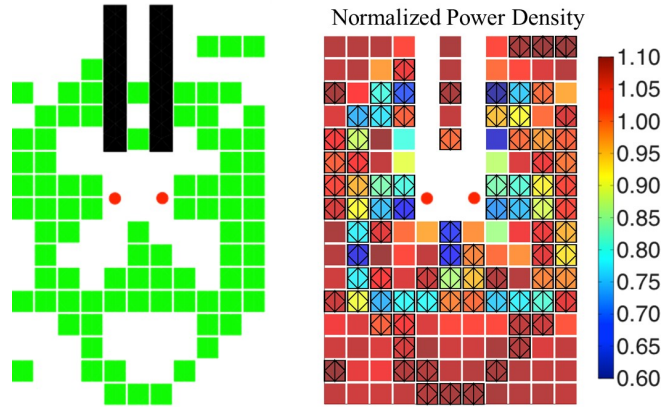


Figure 4.7: Importance graph (effect of each nanoparticle in IC1 on the fitness).

of the coupler, i.e., how much the fitness value of the original coupler is affected by the change of the existence or absence of the corresponding nanocube. In Figure 4.7, the importance of each particle is indicated by a color in the range from 0.6 to 1.1. These values correspond to the fitness values obtained for each case normalized by the fitness value obtained for the original case. For example, a value of 0.9 indicates that the inversion of the existence or absence of the associated nanocube, while the rest of the nanocubes are kept fixed as in the optimized coupler, results in a modified coupler providing a fitness value (mean power density in the optimization frame) that is equal to the 90% of the fitness value achieved with the original configuration of the optimized coupler. Values above unity indicate that extraction or addition of the corresponding nanocubes lead to improvements on the coupler performance, while values below unity correspond to deteriorations. In Figure 4.7, the nanoparticles, which originally exist in the optimized coupler (particles whose corresponding bit values in the final chromosome are equal to 1), are shown with black edges together with their colors.

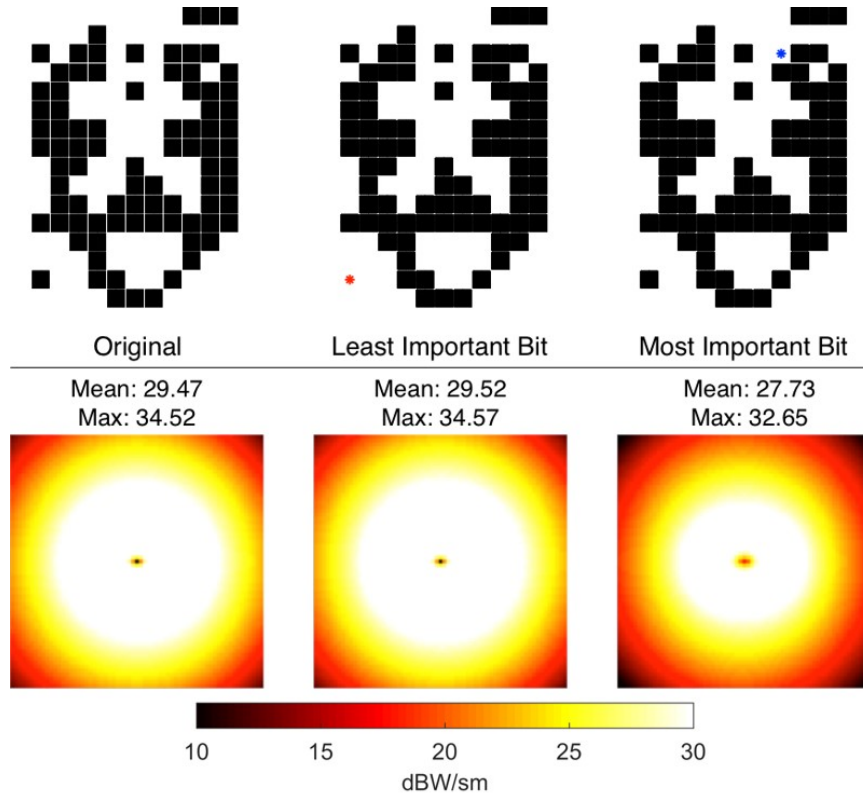


Figure 4.8: Power density distributions for two modified couplers corresponding to the inversion of the least and most important bits, in comparison to the original case.

Regarding the results, it can be stated that the most important bits are generally those close to the sources and nanowire tips. The nanocubes far from the input tips of the nanowires have mostly red color, indicating that they have minor effects on the performance of the overall coupler. In Figure 4.8, power density distributions for the couplers corresponding to the inversion of the most and least important bits are presented, in comparison to the original result. The coupler geometries after the inversion (extraction) of the corresponding bits are also shown, where the extracted nanocubes are represented by colored asterisks. When the results are examined, it can be observed that even the inversion of a single bit may result in a significant decrease in the power transmitted to the output frame. More specifically, extraction of a nanocube corresponding to the inversion of the most important bit leads to a decrease in the output mean power density from 29.47 dBW/m² to 27.73 dBW/m². This is indeed as another evidence on the necessity of a proper optimization to obtain well-designed configurations of nanoparticle arrays. Besides these, there may be nanocubes with

relatively less significant effects on the efficiency of the optimized coupler, such as the one corresponding to the least important bit in Figure 4.8. Once the optimization is completed, these less effective nanocubes can be eliminated with the help of a post-process analysis, such as the importance graph, to reduce the complexity of the designed coupler.

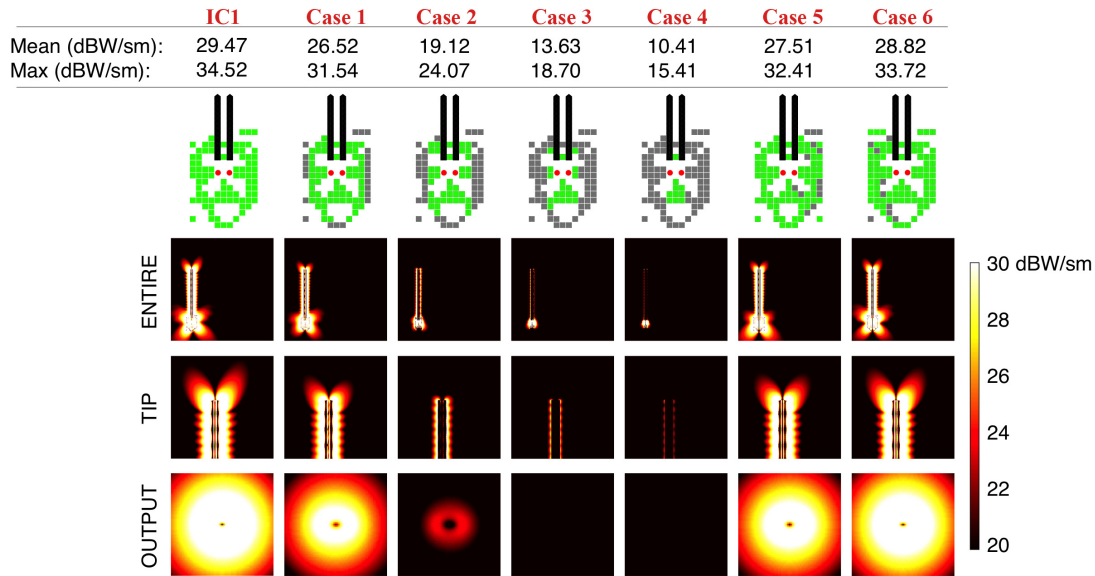


Figure 4.9: Power density distributions for six modified couplers obtained either by eliminating some of the nanocubes (cases 1–4) or symmetrizing the array (cases 5 and 6) of IC1.

Further tests are performed on the elimination of nanocubes of the optimized coupler IC1, while considering its importance graph. Figure 4.9 presents the results for four different cases of particle elimination. Nanocubes are systematically removed starting from the outermost layer to the inner layer, e.g., case 1 corresponds to the coupler obtained when a single (outermost) layer is removed, case 2 corresponds to the coupler obtained when two layers are removed, etc. In Figure 4.9, the nanocubes extracted from the original coupler are shown with gray color, while the ones kept are shown with green. We observe that, as the size of the optimized coupler is reduced, the strength of the power propagating along the nanowires significantly decreases, leading to diminished power transmitted to the output frame. For example, the mean power density decreases from 29.47 dBW/m² to 10.41 dBW/m² when the coupler configuration of case 4 is integrated into the nanowire system rather than using IC1.

However, the mean power density value provided by the coupler of case 4 is still much greater than the value achieved without a coupler. Considering these results, it can be stated that, depending on the application and requirements for the size and performance of the coupler, it is possible to increase the compactness of the coupler by eliminating the nanocubes, as long as the deterioration on the transmission abilities is acceptable. Obviously, design of couplers with restricted dimensions is always possible by performing the optimization trial with a limited starting layout as presented in Section 4.3.2, while elimination via post-processing seems to be an attractive alternative.

Finally, the results presented in Figure 4.9 involve two more attempts performed to make the coupler design symmetric. It should be noted that the ultimate coupler should actually be symmetric considering the symmetry of nanowires, while symmetric configurations are not enforced in GAs so that optimization trial may converge locally to a non-symmetric design, as in the case of IC1. Removing nanocubes to make the design symmetric, the mean power density decreases to 27.51 dBW/m² and 28.82 dBW/m² that are comparable to 29.47 dBW/m² of the original design (IC1). Alternatively, symmetry can be enforced in optimization trials, as presented in the next section.

4.3.4 Design of ICs with Symmetrical Configurations

The problem introduced in Figure 4.3 involves a pair of straight nanowires excited by Hertzian dipoles, whose placements and orientations are adjusted in a way that the symmetric pattern created by the dipoles at the input tips of the nanowires can be transmitted to the output of the nanowires via the propagating modes of SPPs. This electromagnetic response of the pair of straight nanowires without using any IC is already presented in Figure 4.4. Due to the symmetry of the problem, the waves propagating over the surfaces of the nanowires are superposed at the output of the tips of the nanowires and axially symmetric patterns for the power density and field intensities are achieved in the output frame. To obtain perfectly symmetric patterns in the output frames, the phases of the propagating waves on separate nanowires should be well-balanced. Once the optimized ICs are inserted into the input region, the ampli-

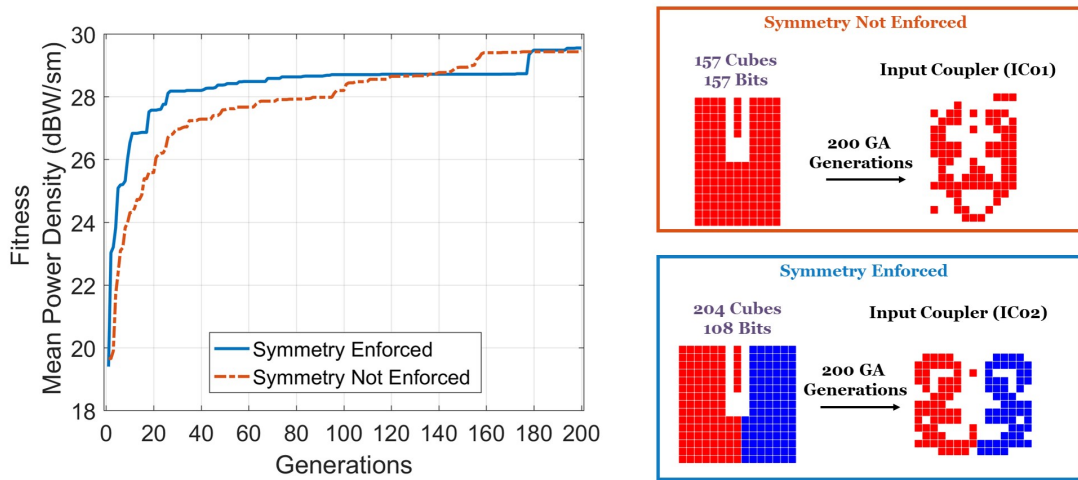


Figure 4.10: Optimization history for the trial performed by enforcing the symmetry of the coupler (IC2), in comparison to the history for IC1 (see Figure 4.6, case 7). Corresponding optimization layouts and the optimized configurations are shown on the right-hand side.

tudes of the waves bounded on the surfaces of nanowires are significantly amplified, but phase differences may occur due to the asymmetry of ICs. In fact, as stated in Section 4.3.3, a symmetric configuration should be the ultimate design provided by the optimization tool. However, as can be seen from the configurations of the optimized couplers, the optimization tool provides designs with non-symmetrical configurations since the final results are not globally optimized structures. Post-processing for making design IC1 symmetric leads to slight deteriorations on the performance of the optimized coupler, as presented in Section 4.3.3.

On the other side, the symmetry of the coupler can be enforced during an optimization, if symmetry is a design constraint. For this purpose, optimization trials are performed with the same parameters of the optimization tool (see Table 4.3) and the full-wave solver (see Table 4.2), as well as using the same nanowire geometry and the excitation (see Table 4.1). Figure 4.10 includes the optimization history to obtain a symmetric configuration of IC, as well as the optimized coupler design at the end of 200 generations, in comparison to those for the non-symmetric case of IC1. For comparisons, the layouts used in the optimization trials are also shown in the figure. The initial layout for the symmetric case containing 204 cubes distributed at

around the nanowire tips and the sources is determined based on the interpretations and facts gathered by examining the importance graph of IC1. On-off optimization is performed by using 108 bits corresponding to the particles at only one half of the optimization layout. The results for the coupler optimized by enforcing symmetric configuration, called IC2, is compared with the results of IC1.

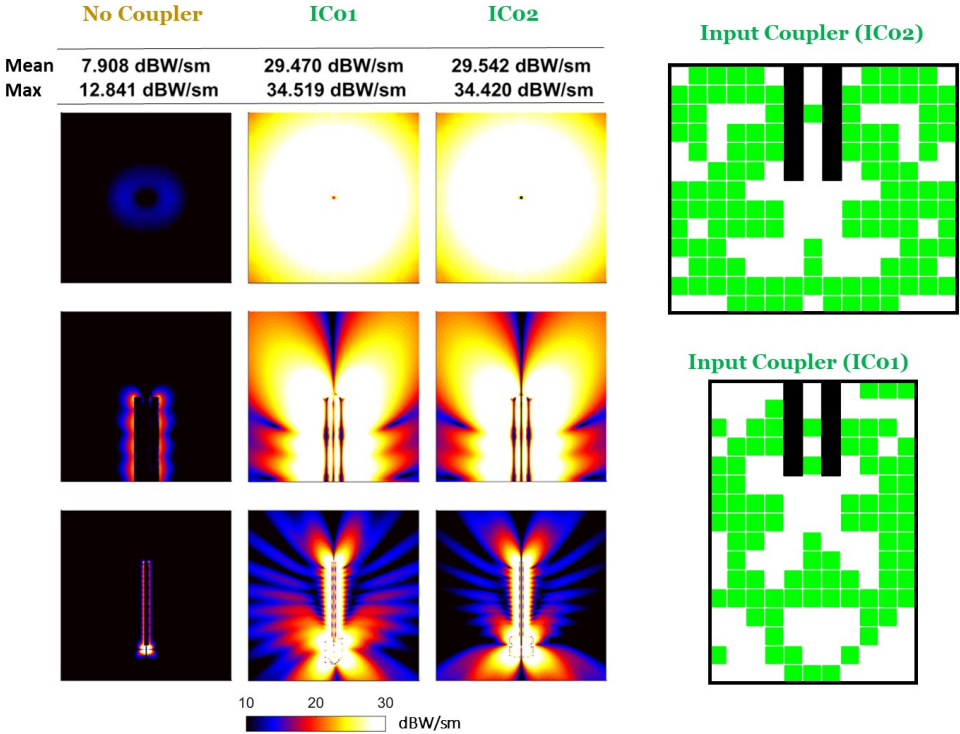


Figure 4.11: Power density distributions when IC1 and IC2 are attached to the straight nanowires shown in Figure 4.6, in comparison to the no-coupler case.

When the optimization histories for the optimization trials of IC1 and IC2 are compared, it can be stated that, despite discrepancies are observed, fitness values of the best individuals in the 200th generation are very close to each other, i.e., the coupler IC2 leads to a fitness value of 29.55 dBW/m², while this value is 29.47 dBW/m² for the case of IC1. This can be seen as another evidence for the stability of the optimization tool, i.e., similarly successful results can be obtained with different trials of optimization to improve the transmission abilities of straight nanowires as long as the starting layout for the distribution of nanocubes is selected properly.

Power density distributions for these two cases, namely IC1 and IC2, are presented in Figure 4.11. For both symmetric and non-symmetric cases, propagating SPPs are

considerably amplified in comparison to the no-coupler case. In addition, for both cases, mean power density values provided in the output frames are improved by approximately 21.65 dBW/m² with respect to the no-coupler case. However, a perfectly symmetric pattern is achieved by using the coupler with the symmetric configuration (IC2). Such type of a symmetry may be very crucial depending on the nano-optical application.

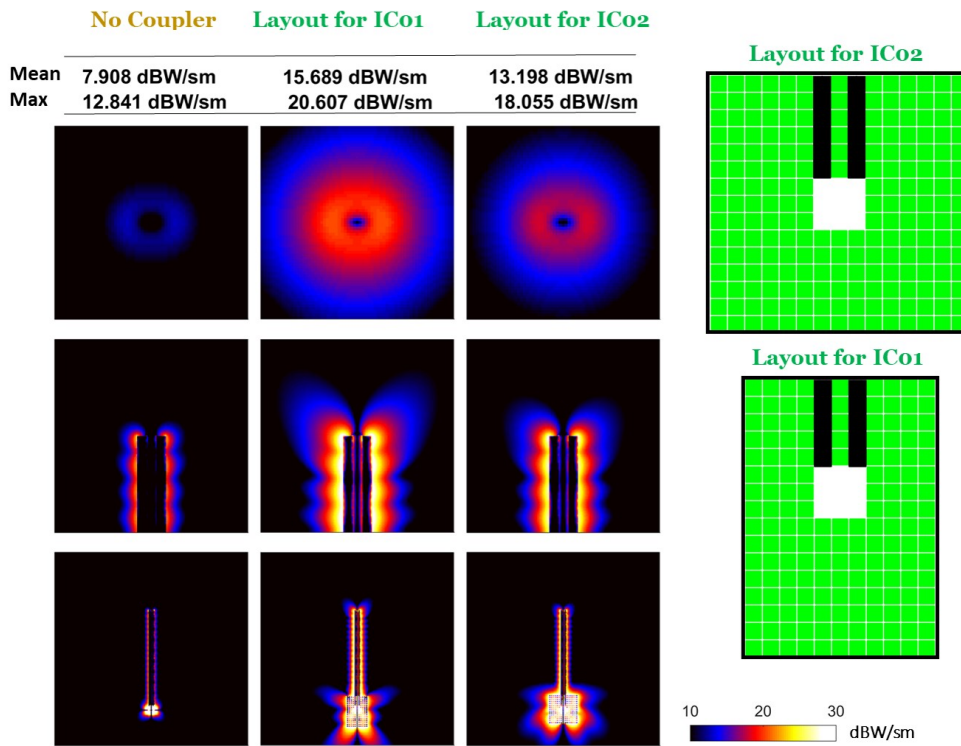


Figure 4.12: Power density distributions when the full arrays corresponding to the layouts of IC1 and IC2 are used as couplers, in comparison to the no-coupler case.

4.3.5 Performances of Full Arrays as ICs

One may ask whether full nanocube arrays can be used as couplers instead of complicated optimization of the arrays. To investigate this, full arrays of nanocubes corresponding to the optimization layouts of IC1 and IC2 are attached to the pair of straight nanowires. The corresponding power density distributions are illustrated in Figure 4.12. We observe that the integration of full nanocube arrays without any optimization provides significant improvements in the power transmitted to the output

frame in comparison to the no-coupler case. Specifically, with the use of full array couplers, the mean power density values of 13.19 dBW/m² and 15.69 dBW/m² are measured in the output frames for the cases (layouts) of IC1 and IC2, respectively. However, considering the successful results for the couplers with the optimized configurations presented in Figure 4.11, coupler designs obtained with the optimization tool achieve much better performance with less numbers of nanocubes than the full-array couplers, which means achieving better transmission abilities with less material. This can be considered as another evidence for the necessity of IC optimization and the efficiency of the optimization tool.

4.3.6 Compatibility of the Optimized ICs for Different Lengths of Straight Nanowires

In real-life applications, it is well-known that, with their enhanced plasmonic properties, nanowires provide high-quality transmission of electromagnetic waves, which are tightly confined to the metallic surfaces in transversal planes, up to several to tens of microns in the axial direction, e.g., 1–20 μm [2]. When building complex nanowire networks or nano-optical links, nanowires with different lengths may be necessary depending on the application. In Sections 4.3.2 and 4.3.4, it was shown that the use of well-designed ICs around nanowire tips and sources provides significant improvements in the transmission quality of nanowires. Considering that the presented ICs are designed for specific lengths of nanowires (5 μm), their compatibilities with different lengths of straight nanowires are also crucial. To investigate this issue, the performance of IC2 is examined by combining it with straight nanowires of different lengths. A separate analysis for each length of the nanowires, ranging from 1 μm (0.8333 λ) to 10 μm (8.333 λ) μm with a step size of 0.1 μm (0.08333 λ), is performed when IC is integrated (with-coupler) and not integrated (no-coupler). The results are compared in terms of the mean power density measured in the measurement (optimization) frame.

Mean of the power density values measured in the measurement frame for both no-coupler and with-coupler cases with respect to the length of the nanowires are presented in Figure 4.13. Moreover, the increase in the mean power density with respect

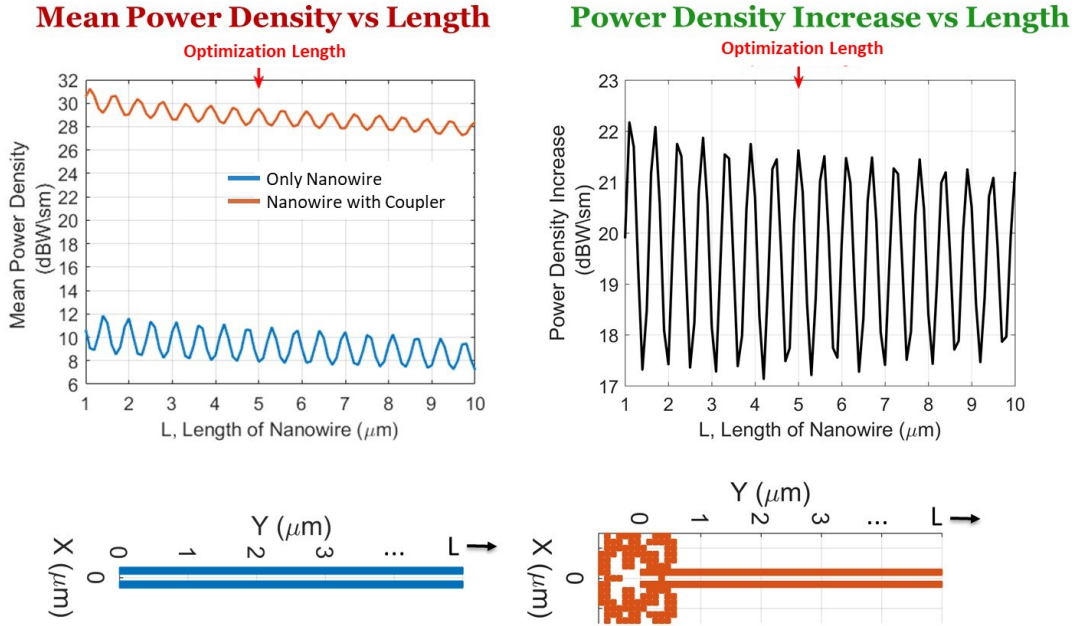


Figure 4.13: Performance of IC2 for different lengths of straight nanowires.

to the no-coupler case is also presented. When the results are examined, it is remarkable that IC2, which is optimized by using a pair of straight nanowires of $5 \mu\text{m}$ length, still provides very good performance for other lengths of the nanowires. Specifically, the improvement in the mean power density changes from 17.1 dBW/m^2 to 22.1 dBW/m^2 for different lengths, while this improvement is equal to approximately 21.63 dBW/m^2 when the length is exactly $5 \mu\text{m}$. These results can be seen as another other evidence for the efficiency of ICs and the optimization tool that is used to obtain the design. Moreover, the high compatibility of the designed ICs with nanowires of different lengths enables their flexible usage in complex networks. Performing separate optimization trials for various nanowire lengths starting from the initial layout or making fine tunings on the optimized coupler designs are also possible if the increase in the computational load (due to repeated optimization trials) is acceptable.

4.3.7 Frequency Response of the Optimized ICs

The optimized couplers, such as IC1 and IC2 (see Figure 4.11), are also examined with respect to the variation of frequency. Performances are particularly investigated

in a range of frequencies from 200 THz to 300 THz, which correspond to near-infrared frequencies. Mean and maximum values of the power density are computed at the sampling points of the measurement frame for both optimized couplers IC1 and IC2 and presented in Figure 4.14, in comparison to the case of nanowires without an IC.

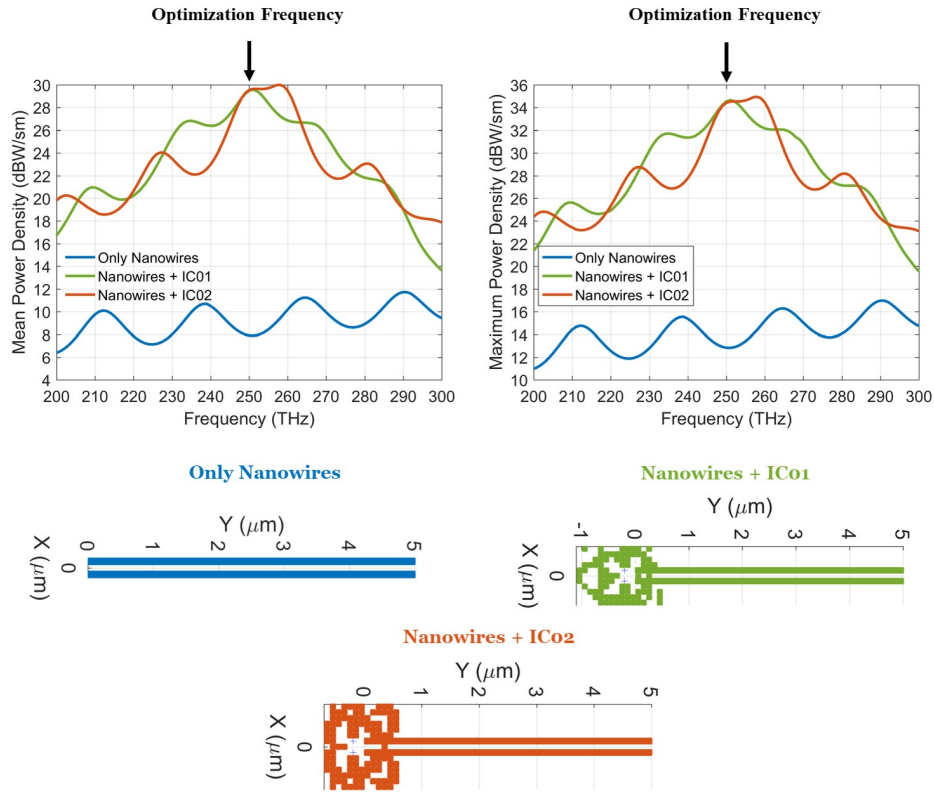


Figure 4.14: Performances of IC1 and IC2 in a range of frequencies from 200 THz to 300 THz.

Taking into the account that ICs, such as IC1 and IC2, are optimized at the frequency of 250 THz, the best performances for the couplers are achieved near the optimization frequency, which is shown with black arrows in the figure. However, their substantial contributions to the transmission ability of the nanowires can be observed in the whole frequency range from 200 THz to 300 THz. Specifically, for both ICs, mean power density values above 20 dBW/m² are achieved from nearly 220 THz to 288 THz, while in the same range, the corresponding values change in the 6–12 dB range for the no-coupler case. Similar values of efficiency are also obtained for the maximum power density values. When the performances of the two couplers are com-

pared against each other, IC2 achieves better transmission ability in a wider range of frequencies around the optimization frequency in comparison to IC1. However, in general, the performances of both couplers can be considered to be very similar to each other.

4.4 Design of Efficient Couplers for Improving Transmission Through Sharp Bends

Once nanowires are excited by external sources and propagating modes of SPPs are generated on their metallic surfaces, electromagnetic energy can flow along them up to several to tens of μm , e.g., for 1–20 μm , unless they are attenuated to undetectable levels due to propagation losses and diffractions. For example, propagation of SPPs along metallic surfaces of bent nanowires significantly deteriorates due to reflections and diffractions at bending regions, while the power transmission to the outputs drops down [17]. Considering the need for further miniaturization of optical devices as the technology advances, bending of nanowires is inevitable to construct complex nanowire networks with compact designs at the expense of deteriorations on power transmission [16, 46]. Moreover, such types of bends in practice may lead to additional deformations on nanowire surfaces, further reducing the transmission of power. Consequently, distortion of the electromagnetic energy flow due to the bends is among the major issues that need to be solved to design and construct complex nano-optical links and networks. Several studies have been performed on the modeling of bending effects via mathematical expressions and experimental results, particularly considering plasmonic propagation along curved nanowires [7, 47, 48]. It is known that leakage losses occurring at bending regions can be decreased by using smooth bends rather than sharp corners. But such type of smoothing may result in some limitations in practice. First, even though fabrication examples can be found in the literature, smoothing nanowires may not be very practical in all fabrication setups. Second, for sufficiently good transmission levels, large values for the radius of curvature are often needed, reducing compactness. Third, smoothing operation needs to be customized depending on the dimensions of the considered transmission line, which may make smoothly bent nanowires highly specialized and not suitable to be used as

building blocks of nanowire networks. Considering all these limitations, instead of performing geometrical modifications on the geometry of nanowires, utilizing compact structures, such as couplers that consist of nanoparticles, at the corresponding bending regions can be considered as a more feasible and favorable solution to improve the transmission abilities of bent nanowires. In this section, extensive analysis and optimization results are presented related to the design of such type of couplers, namely corner couplers (CCs), to increase the power transmitted to outputs of bent nanowires by decreasing the leakage of electromagnetic energy through bends. Optimization tool, proposed in Chapter 3, is used for finding the optimum configuration of the nanoparticle arrays to achieve enhanced efficiency for power transmission.

4.4.1 Details Related to Optimization of CCs

In this section, analysis and optimization of CCs are mostly performed by utilizing a pair of $10\ \mu\text{m}$ bent nanowires with 90° sharp bends at the middle. Some of the parameters related to the geometry, excitation, and the overall electromagnetic problem are fixed as given in Section 4.2. In Figure 4.15, the placement of the bent nanowires is shown together with the fixed parameters. It should be noted that, unless stated otherwise, the parameters shown in Figure 4.15 and introduced in Table 4.1 are used for the analysis and optimization results.

In Figure 4.15, the CC region, in which an efficient coupler design is sought, is shown with a rectangular red dashed line. Arrays of silver nanoparticles, whose electrical properties are as given in Table 4.1, are considered for the optimization of CCs. In most cases, dimensions of each array particle are limited to fit into a cube with 90 nm edges, while coupler designs involving proper configurations of nanoparticles with different shapes, such as cubes, cylinders, and spheres are investigated. The results for the transmission abilities of nanowires involving various designs of CCs are examined by comparing the power values transmitted to the measurement (optimization) frame. As shown in Figure 4.15, the values of the parameters related to the optimization frame, such as the sampling rate for the calculation of fields and power density values, dimensions of the frame, and the distance between the nanowire output tips and the measurement frame, are selected same as those in the optimization trials of

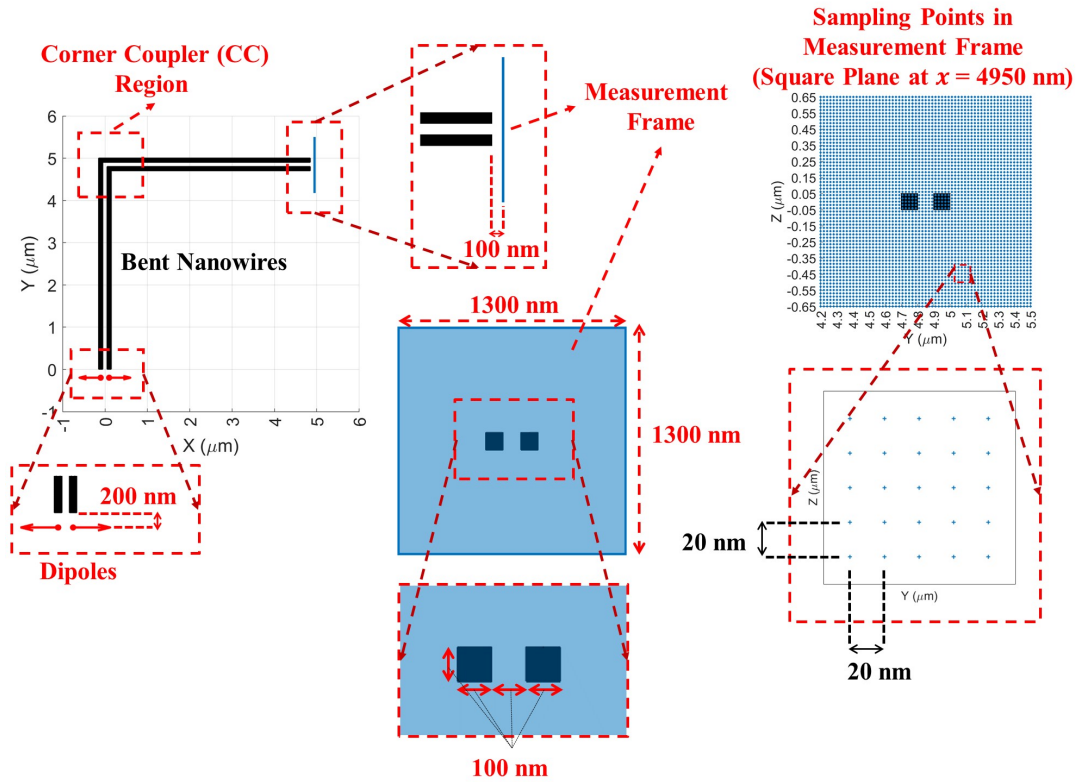


Figure 4.15: A pair of nanowires with 90° sharp bends considered in CC optimization trials and the corresponding measurement (optimization) frame, in which the power density values are computed.

ICs. Various cost functions, which are designed by using the power density values calculated at the sampling points in the measurement frame, are considered. Optimization trials, presented in this section are carried out by using the optimization tool proposed in Chapter 3 with the optimization parameters given in Table 4.3, while the required full-wave solutions of the individuals are performed by using the MLFMA solver introduced in Chapter 2 with the solver parameters given in Table 4.2.

4.4.2 Power Transmission Abilities of Bent Nanowires with Sharp Bends

To clarify the necessity of CCs, the electromagnetic response of the bent nanowires without an integration of any coupler should be examined. In Figure 4.16, the results are presented for the distributions of the electric and magnetic field intensities, as well as the power density, when the excitation is via Hertzian dipoles at 250 THz as

illustrated in Figure 4.15. The results in the first column, namely in the output frame, correspond to the distributions obtained in the measurement frame. The results in the second and third columns are those obtained when field and power density calculations are performed at a plane lying on the x - y plane and bisecting the geometry, respectively.

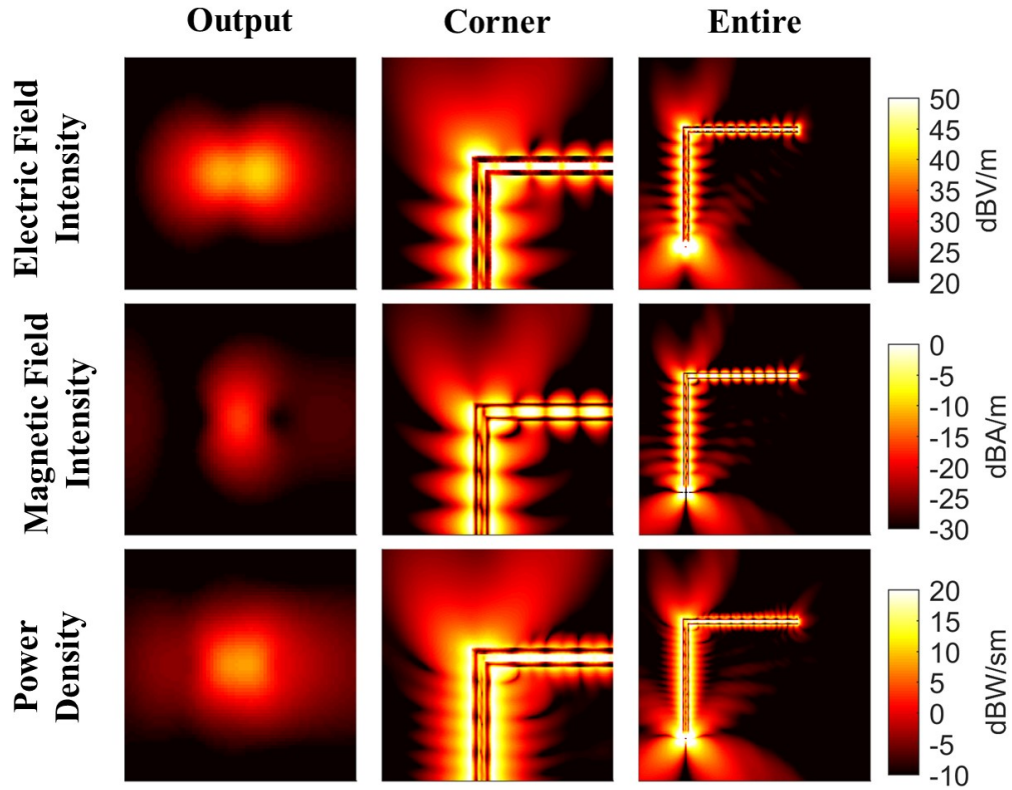


Figure 4.16: Electric field intensity, magnetic field intensity, and power density distributions in different regions when a pair of $10 \mu\text{m}$ bent nanowires involving 90° sharp bends is excited via Hertzian dipoles at 250 THz .

When the results in Figure 4.16 are examined, oscillatory distributions of the electric and magnetic field intensities along the outer surfaces of the nanowires can be seen clearly. As a result of the propagation of SPPs along the nanowires, detectable field and power values are achieved at the output. Specifically, the mean of the power density values at the sampling points in the measurement frame is obtained as -3.0930 dBW/m^2 , while the maximum value is equal to 8.1793 dBW/m^2 . However, the leakage of electromagnetic energy in the corner region is remarkable, which results in significant deterioration on the transmission abilities. Once the nanowires are ex-

cited, SPPs are generated on the outer surfaces and propagate along the nanowires with tight confinement, until they are diffracted and reflected by the sharp bends in the corner region. Significant amounts of guided waves escape from the outer surfaces of the nanowires to the host medium. As a result, the amplitudes of the electric and magnetic field intensities, as well as the power density, are significantly reduced after the sharp bends. In addition, due to the incoherent behavior of the reflections and diffractions in the corner region, the symmetric pattern created by the dipoles at input tips of the nanowires is transmitted to the output with extreme distortions. In the following sections, design of CCs, which are placed in the corner regions to eliminate all these deficiencies in the transmission of electromagnetic energy, is presented. The results presented in Figure 4.16 are considered as references for the evaluation of the designed couplers.

4.4.3 Design of CCs to Improve Power Transmission Through Sharp Bends

Considering the results presented in Section 4.4.2, the design of CCs can be said to be crucial to enhance the power-transmission abilities of nanowires with bends. While designing such couplers, it is possible to improve transmission abilities of nanowires in terms of various aspects, such as the mean power transmission or the maximum power transmission. The transmission abilities can be examined by comparing power values transmitted to output, i.e., into the measurement frame. Since the application itself directly affects the ultimate configuration of nanoparticle couplers, different trials should be performed for different cost functions corresponding to the target parameter to be optimized.

In this section, apart from the design of efficient couplers to enhance the power transmission abilities of bent nanowires, the effects of cost functions on the optimization of CCs are investigated. Two different cost functions are used for the optimization trials, i.e., the mean and maximum of the power density values measured at the sampling points in the measurement frame. As in IC optimization, CCs are designed by starting with an initial layout corresponding to the full array of nanoparticles. Nanocubes with 90 nm edge lengths are considered as the individual particles of the array. The full array corresponding to the optimization layout is constructed as a 13×13 array of

nanocubes, while the particles that coincide with the nanowires are removed, leading to 139 nanocubes to be optimized. Optimization trials are performed by using 139 bits, i.e., existence of each nanocube on the layout is independently determined by the optimization tool.

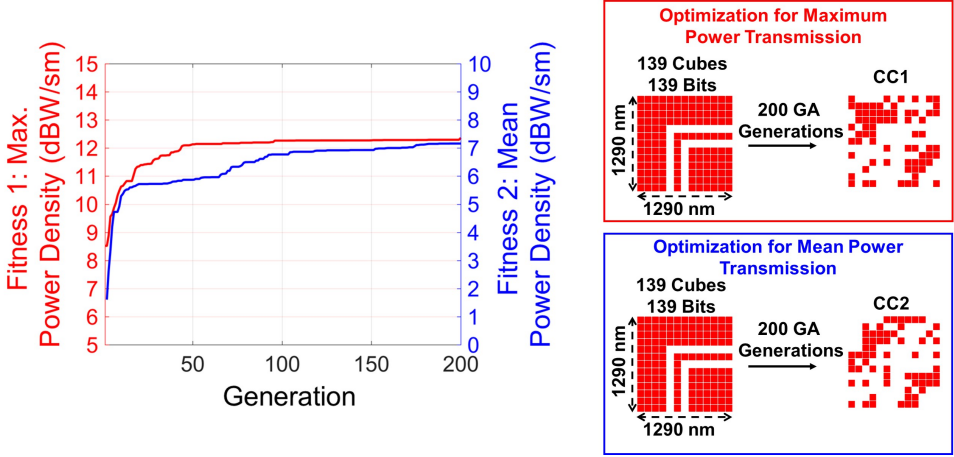


Figure 4.17: Optimization histories for two trials using different cost functions, the optimization layout, and the obtained configurations for the designs after 200 generations.

In Figure 4.17, optimization histories for two different trials using different cost functions, the optimization layout, and the final configurations for the ultimate designs after 200 generations are presented. In this figure, fitness values with respect to generations for different cost functions are shown in the same graph with the different axes, the blue axis corresponds to the cost function for the mean power density, while the red axis corresponds to the cost function for the maximum power density. Significant levels of improvement are achieved for both cases starting from initial generations up to final generations. As a result, two different configurations of nanoparticle arrays are obtained as the ultimate designs of CCs, each of which is designed to enhance the power transmission ability of the bent nanowires for different target properties, i.e., average and maximum power transmissions.

The efficiency of the couplers can further be studied by examining field intensity and power density distributions in comparison to the case involving only the pair of bent nanowires without an integration of any coupler. In Figure 4.18, variation of the electric field intensity along the boundary between the outer surface of a nanowire and

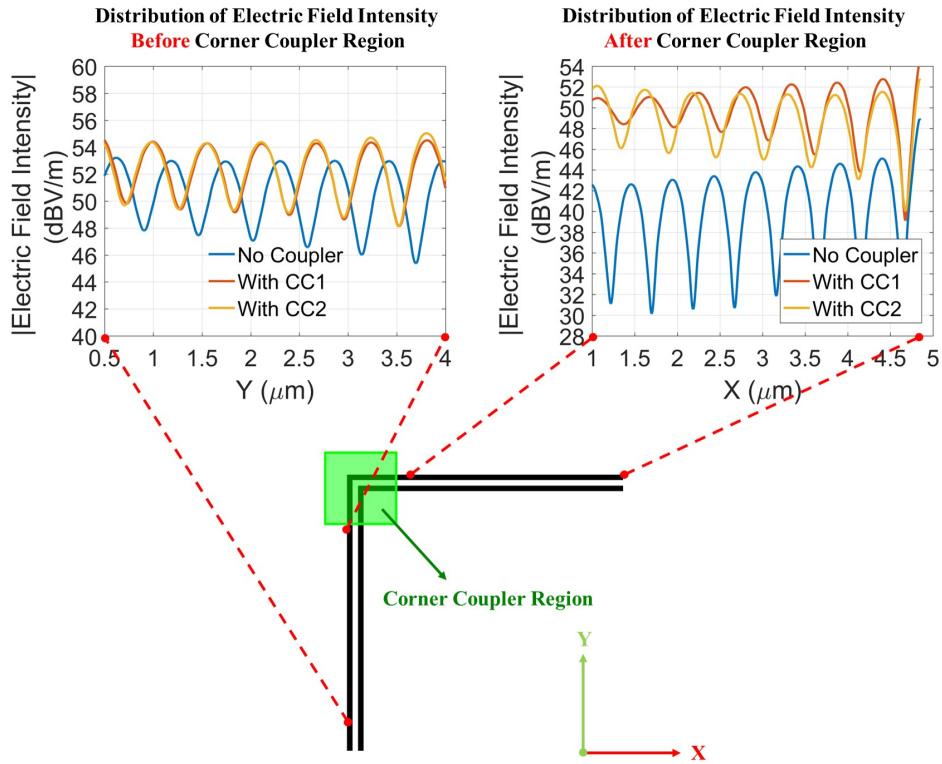


Figure 4.18: Electric field intensity along the nanowire-vacuum interface for different cases involving bent nanowires.

the host medium is presented for different cases, i.e., without a coupler, with CC1, and with CC2. Field values are computed at the sampling points on two separate lines, one of which is along with the y axis corresponding to the field distribution before the CC region, while the other is along the x axis corresponding to the field distribution after the CC region. Distortion of electromagnetic energy flow due to the sharp bend at the corner can be understood by comparing the signal levels in two plots. Specifically, the mean amplitude of the electric field intensity decreases from nearly 50 dBV/m to 38 dBV/m due to the sharp bend. When CC1 and CC2 are integrated into the corner region, however, the signal levels are drastically improved for both cases.

The efficiency of CCs on the transmission ability of the bent nanowires can also be demonstrated by examining the power density distributions, again in comparison to the no-coupler case. The results are presented for three different cases in Figure 4.19. In addition to plots, the mean and maximum values of the power density measured at the sampling points in the measurement frame are also provided. Improvements

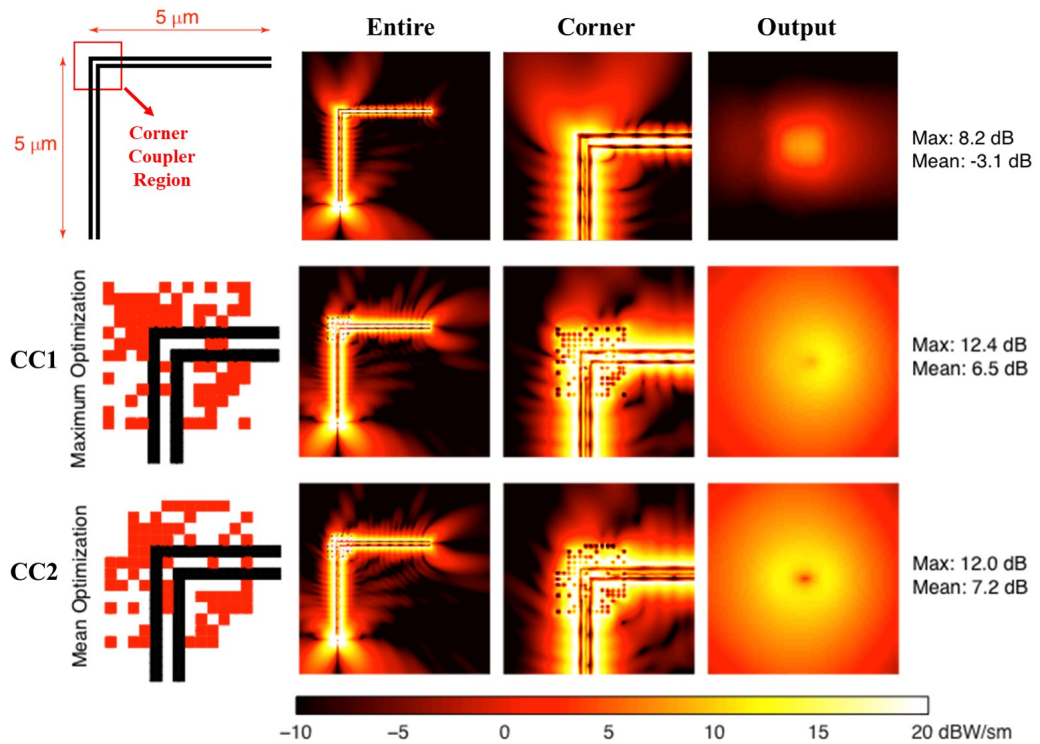


Figure 4.19: Power density distributions in different regions, when CC1 and CC2 are integrated into the corner region of the bent nanowires, in comparison to the no-coupler case.

on the transmission ability of the nanowires with the integration of CCs are apparent in the power density distributions in the corner region. Specifically, escaping electromagnetic waves at the corner are greatly reduced and significant amounts of power are re-coupled to the nanowires after the corner region. When CC1 is integrated into the corner region, a mean power density of 6.5 dBW/m^2 and a maximum power density of 12.4 dBW/m^2 are achieved in the optimization frame. These values are 7.2 dBW/m^2 , and 12 dBW/m^2 , respectively, when CC2 is used. Considering that the mean and maximum power density values are -3.1 dBW/m^2 and 8.2 dBW/m^2 , respectively, without any coupler integration, both couplers can be said to provide significant improvements on the transmission of electromagnetic energy along the nanowire system. When the couplers are compared with each other, we note that optimization trials with two different targets provide different configurations such that the related target parameters can be improved with the integration of the optimized couplers. Specifically, the coupler configuration CC1, which is optimized to improve

the maximum power density provides greater values for this quantity, while the coupler configuration CC2, which is optimized to improve the mean power density, leads to better power transmission in terms of the average value in the output frame. This can be considered as another evidence on the efficiency and flexibility of the optimization tool for different cost functions.

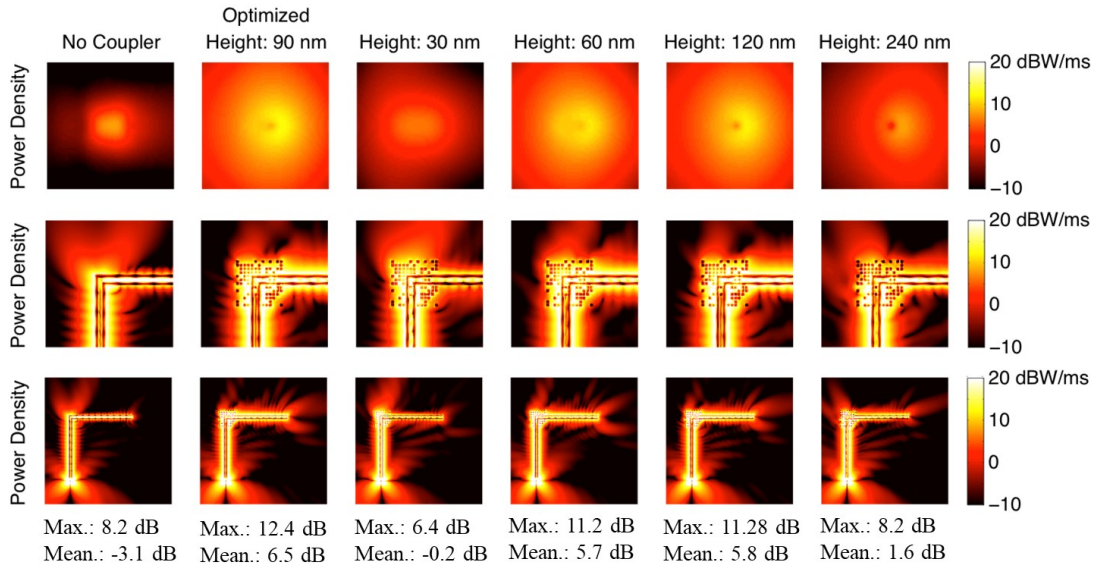


Figure 4.20: Power density distributions in different regions, when the height of the particles of CC1 is altered from 90 nm to 30 nm, 60 nm, 120 nm, and 240 nm.

4.4.4 Effect of Geometrical Properties on the Performance of CCs

Geometric properties, such as shape and size of individual particles, have major effects on the performances of CCs. Naturally, the electromagnetic response of any coupler depends on the geometry of its particles, while CCs can be very sensitive to such geometric properties, as illustrated in this section. The results presented in this section are obtained for CC1, which is optimized to increase the maximum power density in the output frame, while similar interpretations and observations can also be made for other CCs (as well as for other types of couplers).

In Figure 4.20, the power density distributions are presented to see the effect of the height of the particles on the performance of the optimized coupler. The rows in this figure correspond to the power density distributions in different frames, while the

columns correspond to different cases involving the integration of various couplers, as well as the no-coupler case. These different cases are constructed by altering the height of the particles of CC1 from 90 nm to 30 nm, 60 nm, 120 nm, and 240 nm, while their cross sections are fixed as 90 nm \times 90 nm. It is observed that decreasing/increasing the height to 60/120 nm has little effect on the efficiency of the coupler. A relatively poor performance is obtained when the height is changed to 30 nm (one third of the original), while the power transmission even for this case is not worse than the one without a coupler. Increasing the height to 240 nm also leads to visible deterioration in the performance of the coupler, while it still provides improved transmission in comparison to the no-coupler case. These results demonstrate the robustness of the optimized coupler against changes in nanoparticle heights.

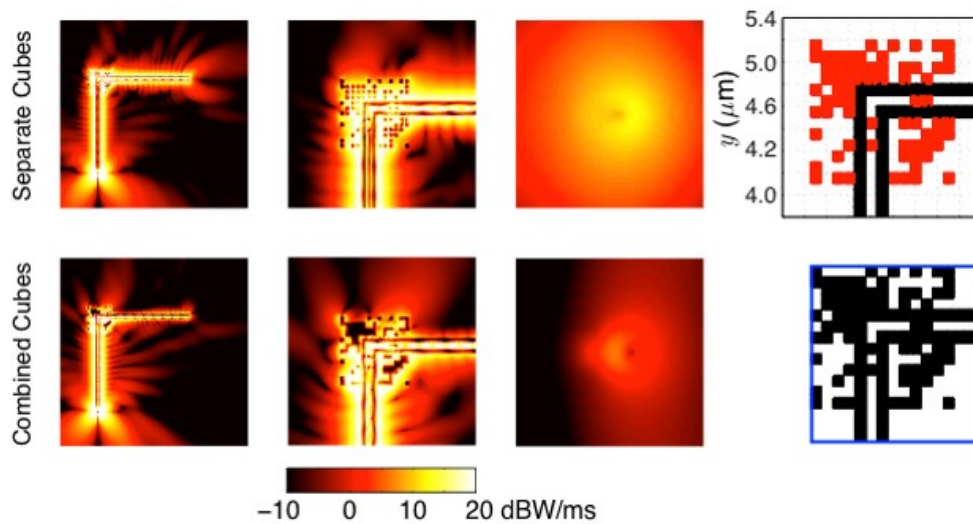


Figure 4.21: Power density distributions when the nearby nanoparticles in the optimal design CC1 are combined, in comparison to the original results.

Once the ultimate design for a CC (or for any type) is obtained, it is tempting to combine adjacent nanoparticles for the ease of fabrication. As an example, Figure 4.21 presents the results when the nearby nanoparticles (nanocubes) in the optimal design of CC1 are combined. Comparing the results, it is observed that the performance of the coupler significantly deteriorates. A close examination in the bending region shows that the coupler with combined nanoparticles operates very differently with cavities, in comparison to the well-designed interactions between separated nanoparticles in the original design.

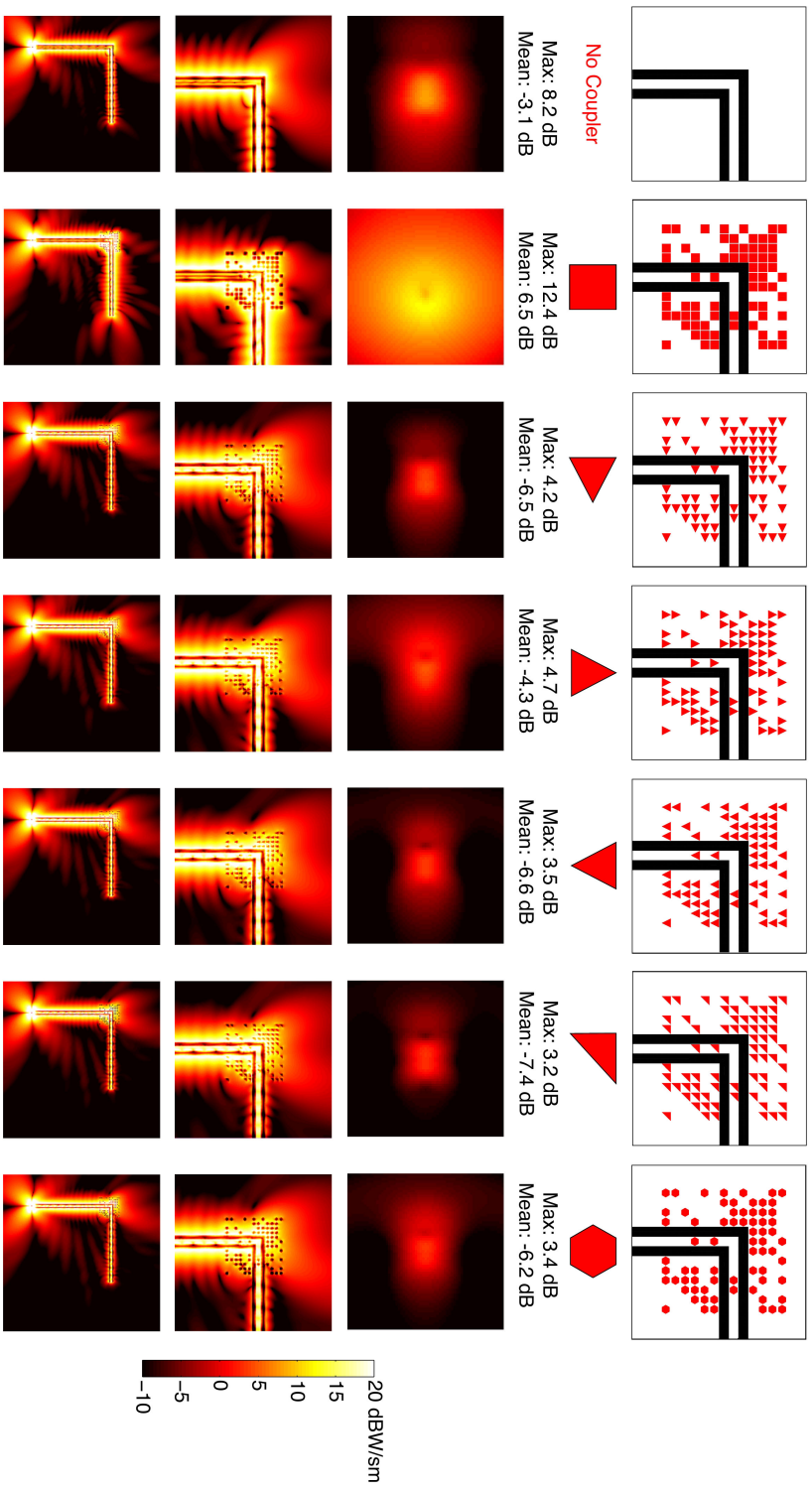


Figure 4.22: Power density distributions when the optimal arrangement of CC1 is used for different nanoparticle geometries.

The sensitivity of the optimized couplers to the shape of the individual particles is another issue that should be investigated. For this purpose, the array configuration of CC1 is used to construct couplers with nanoparticles of five different shapes, while the size of each particle is limited to fit into a $90 \text{ nm} \times 90 \text{ nm} \times 90 \text{ nm}$ cube. Corresponding power density distributions, as well as mean and maximum power density values measured in the output frame are given in Figure 4.22, in comparison to the results obtained without coupler (the first column) and with CC1 (the second column). It can be assessed that the performance of the coupler is highly sensitive to the shape of its particles. Specifically, despite that the same configuration is used, the power transmitted to the output is significantly decreased when using other types of particles, leading to overall performances even worse than the no-coupler case. Therefore, it can be concluded that the performance achieved by an optimized coupler depends not only on the array configuration, but also on the shape of its particles. If the shape of the particle is changed, the optimization must be repeated to obtain the optimal configuration for the desired performance. Considering that the used nanoparticles are very small with respect to wavelength and they are also passive elements, this conclusion may be surprising. Nevertheless, nano-plasmonic interactions often lead to this kind of phenomena, where small-scale details have large impacts on the electromagnetic responses of the structures.

4.4.5 Design of CCs by Using Different Types of Nanoparticles

As discussed in Section 4.4.4, an array configuration provided by the optimization tool is closely related to the types of the nanoparticles used in the designed couplers. Due to their fabrication and well-known enhanced plasmonic properties, most of the couplers in this thesis are designed by using nanocubes. However, it is also possible to design couplers by using nanoparticles with different shapes. In this section, optimization trials for such types of nanoparticles are presented to demonstrate both the effect of particle geometry on the performance of CCs and the efficiency of the optimization tool for different cases. All parameters, such as related to nanowires, excitation, measurement frame, solver, and optimization tool are the same as those presented in Section 4.4.1. Moreover, the number of nanoparticles in the starting layout for the coupler designs is kept fixed.

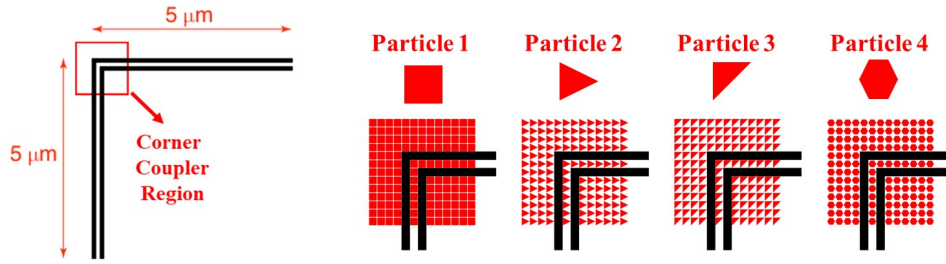


Figure 4.23: Starting layouts for the optimization trials, which are performed for four different types of nanoparticles.

Three different shapes of particles are considered for the coupler designs as illustrated in Figure 4.23 together with the corresponding optimization layouts. Particle 1 in this figure corresponds to the original nanocube with 90 nm edges, whose optimization trials are already presented in Section 4.4.4. Particle 2 and particle 3 are triangular prisms, while particle 4 is a hexagonal prism. As in the CC optimization using nanocubes, optimization trials for different cost functions, i.e., mean and maximum of the power density measured at the sampling points in the output frame are performed, and the configurations obtained after 200 GA generations are accepted as the final designs to compare their performances with respect to each other.

Power density distributions in three different frames corresponding to the optimized couplers with particles 2, 3, and 4 are given in Figure 4.24, in comparison to the results achieved with particle 1. In addition to the plots, the mean and maximum power density values at the sampling points in the measurement frame are also presented. When the results are examined, we observe that, a specific coupler configuration is obtained for each case such that the power transmission is significantly enhanced in comparison to the no-coupler case. This demonstrates the robustness of the optimization tool for different types of nanoparticles. When the results are compared, we observe that the designed couplers involving nanocubes perform much better than the other couplers in terms of both mean and maximum power density values achieved at the outputs. This is consistent with the observation that the leakage of electromagnetic waves at the corner is better suppressed when the coupler involving nanocubes is used. However, the performance of the other couplers can also be considered successful, especially considering the no-coupler case.

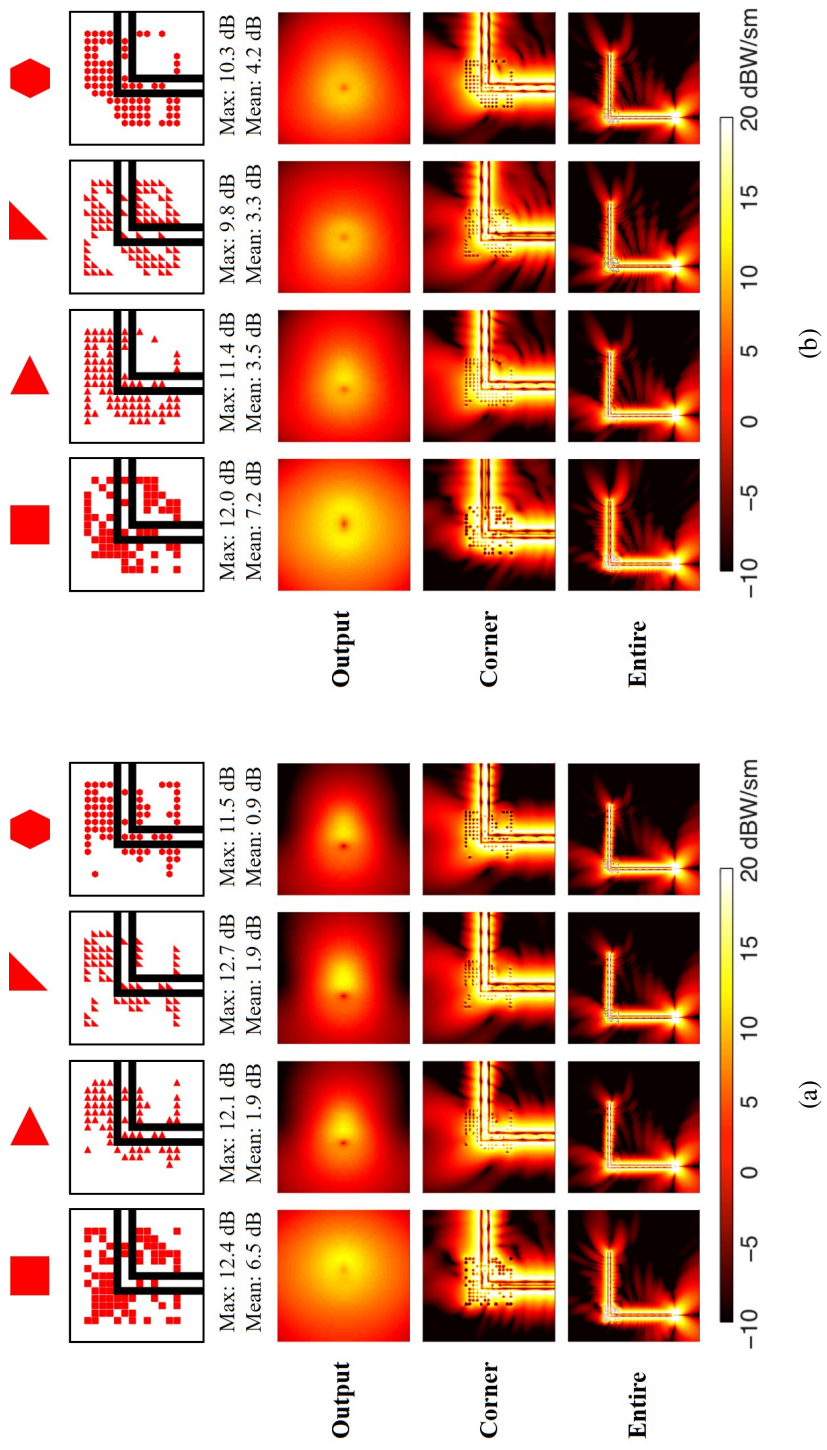


Figure 4.24: Power density distributions for the optimized couplers using different types of nanoparticles, which are designed with the aim of increasing (a) maximum and (b) mean power density in the output frame.

In Figure 4.25, performances of the designed CCs are further tested with respect to frequency from 200 THz to 300 THz. Despite that the couplers are designed at a frequency of 250 THz, their abilities to improve the power transmission along bent nanowires remain in a wide range of frequencies. This plot also shows that, relatively better performances in terms of mean power density is achieved with the coupler involving nanocubes, in comparison to the others. It is also remarkable that the coupler designs with particle 2 and particle 3 (triangular prisms with different cross sections) perform very similar to each other, despite the differences in their geometries and array configurations. This supports the idea that the design of a CC is highly sensitive to the shape of the array elements, while similar performances may still be achieved with the rigorous optimization tool.

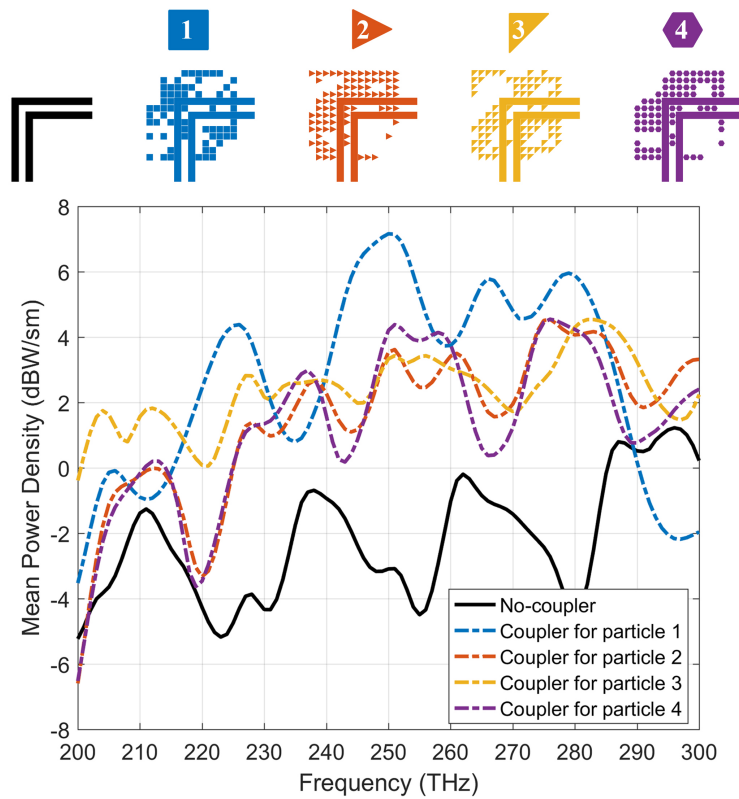
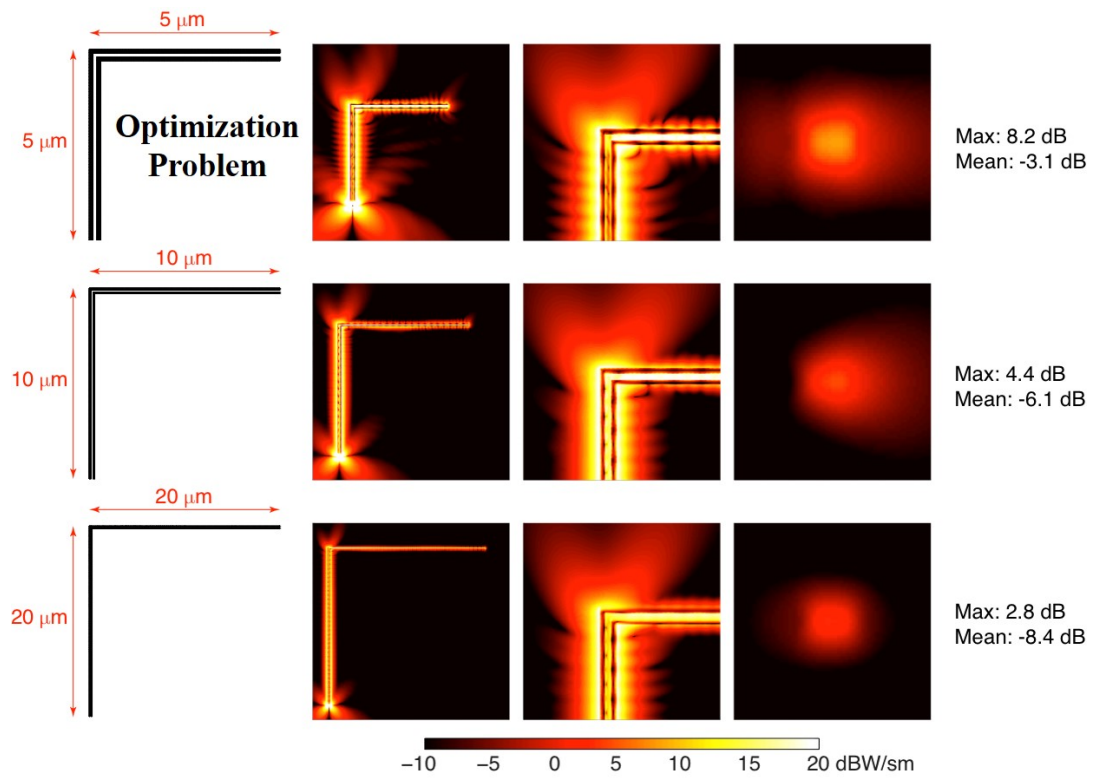
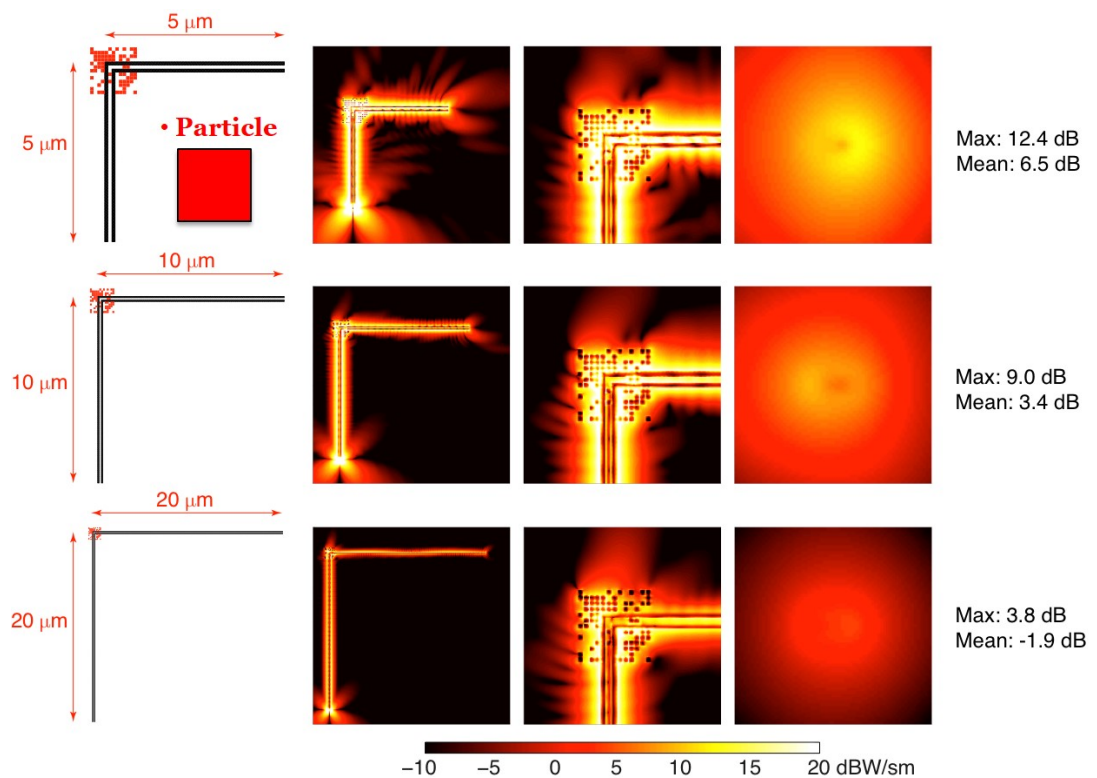


Figure 4.25: Performances of the designed CCs, which involve four different types of nanoparticles to improve the mean power density in the output frame, in a range of frequencies from 200 THz to 300 THz.



(a)



(b)

Figure 4.26: Performance of CC1 with different lengths of nanowires ($5 \mu\text{m}$, $10 \mu\text{m}$, $20 \mu\text{m}$). Power density distributions are shown for the cases (a) without a coupler and (b) with CC1.

4.4.6 Performance of the Optimized CCs for Different Nanowire Lengths

As considered for ICs in Section 4.3.6, CCs may also be desired to be integrated into nanowire systems of different lengths. Considering that CCs are optimized for a pair of 10 μm nanowires with 90° sharp bends, their performances for different lengths are examined in this section.

In Figure 4.26, the results for the integration of CC1 into pairs of nanowires that are longer than the original ones (20 μm and 40 μm) are presented. In Figure 4.26a, the power density distributions for only nanowires (without CC1) are presented in three different frames, while in Figure 4.26b, the results obtained with CC1 are presented. The mean and maximum power density values measured in the output frame are also given for each case. As depicted in the results, CC1 keeps its satisfactory performance for longer nanowires. Specifically, with the integration of CC1, the mean power density is increased by 9.5 dB and 6.5 dB for 20 μm and 40 μm nanowires, respectively. Similarly successful results are also obtained for the values of the maximum power density. The good performance of CC1 is also apparent in the power-density distributions in the corner region. The leakage of electromagnetic energy at the sharp bends can significantly be reduced and the power transmission can significantly be improved by using CC1 for all cases.

The distance between the corner region and the input tips of the nanowires is also an important parameter for the performance of CCs. To investigate this, the length of the first segment of the bent nanowires (before the corner region) is changed progressively from 1.5 μm to 10 μm with a step size of 0.1 μm , while the length of the second segment (after the corner region) is kept constant as 5 μm . For these different lengths of nanowires, the performances of both CC1 and CC2 are examined by comparing the values of the mean power density with those obtained without a coupler. The results presented in Figure 4.27 demonstrate that the optimized couplers can also be used for a wide range of input-to-corner lengths. These results support the ones presented in Section 4.3.6 regarding the performance of an IC for different lengths of nanowires. It can be stated that the array configuration of a coupler mainly depends on the portion of the structure around the coupler region. Therefore, the design of a coupler can be performed for a smaller structure involving the part of nanowire system, where the

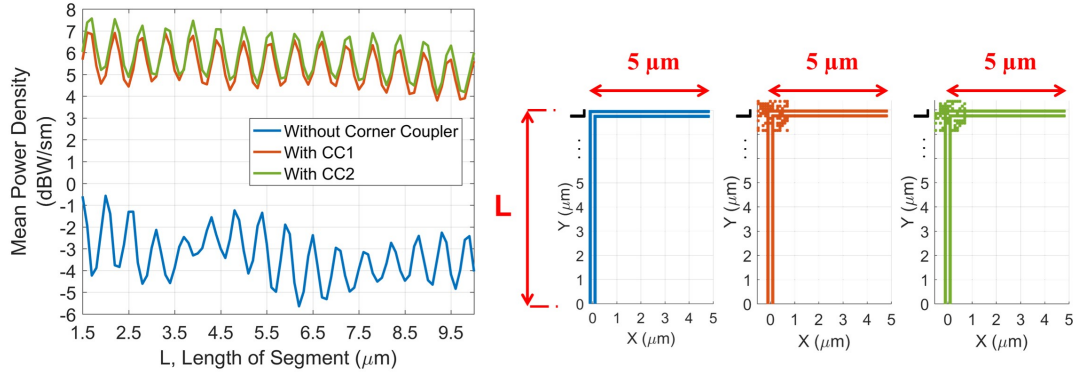


Figure 4.27: Variation of the mean power density in the output frames with respect to the length of the first segment of the bent nanowires for cases without coupler, with CC1, and with CC2.

transmission needs to be improved, e.g., the input tips for the design of an IC and sharp bends for the design of a CC. Once a design is completed, it can be used for different lengths of nanowires with quite satisfactory performances. This way, both the complexity of design processes and the computation load can be reduced. We emphasize that the considered nanowires should still have sufficient lengths (e.g., 5 μm in most of our optimization trials) to avoid contaminations by edge effects.

4.4.7 Performances of CCs in Comparison to Smooth Bends

As mentioned in Section 4.4, smoothing sharp bends, as commonly practiced in the literature, can provide substantial improvements on the transmission abilities of bent nanowires at the expense of geometric inefficiencies and other disadvantages in the context of nanowire networks. CCs presented up to now can be considered as favorable alternatives to such type of operations with their both compact structures and high performances for the efficient transmission of SPPs. At this stage, it is desirable to compare the performances of the designed couplers with the performances achieved by smoothing the sharp bends of nanowires. First, transmission abilities of curved nanowires with different values of radii of curvature (R) are examined. For this analysis, the pair of nanowires in Figure 4.28a, which is used for the optimization of CCs presented up to now, is considered as the reference geometry. Smoothing is applied on these nanowires for different values of R , and the geometries correspond-

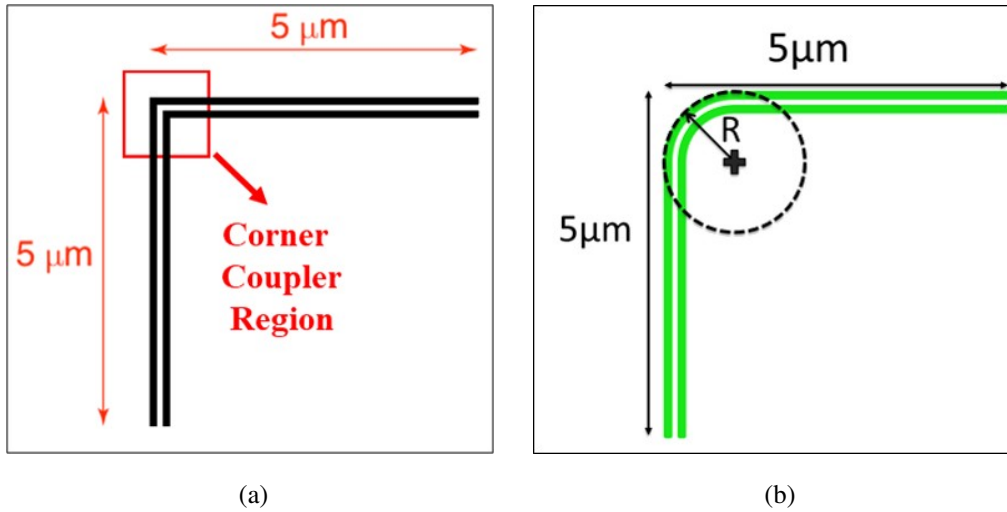


Figure 4.28: (a) A pair of nanowires involving a 90° sharp bend and (b) a pair of nanowires involving a curved bend with a radius of curvature (R).

ing to these different cases are analyzed in terms of the mean and maximum values of the power density in the measurement frame.

Figure 4.29 depicts the mean and maximum power density with respect to R , which is changed from $0.5 \mu\text{m}$ to $5.0 \mu\text{m}$ with a step size of $0.1 \mu\text{m}$. When the results are examined, it can be stated that, despite some local minima, both mean and maximum power density values exhibit increasing trends as the bending radius increases.

To further investigate the transmission abilities of the curved nanowires, the power density distributions in the transversal planes bisecting the geometries and in the output frame are presented in Figure 4.30a and Figure 4.30b, respectively. As can be seen in Figure 4.30a, distortion in the propagation of SPPs occurs in the corner regions especially for smaller values of the bending radius. As the bending radius increases, despite the fact that electromagnetic energy still escapes due to bending, leakage is considerably reduced and the power transmitted to the output is significantly improved, as also illustrated in Figure 4.30b. Besides the enhancement of the power transmission, the symmetry of the pattern in output frame is also improved for large radii of curvatures.

For some certain values of the bending radius (shown with plus and circle in Figure

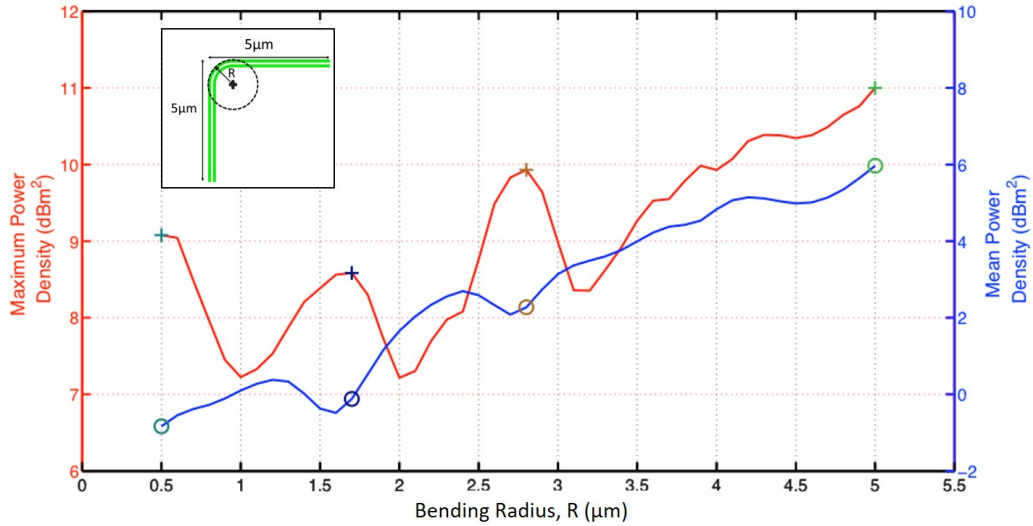
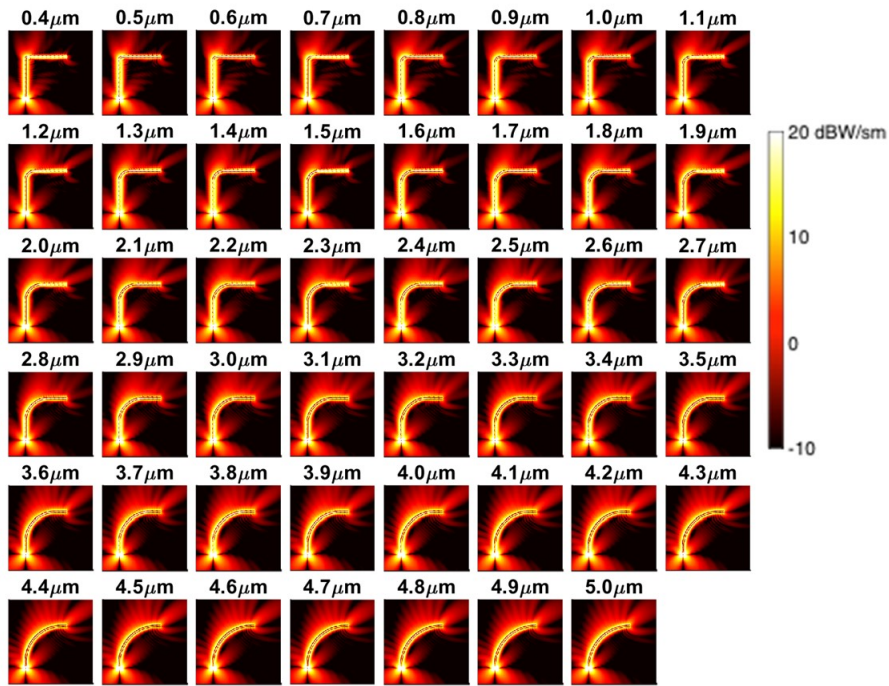
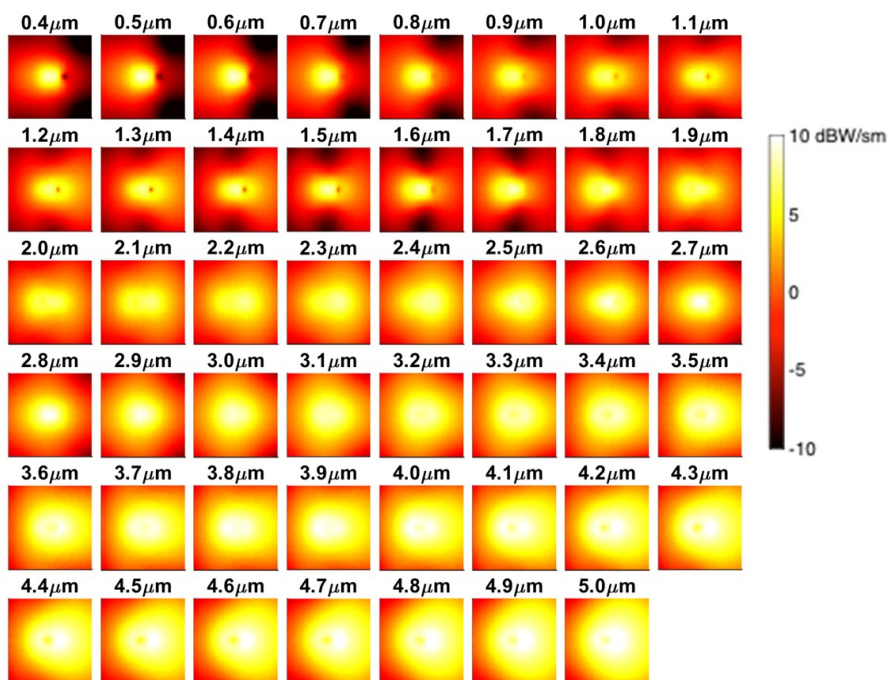


Figure 4.29: Variation of the mean and maximum power density in the output (measurement) frame with respect to the bending radius of curved nanowires.

4.29), i.e., $R = 0.5 \mu\text{m}$, $1.7 \mu\text{m}$, $2.8 \mu\text{m}$, and $5 \mu\text{m}$, the corresponding nanowires and the power density distributions in three different frames are presented in Figure 4.31. The results corresponding to the pair of nanowires involving 90° sharp bend are also given in the first column. The maximum and mean values of the power density computed at the sampling points in the measurement frame are separately given for each case. It is remarkable that, even for small values of bending radius, significant improvements can be obtained in both mean and maximum power density values. For example, once the sharp bends of the nanowires are smoothed with a bending radius of $0.5 \mu\text{m}$, the maximum power density increases from 8.18 dB to 9.08 dB, while much better improvement is obtained for the mean power density that increases from -3.09 dB to -0.83 dB. However, when the performances achieved with the designed couplers are considered, these improvements are outshined. In order to achieve much better transmission ability, a larger bending radius is required. In the smoothing trials, the best performance is achieved when the nanowires are smoothed with a bending radius of $5.0 \mu\text{m}$, as one would expect. Specifically for this extreme case, 9.1 dB and 2.8 dB increases are obtained in the mean and maximum power density values, respectively, in comparison to the values provided by the nanowires involving sharp bends. Despite these satisfactory improvements, nanowires involving smooth bends with this much curvature may be impractical. Specifically, constructing



(a)



(b)

Figure 4.30: Power density distributions for different cases involving curved nanowires with different values of bending radius in a range from $0.4 \mu\text{m}$ to $5.0 \mu\text{m}$: (a) Transversal planes bisecting geometries and (b) the output frame.

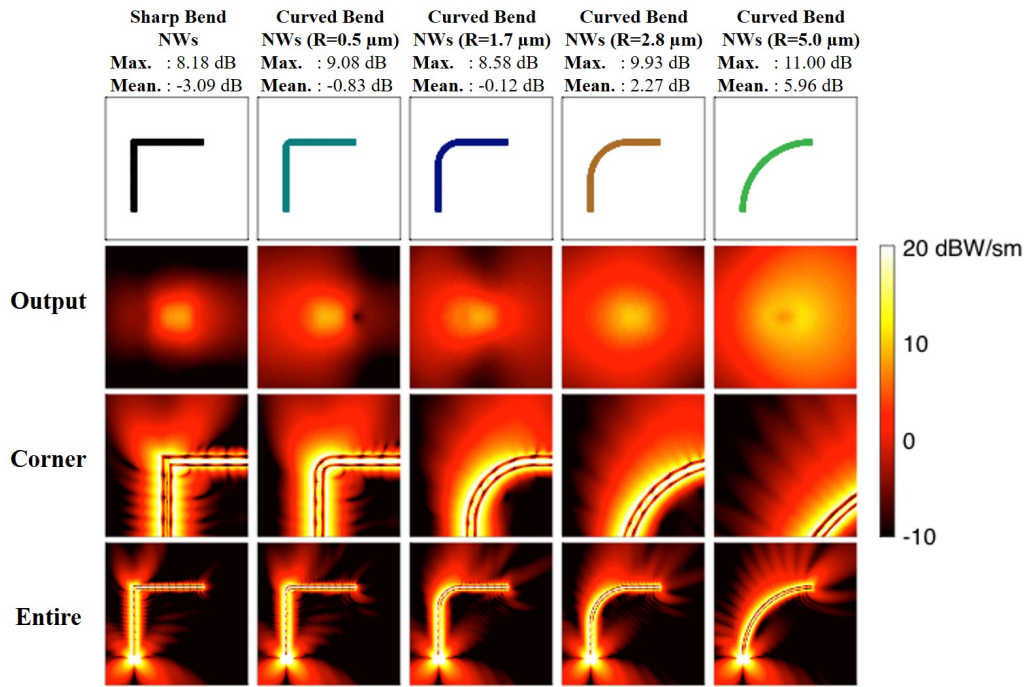


Figure 4.31: Power density distributions in three different frames for curved nanowires with $R=0.5 \mu\text{m}$, $1.7 \mu\text{m}$, $2.8 \mu\text{m}$, and $5.0 \mu\text{m}$ in comparison to the results for nanowires with 90° sharp bends.

large nanowire networks, consisting of several nanowires, couplers, and other types optical devices may not be practical when nanowires are curved with large bending radii. Utilizing compact structures, such as the designed CCs presented in Section 4.4.3, can be much more efficient to construct huge nanowire networks. In fact, in addition to their compactness, the designed CCs provide much better improvements than smoothing. Specifically, by integrating CCs, it is possible to achieve a mean power density of 6.5 dB and a maximum power density of 12.4 dB at the output of the nanowires, while these values are still larger than those achieved with a bending radius of $5.0 \mu\text{m}$.

One may also question the performances of CCs, which are designed for a pair of nanowires with 90° sharp bends, when they are used with curved nanowires. To investigate this, CC1 is integrated into a pair of nanowires, whose bend at the corner is smoothed with a bending radius of $0.4 \mu\text{m}$. Figure 4.32 presents the power density distributions for five different cases. Case 1 (the pair involving a sharp bend without any coupler integration and smoothing operation) and case 2 (the pair involving

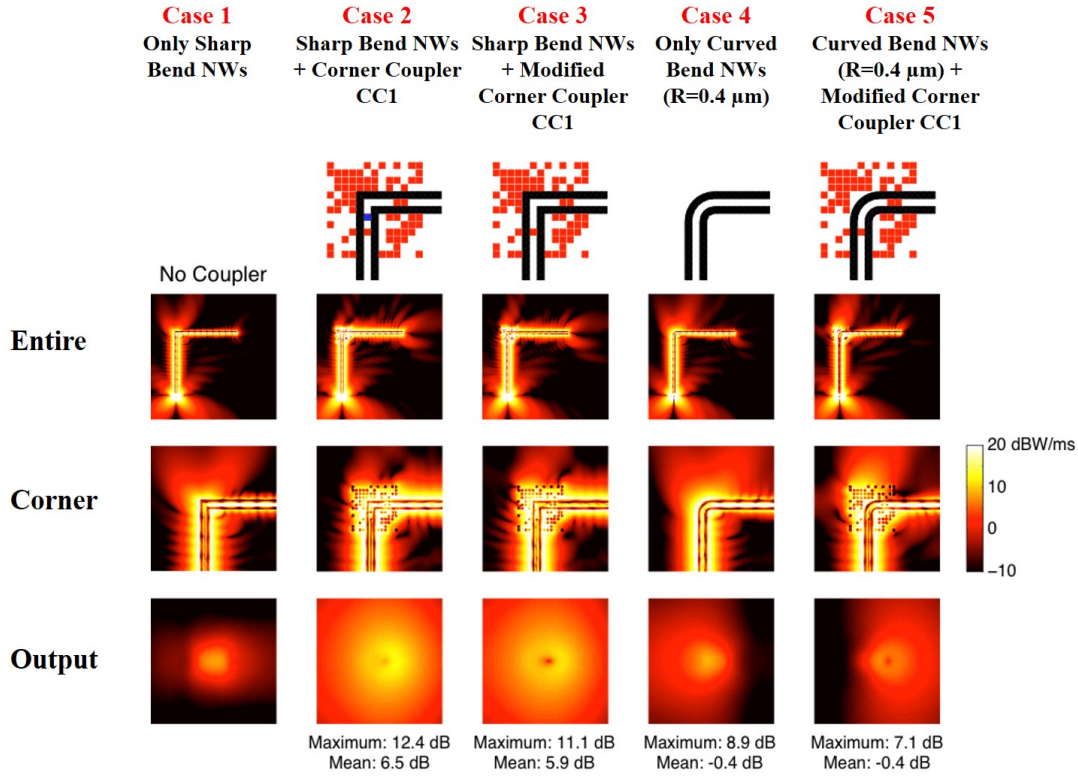


Figure 4.32: Results regarding the integration of CC1 into the pair of curved nanowires with a bending radius of $0.4 \mu\text{m}$.

a sharp bend with the optimized coupler) are given for comparison purposes. To integrate CC1 into the nanowire pair involving curved bend with a radius of $0.4 \mu\text{m}$, one of the nanocubes, shown with blue color in case 2, is required to be removed since it coincides with one of the curved nanowires. Once this nanocube is removed, the value for the mean power density decreases from 6.5 dB to 5.9 dB, while the maximum power density decreases from 12.4 dB to 11.1 dB, as shown in the third column of Figure 4.32. Despite the fact that a significant deterioration occurs in the performance of the CC, it still performs well in comparison to the no-coupler case. However, once the coupler is integrated into the pair of nanowires involving curved bends (case 5), its ability to improve the power transmission is completely destroyed, which can be understood by comparing the results in case 4 and case 5. In fact, the CC deteriorates the propagation of the SPPs over the nanowires. Therefore, it can be concluded that the coupler designs are highly sensitive to the bending of nanowires.

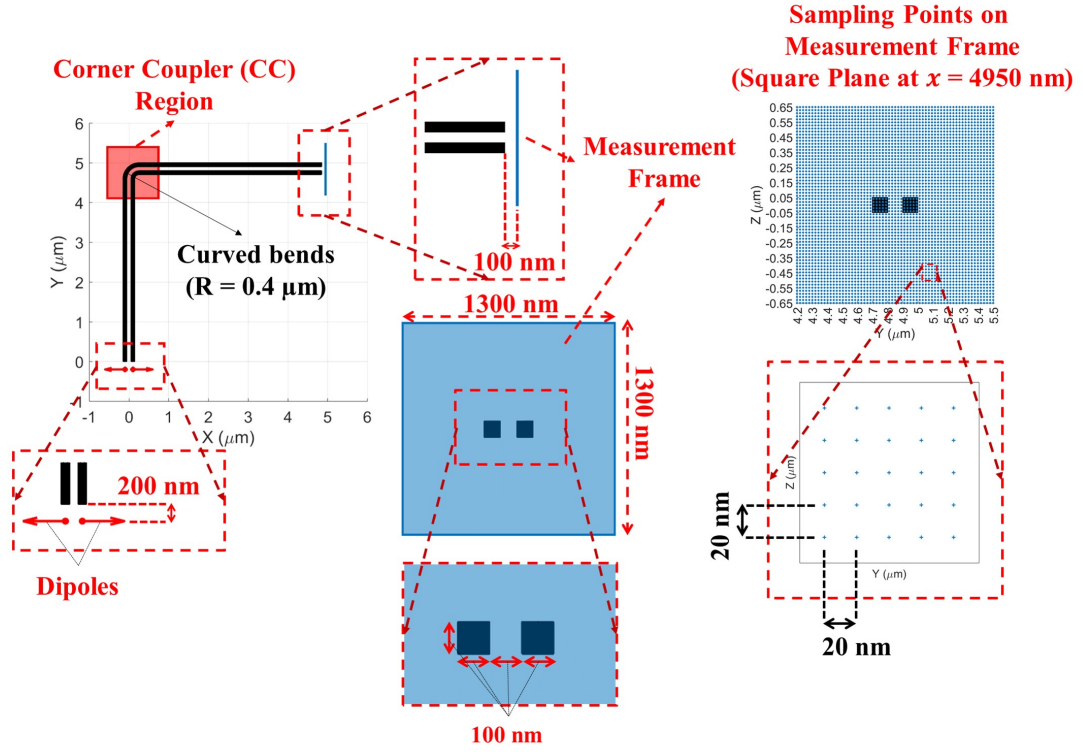


Figure 4.33: Geometric details for the curved nanowires with a bending radius of $0.4 \mu\text{m}$, on which CCs are designed via optimization.

For a given bending, an optimization should be performed to obtain the specific coupler configuration to improve transmission. This idea is supported by performing new optimization trials for a pair of curved nanowires, as illustrated in Figure 4.33. Separate trials are performed for both cost functions, i.e., for the optimization of the mean and maximum power density values in the measurement frame. Power density distributions obtained for the optimized coupler designs are given in Figure 4.34 in comparison to the no-coupler case. Considering the results, it can be stated that the optimization tool can provide suitable array arrangements, i.e., mean and maximum power density values can be enhanced with respect to the no-coupler case. It is also remarkable that the array configurations for the optimized couplers are significantly different than the configurations of CCs designed for the nanowires with sharp bend (CC1 and CC2). However, the values of the power density achieved in the measurement frame are very close to those achieved with CC1 and CC2 on sharp bends. This also demonstrates the efficiency of the optimization tool proposed in Chapter 3 as it provides reliable designs of couplers to achieve satisfactory transmissions with

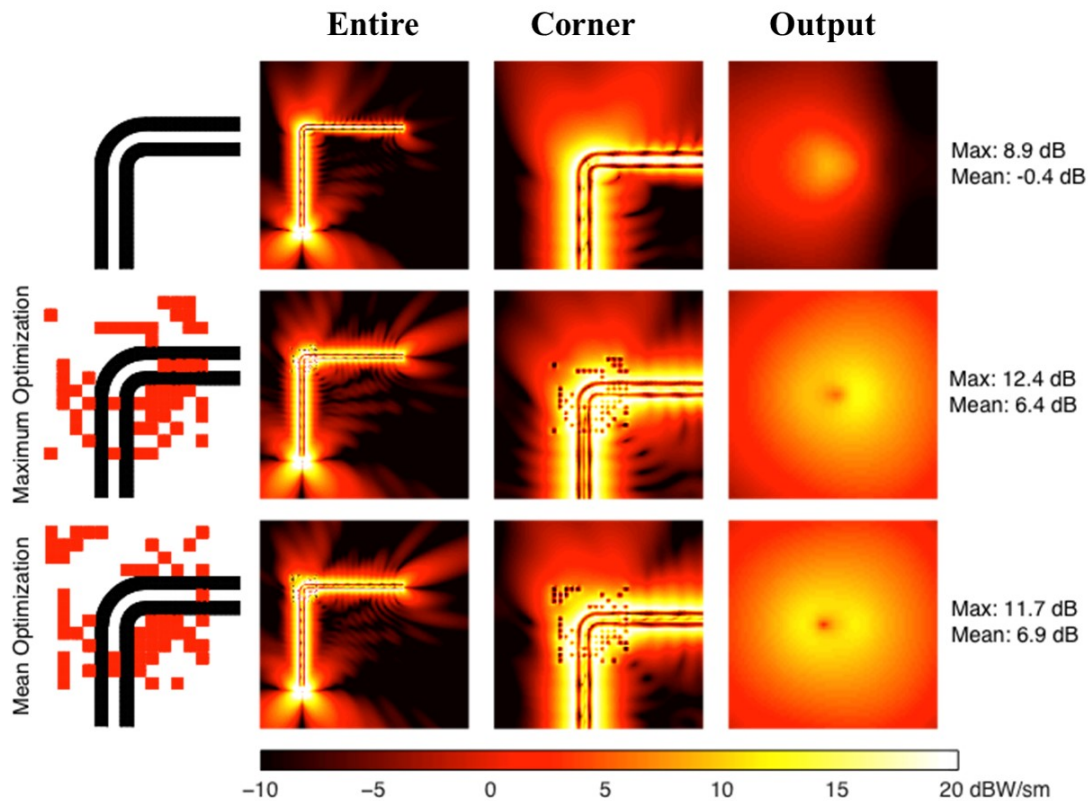


Figure 4.34: Coupler designs with the corresponding power-density results, which are designed for the pair of curved nanowires shown in Figure 4.33.

different types of nanowires.

4.5 Analysis and Optimization of Multiple Couplers

The efficiency of the optimization tool to improve the transmission abilities of different types of nanowire systems is demonstrated with several examples in Sections 4.3 and 4.4. Each of these involves finding an optimal array configuration for a single coupler region. In real-life applications, however, nanowire systems can be more complex with several junctions, bends, and source-input interactions, each of which can be considered as a coupler problem. In order to achieve optimum power levels at the outputs of a nanowire system, efficient and compact couplers should be integrated into such regions, where the flow of the electromagnetic energy is significantly disturbed. One example is given in Figure 4.35, which depicts a pair of bent nanowires

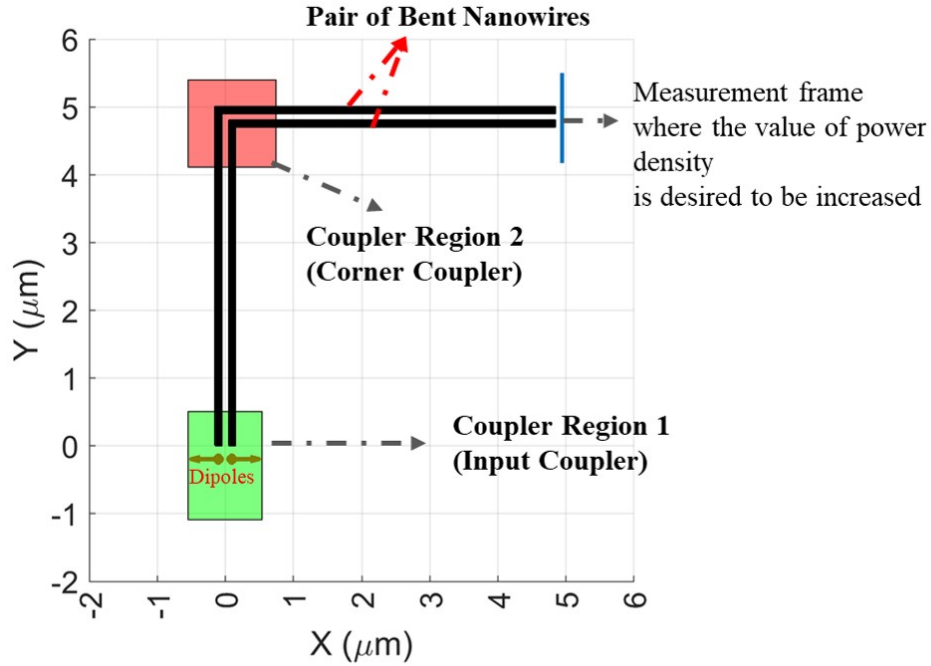


Figure 4.35: A nanowire system involving several coupler regions.

with 90° sharp bends at the center. This nanowire pair is already considered in Section 4.4 for the optimization of CCs (corresponding to the coupler region 2 in Figure 4.35). Despite, the power transmitted to the outputs can significantly be improved by using a CC, the transmission ability of the system is still open to improvements due to the coupling deficiencies in the input region. Specifically, for a better power transmission, well-designed couplers should be used simultaneously in both corner and input regions. There may be different ways to design couplers for such systems involving several coupler regions. A brute-force way is the optimization of the couplers for multiple regions in a single trial of optimization. Although an ideal application of this strategy can provide the ultimate designs for the desired couplers, it can be extremely challenging due to the enlarged optimization spaces. Moreover, since the configurations are achieved for very specific cases where multiple coupler regions coexist, the obtained designs for the couplers can be very specialized and not suitable to be employed for general purposes. On the other side, in Section 4.4.7, it is shown that the performance of a coupler is mainly sensitive to the local region where the coupler is placed. Considering this, the couplers for different regions can be designed separately, e.g., ICs can be designed by considering straight nanowires and CCs can

be designed by considering a relatively small portion of bent nanowires. Once the designs are completed, they can be used together to construct complex nanowire structures. In this section, this idea is tested in detail and the validation of the approach is demonstrated via several examples involving extensive analysis and optimization trials.

4.5.1 Compatibility of Separately Designed Couplers

We now consider the use of multiple couplers, which are designed separately, on a single nanowire structure. As shown in Section 4.4, CC1 and CC2 provide significant improvements in power transmission through bent nanowires by eliminating the leakage of electromagnetic waves. Similarly, in Section 4.3.4, IC1 and IC2 are introduced to improve power transmission along straight nanowires. In the following, we test the performances of the ICs for bent nanowires, as well as their compatibility with the CCs. Coupler configurations used for these analyses are as shown in Figure 4.36. In Figure 4.37, the power density distributions obtained for different cases involving different combinations of ICs and CCs on a pair of nanowires with 90° sharp bends are presented. The results obtained when none of the couplers is used (empty + empty) are also given for comparisons. In addition to the power density distributions, the geometry corresponding to each case is also illustrated, where the couplers are shown as colored rectangular frames (red for CC and green for IC). The results show that the best transmission to the output of the nanowires can be achieved when an IC and a CC are used together. First, it is remarkable that ICs designed for straight nanowires also perform well for bent nanowires. Specifically, even only using an IC at the input provides a significant increase in the power density values at the output. For example, with the integration of IC1, the mean power density increases from -3.1 dBW/m² to 17.3 dBW/m², which corresponds to an increase by 20.4 dB. Similarly successful results are obtained with the integration of IC2, which increases the mean power density by nearly 19.6 dB with respect to the no-coupler case. However, without using a CC, significant amounts of power escape in the bending region. Once a CC is integrated into the corner region, power loss due to bending is dramatically reduced and the power transmitted to the output frame is further increased. The progressive improvement in power transmission can be seen by comparing dif-

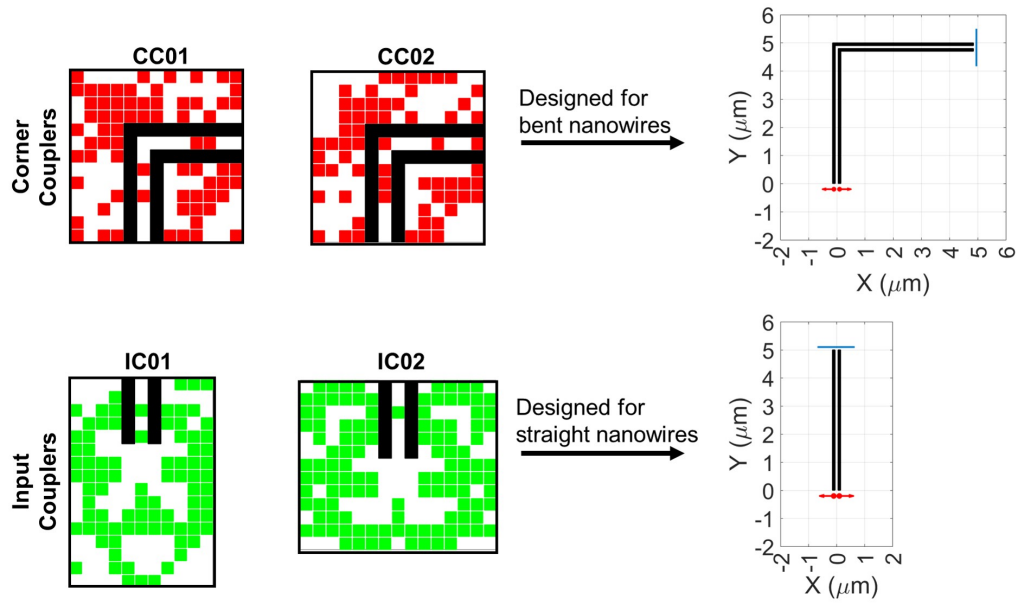


Figure 4.36: IC and CC designs used in the tests presented in Figure 4.37.

ferent cases in Figure 4.37. For example, when none of the couplers is used (empty + empty), the mean power density is -3.1 dBW/m^2 in the output frame. If the power losses at the input are eliminated by using IC1, the mean power density increases to 17.3 dBW/m^2 . In addition to IC1, once CC1 is also integrated into the corner region, the mean power density further increases from 17.3 dBW/m^2 to 24.2 dBW/m^2 . Similarly successful results are also observed for different combinations of IC1 and IC2 with CC1 and CC2. These results obviously demonstrate that the transmission ability of a nanowire system can be improved by using multiple couplers together. In addition, couplers designed for sub-systems can perform well in larger systems. For example, ICs designed for straight nanowires can provide high performance for other types of nanowire systems, such as bent nanowires. However, to validate the sub-system approach, the performances of the designed ICs should also be compared with those that are designed by using bent nanowires. This issue is examined in the next section.

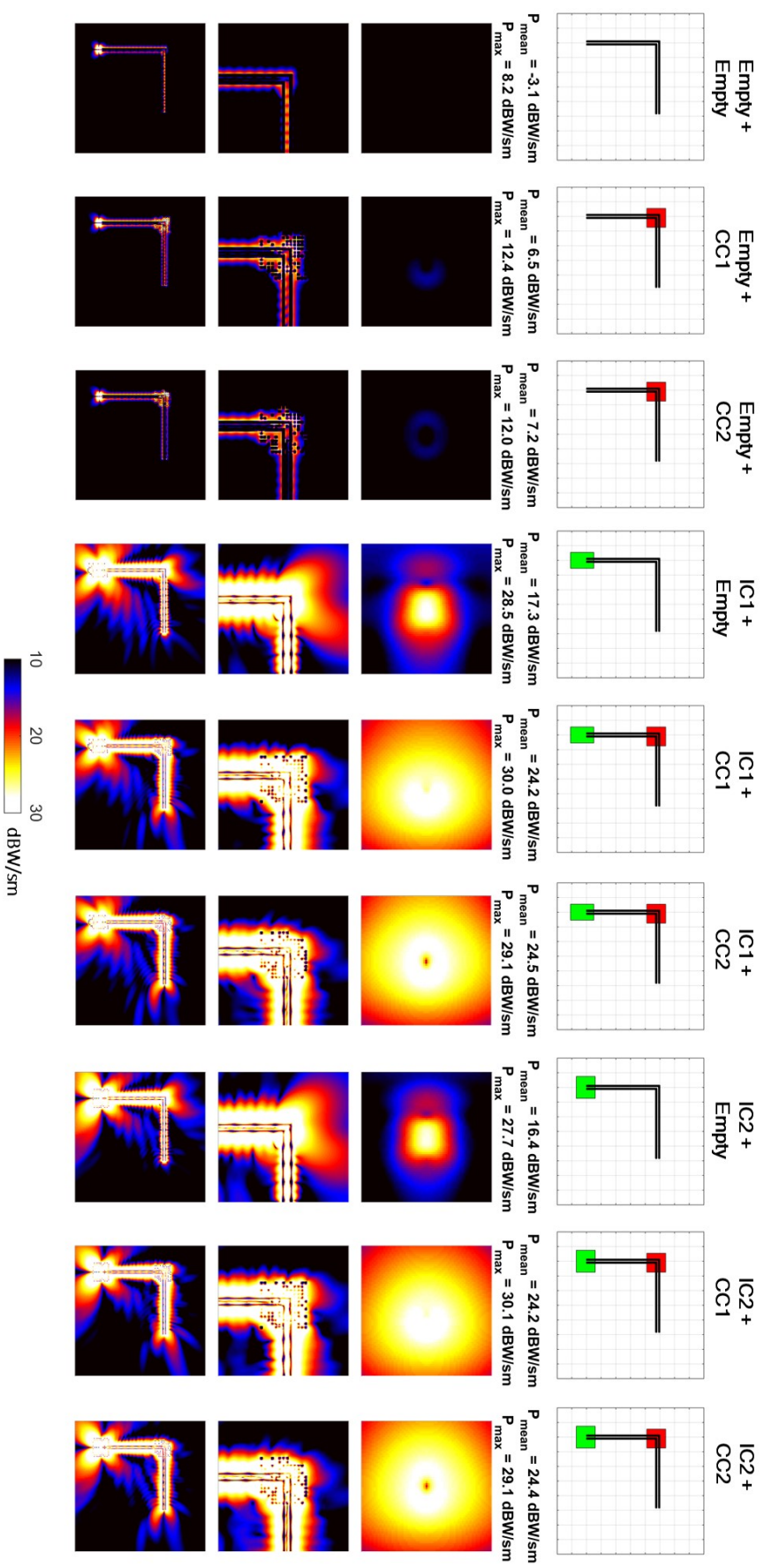


Figure 4.37: Power density distributions for different cases corresponding to different combinations of ICs and CCs into the coupler regions of the bent nanowires shown in Figure 4.35.

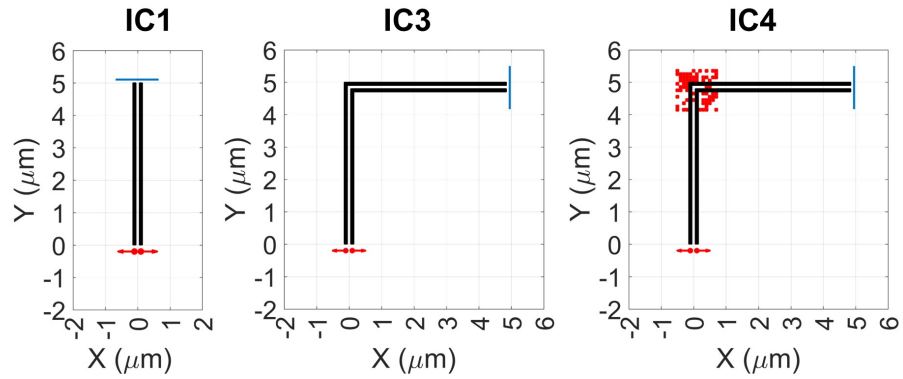


Figure 4.38: The nanowire geometries used for the optimization of different types of ICs, i.e., IC1, IC3, and IC4.

4.5.2 Optimization of ICs for the Bent Nanowires

The high performances of the ICs designed for a pair of 5 μm straight nanowires, e.g., IC1 and IC2 (Figure 4.11), are demonstrated for the transmission abilities of bent nanowires in Section 4.5.1. This section involves the optimization of new ICs specifically for bent nanowires. For this purpose, optimization trials for two more cases are considered, as depicted in Figure 4.38. In the first case, the optimum configuration of IC is searched to enhance the transmission ability of a pair of bent nanowires (the nanowire geometry is the same as the one used for the optimization of CCs, i.e., see Figure 4.15). The final design of IC for this case is called IC3. In the second case, an IC is designed for the same bent nanowires when it is used together with CC1, and the final configuration is called IC4. It should be noted that CC1 is designed for the bent nanowires without considering any IC, and the corresponding results are already given in Section 4.4. The nanowire geometries utilized during the optimization of IC1, IC3, and IC4 are illustrated in Figure 4.38. All parameters related to the optimization are selected as in the design of IC1, whose details are given in Section 4.3. Moreover, both IC3 and IC4 are designed based on the layout of 157 nanocubes, which is the same as the layout of IC1.

In Figure 4.39, the designs of IC1, IC3, and IC4, as well as the corresponding optimization histories in comparison to different power levels are shown. Considering

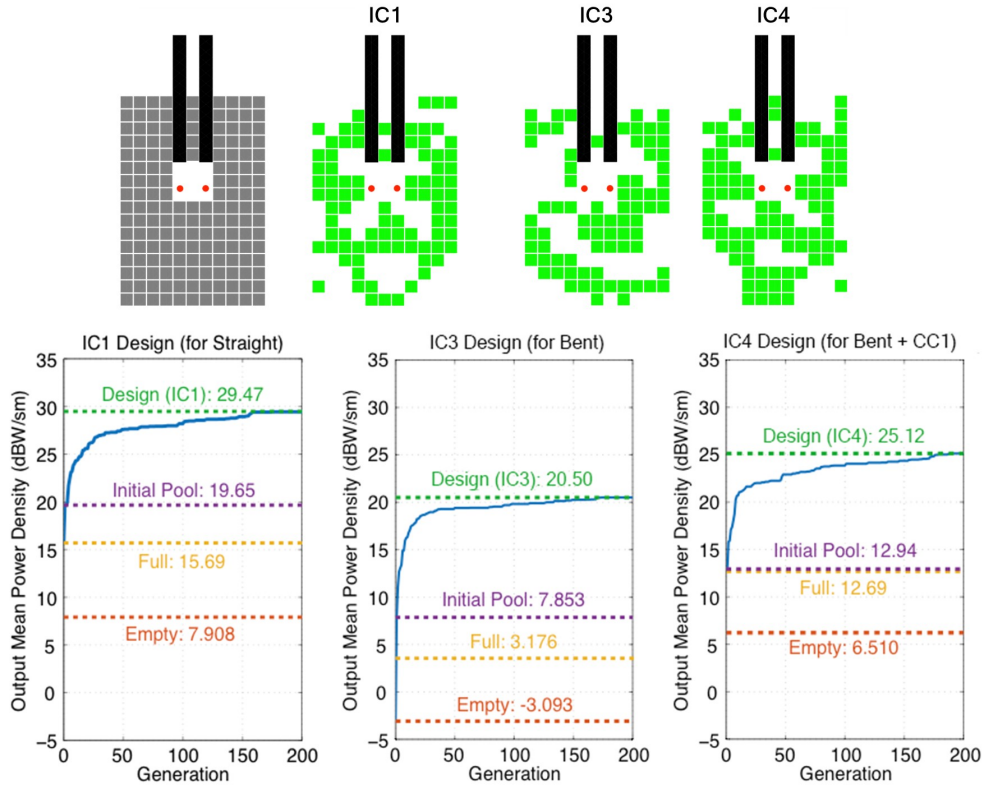


Figure 4.39: Couplers IC1, IC2, and IC3 that are designed for different scenarios. Optimization histories are shown with different levels (empty, full, and the best configuration in the initial pool).

the fitness values (output mean power density) with respect to generations, both trials of optimization (IC3 and IC4) can be said to achieve significant improvements in the power transmission. Specifically, with the design of IC3 corresponding to the optimization of an IC for $5 + 5 \mu\text{m}$ bent nanowires, the mean power density in the output frame increases to 20.50 dBW/m^2 , in comparison to -3.039 dBW/m^2 (without any IC) and 3.176 dBW/m^2 (when the full layout is used directly). Similarly, IC4 provides a significant improvement in the power transmitted to the output, leading to 25.12 dBW/m^2 mean power density, while this value is only 6.510 dBW/m^2 without its integration (when there is only CC1).

In Figure 4.40, the power density results for ten different cases involving bent nanowires are presented. Each case corresponds to the integration of different combinations of IC1, IC3, IC4, and CC1 into the coupler regions. The results for the cases when none of the couplers is utilized (empty + empty) and when using full arrays corresponding

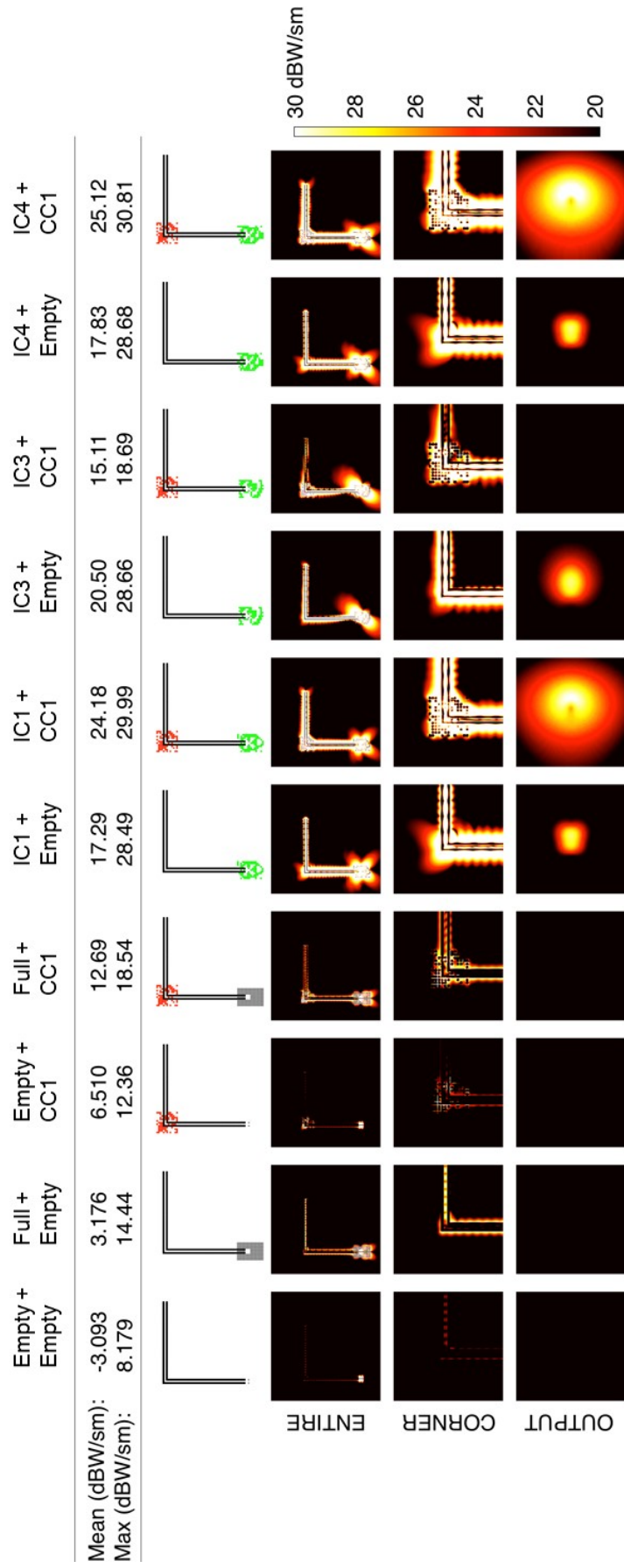


Figure 4.40: Power density results for the different cases involving different combinations of IC1, IC3, IC4, and CC1 into the system of bent nanowires.

to the layouts of IC1, IC3, and IC4 are also given for comparisons. Among different cases, the best level of power transmission to the output is achieved when using IC4 together with CC1, i.e., a mean power density of 25.12 dBW/m² is obtained in the measurement frame. In fact, this level of performance is somewhat expected, since IC4 is particularly designed for bent nanowires integrated with CC1. A remarkable result is that, although IC1 is designed for a pair of 5 μm straight nanowires, its use for the bent nanowires involving CC1 at the corner region provides excellent power transmission, even comparable to that provided by IC4 and CC1 together. Specifically, a mean power density of 24.18 dBW/m² is obtained at the output when using IC1 + CC1. On the other hand, IC3 that is optimized for the bent nanowires without any CC provides a relatively poor performance in comparison to IC1 and IC4. Although, its integration with the bent nanowires leads to an increase in the mean power density by approximately 23.50 dBW/m² with respect to the no-coupler case, its performance significantly deteriorates when CC1 is further integrated into the corner region, since IC3 is optimized specifically for the bent nanowires without any CC. This is mainly due to the fact that the transmission ability of a bent nanowire is significantly affected by bending losses unless any CC is used. Therefore, the optimization tool provides a highly special array configuration for IC3 such that the dipole pattern at the input is steered towards the output of the nanowires, and the electromagnetic energy is forced to propagate through the host medium rather than being guided along the nanowires. Obviously, this is not a desired solution for the practical applications.

The operation mechanisms of IC3 and IC4 can further be investigated by examining their performances with straight nanowires. The results for power density distributions are presented in Figure 4.41, in comparison to IC1 that is particularly optimized for straight nanowires. All couplers lead to much better transmission levels than the no-coupler and full-array cases. However, IC3 again provides relatively poor power transmission in comparison to IC1 and IC4, since it is optimized for bent nanowires without any CC. It is remarkable that, IC4, which is optimized for bent nanowires when CC1 exists at the corner, performs well for straight nanowires. Specifically, the use of IC4 with the 5 μm straight nanowires, the mean of the power density reaches 29.09 dBW/m² at the output, while this value is equal to 29.47 dBW/m² when IC1 is used. In fact, this implicitly demonstrates the effectiveness of CC1. Using CC1 in

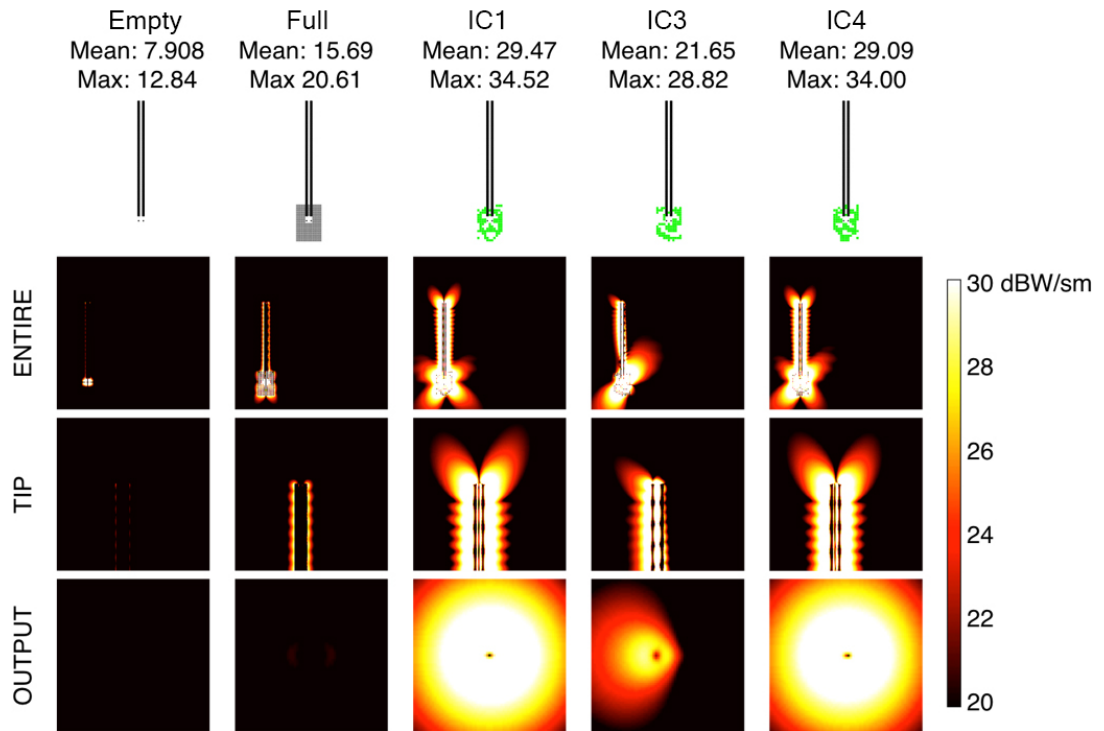


Figure 4.41: Power density distributions for the cases when IC1, IC3, and IC4 are integrated into the input region of the $5 \mu\text{m}$ straight nanowires.

the bending region can reduce the reflections from the corner so effectively that the performance of IC4 is weakly affected by the bends.

Considering all of these results discussed above, several main conclusions can be reached related to the optimization of ICs and CCs. First, for a proper optimization of an IC to be used in complex nanowire structures, including sharply bent nanowires, secondary deficiencies on the electromagnetic energy flow, such as reflections and diffractions at bending regions, should be eliminated to avoid misleading results. This rule can be generalized to other types of couplers, i.e., in an optimization of a coupler, the isolated sub-system should be constructed on the assumption that other sub-systems operate properly. Second, different types of couplers, such as CCs and ICs can work together efficiently to improve transmission abilities of nanowires, although they are optimized in separate optimization trials. Nevertheless, it is always possible to optimize different types of couplers in a single trial of optimization, and this issue is examined in the next section.

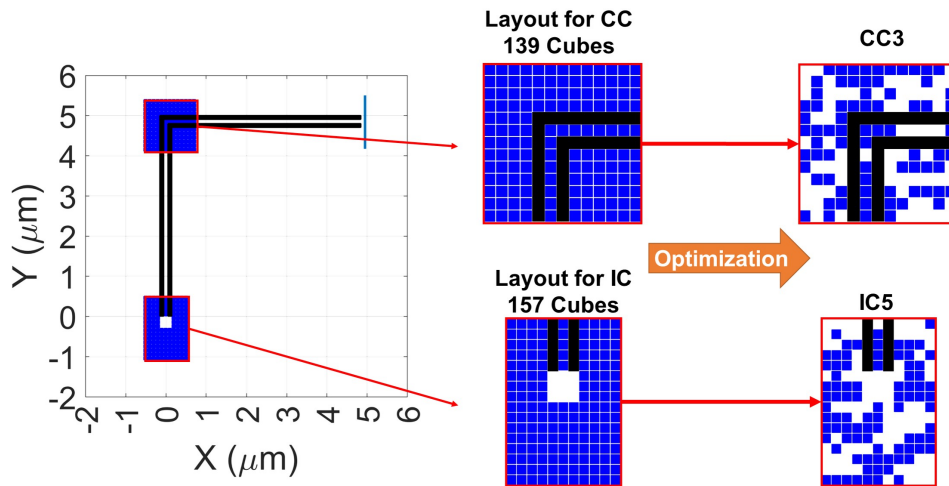


Figure 4.42: Layouts and ultimate configurations for IC5 and CC3 when they are designed simultaneously.

4.5.3 Design of Input and Corner Couplers via a Simultaneous Optimization

In Section 4.5.2, it is shown that power transmitted to outputs of bent nanowires can also be improved with a proper design of an IC, in addition to the use of a CC in the bending region. Moreover, an IC can be designed either specifically for bent nanowires involving a CC or directly for straight nanowires. In both approaches, highly successful transmission abilities can be achieved for bent nanowires. In fact, these approaches can be better than performing a simultaneous design of couplers, considering the dramatic grow of the optimization space with the number of bits. To provide comparative results, an additional trial of optimization is carried out to design a pair of IC and CC simultaneously for bent nanowires using the layouts of 157 and 139 nanocubes, respectively. It should be noted that all parameters regarding the optimization of these couplers are the same as those used in the earlier optimization trials. Moreover, the layout of IC1 is selected as the layout of the designed IC, while the layout of CC1 is used for the optimization of the CC.

In Figure 4.42, the initial layouts for the designed couplers and the final configurations (IC5 + CC3) obtained by the optimization are given. In Figure 4.43, the power density distribution when IC5 and CC3 are used with the bent nanowires ($5 \mu\text{m} + 5 \mu\text{m}$) is given in comparison to several cases including (IC1 + CC1) and (IC4 + CC1). The

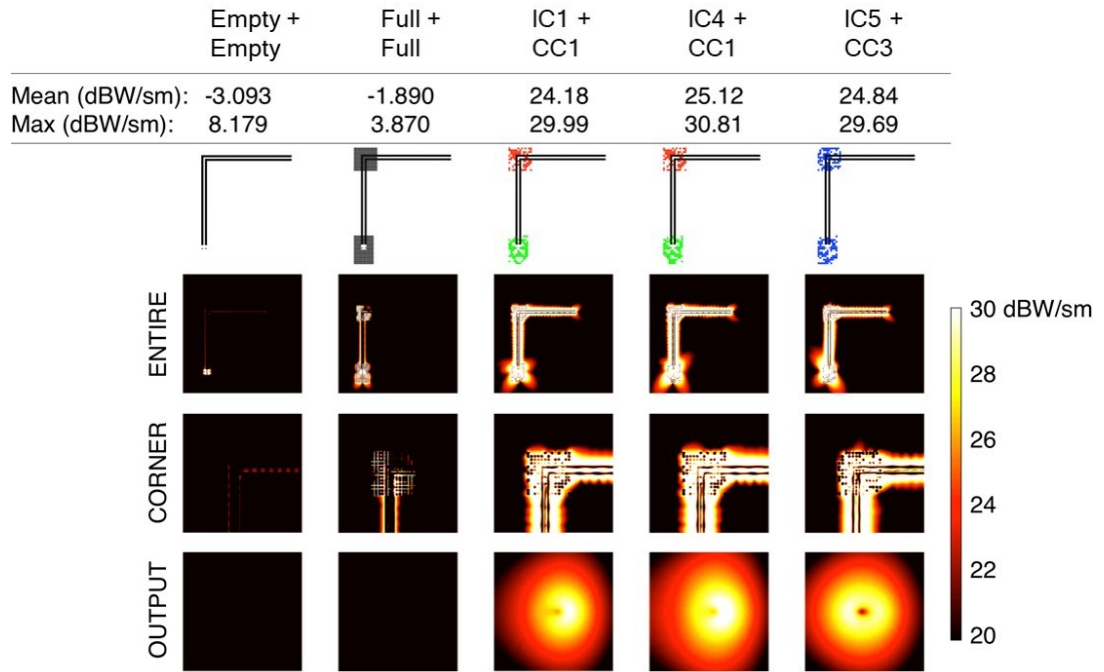


Figure 4.43: Power density distributions for several cases involving different configurations of ICs and CCs.

design (IC5 + CC3) is successful with 24.84 dBW/m^2 mean power density at the output, while this is not better than IC3 together with CC1. In fact, even IC1 with CC1 performs similarly. Obviously, if the optimization result was a global maximum, IC5 + CC3 is expected to be better than any other manual combinations. But, the results in Figure 4.43 clearly show that the improvement would not be significant to justify the cost of the increased computational load due to the enlarged optimization space.

To give an idea about the computational load of the optimization trials, the average time for the completion of one generation and the total time required to carry out 200 generations of an optimization are given in Table 4.4 for different cases of IC and CC optimization. All optimization trials given in Table 4.4 are carried out in the MATLAB environment (2.5 GHz Intel Xeon E5-2680v3 processors), while the processing times are for a single core. As listed in the table, the simultaneous optimization of IC and CC to reach IC5 + CC3 is the worst case in terms of the CPU time. Specifically, achieving a mean power density of 24.84 dBW/m^2 at the output of the bent nanowires by designing IC5 and CC3 takes 301 days on a single core. On the other hand, optimization of IC1 and CC1 in separate trials require a total time of 214.7 days (90

Table 4.4: Computational Load For the Optimization of ICs and CCs in Different Scenarios

Optimization Problem	Number of Unknowns	Average Time Per Generation (Hours)	Total Optimization Time (Days)
IC1	11514	10.8	90
IC3	12870	12.4	103.3
IC4	16650	20.96	174.7
IC5 + CC3	20376	36.12	301.0
CC1	11898	14.96	124.7

days for IC1 + 124.7 days for CC1), while their integration into the bent nanowires provides a mean power density of 24.18 dBW/m². Moreover, once these couplers are designed separately, they can also be used in other types of complex nanowire networks rather than being efficient for a particular case. Considering the cost of the increased computational load due to the enlarged optimization problem, dividing a problem with multiple coupler regions into multiple sub-problems is a more efficient and feasible approach. Performances of separately optimized couplers within complex nanowire networks are demonstrated in Section 4.7.

4.6 Design of Efficient Couplers for Different Types of Junction Problems

In Section 4.3 and Section 4.4, nanowire segments with single outputs are considered together with various coupler designs. On the other hand, in many practical applications, such as plasmonic integrated circuits [16], once propagating waves are generated along nanowires, they may be desired to be transmitted in several branches towards multiple outputs in order to excite other devices. Such types of nanowire networks involve different kinds of junctions to transmit electromagnetic power to the desired outputs. Considering successful results for straight and bent nanowires, couplers that consist of proper arrangements of nanoparticles can also be designed to enhance power transmission through such junctions. In this section, optimization

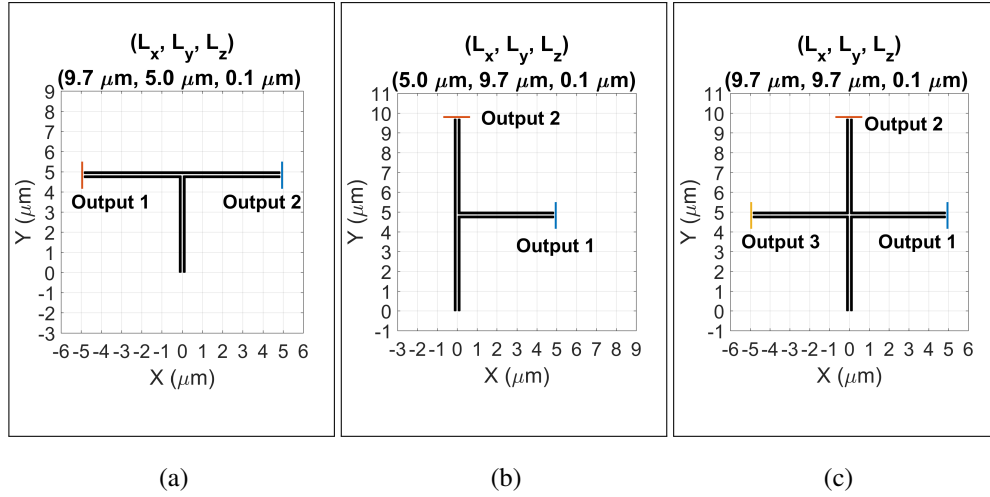


Figure 4.44: Three different types of junctions involving $5 \mu\text{m}$ nanowire segments: (a) Three-way junction with two symmetrically located outputs, (b) three-way junction with two differently oriented outputs, and (c) four-way junction with three outputs (dimensions of the geometries are also given).

of couplers for three different types of junctions shown in Figure 4.44 are presented with detailed analyses of their performances.

4.6.1 Details Related to the Optimization of Junction Couplers

As the sample junction problems, three different types of nanowire systems shown in Figure 4.44 are considered. Proper arrangements of nanoparticle arrays are searched for each junction by performing different on-off optimization trials using nanowire segments representing the corresponding junction. The optimization trials presented in this section are carried out by using the optimization tool proposed in Chapter 3 with the optimization parameters given in Table 4.3, while the full-wave solutions are performed by using the MLFMA solver introduced in Chapter 2 with the solver parameters listed in Table 4.2. To construct the nanowire systems, pairs of closely placed nanowires are considered, as in the design of CCs and ICs. The parameters related to the nanowires and the excitation, such as the cross section of the nanowires, the distance between the nanowires, and the distance between the dipoles and nanowires are selected as given in Section 4.2. The operation frequency is again fixed to 250

THz, while $90 \times 90 \times 90$ nm Ag nanocubes (whose good performances to build couplers are already demonstrated) are used to design the junction couplers. As in the designs of ICs and CCs, each coupler is designed by initially considering the corresponding full array, i.e., when all nanocubes exist on a predetermined grid with 100 nm center-to-center distances between consecutive elements. The performances of junction couplers are investigated by examining the power density values in the measurement frames. The parameters related to the measurement frame, such as its dimensions and sampling points are as given in Section 4.2.

The optimization trials for junctions are carried out to improve the power density obtained at the outputs while minimizing the difference between them. This can be achieved either automatically by using symmetrical configurations for the designed coupler, such as depicted in Figure 4.44a, or choosing a well-designed cost function. The cost function used in the optimization trials shown below can be defined as

$$CF3 = CF1 \times CF2, \quad (4.3)$$

where CF1 is the term that measures how much power is transmitted to all outputs in average and CF2 is the term that measures the balance between the power transmitted to different outputs. Given that M represents the number of outputs and $MPD^{Output,k}$ is the mean power density at the k th output that is defined as

$$MPD^{Output,k} = \frac{\sum_{i=1}^N \sqrt{|S_x(x_i, y_i, z_i)|^2 + |S_y(x_i, y_i, z_i)|^2 + |S_z(x_i, y_i, z_i)|^2}}{N}, \quad (4.4)$$

where S_x, S_y, S_z are the components of the Poynting vector (\mathbf{S}) in x, y, z directions, respectively, CF1 and CF2 can be defined as

$$CF1 = \frac{\sum_{k=1}^M MPD^{Output,k}}{M}, \quad (4.5)$$

and

$$CF2 = \frac{1}{2^{std(MPD^{Output,1}, MPD^{Output,2}, \dots, MPD^{Output,M})}}, \quad (4.6)$$

respectively. In the above, "std" represents the standard deviation. By using the cost function defined in Equation 4.3, the optimization tool provides suitable array configurations such that the mean power density at the outputs can be maximized while the difference between them is minimized. In this cost function, term CF2 can

be considered as a punishment factor, i.e., any imbalance in the power transmitted to the outputs leads to an CF2 value less than 1. Hence, the overall fitness value (value of CF3) is decreased by the multiplication of CF2. Moreover, as the imbalance, and accordingly, the standard deviation between the mean power density values obtained in the output frames increase, CF2 exponentially decreases, leading to significantly reduced fitness values. Hence, individuals with higher differences between mean power density values at the outputs are more likely eliminated during an optimization, and a successful design provides an CF2 value close to one corresponding to well-balanced output powers.

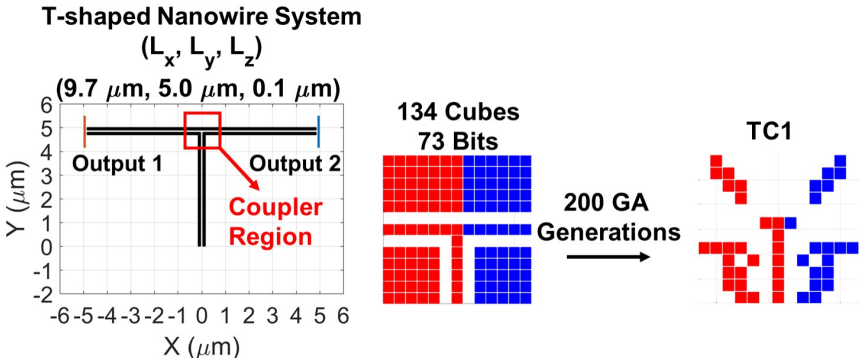


Figure 4.45: T-shaped nanowire system involving a three-way junction with two symmetrically located outputs. Full array layout used for the optimization of the junction coupler and the final design (TC1) are also shown.

4.6.2 Design of Couplers for a Three-way Junction with Two Symmetrically Located Outputs

In this section, coupler designs for the nanowire system involving a three-way junction with two symmetrically located outputs are considered. As shown in Figure 4.45, the structure consists of three $5 \mu\text{m}$ segments, one of which is used as the input leg for the excitation, while the others are used as the outputs. Ideally, such type of a nanowire system can be utilized to deliver electromagnetic power from one input to two symmetrically located outputs. Considering that the junction involves 90° sharp bends to connect the input to the outputs, electromagnetic energy flow through the nanowires can significantly be distorted due to reflections and diffractions at the

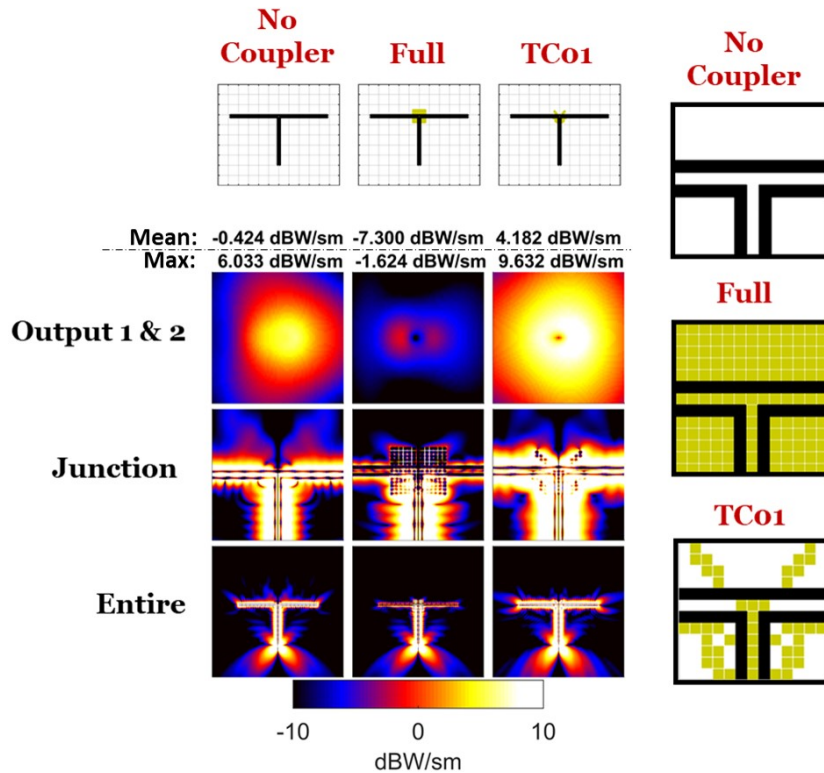


Figure 4.46: Performance of TC1 in comparison to the no-coupler and full-array cases. Power density distributions in three different frames and the geometries for all cases are shown.

junction. The optimization trial is performed to design a coupler, namely T-shaped junction coupler (TC), involving arrangements of nanoparticles such that the power transmitted to the outputs can be increased equally. As depicted in Figure 4.45, the starting layout for the coupler designs involves 134 particles, which are the remaining elements of an 13×13 array once the particles that coincide with the nanowires are removed. Since the outputs are symmetrically located, symmetry is enforced during the optimization for the arrangement of the nanoparticles, i.e., existences of particles are only searched for half of the full array (73 particles). After 200 generations of an optimization trial, the coupler design, namely TC1, is obtained, as shown in Figure 4.45.

To investigate the design, the power density distributions for the case involving the nanowire system without a coupler, as well as for two cases corresponding to the integration of the full array and the optimized array into the junction region are presented

in Figure 4.46. The results, once again, demonstrate the efficiency of the coupler for the nanowire network. When the results corresponding to the no-coupler case are examined, it can be observed that a significant amount of electromagnetic power propagating along the nanowires escapes into the host medium from the junction, which significantly deteriorates the transmission towards the upper nanowire segments and the outputs. In fact, this is as expected behavior, since the plasmonic waves that are generated at the input tips of the nanowires mostly propagate along the longitudinal axis of the input nanowire segment. Once the waves arrive at the junction, they tend to keep their initial propagation direction so that a significant amount of power is coupled to vacuum and propagates away. With the integration of the properly designed junction coupler TC1, waves arriving at the junction interact with the particles such that they are directed towards the outputs of the nanowire system. This can be observed by comparing the amplitudes of the power density along the nanowires before and after the junction regions. High-quality performance of the designed coupler can also be supported with quantitative data. Specifically, the mean power density at the outputs increases to 4.182 dBW/m^2 , while these values are equal to -0.424 dBW/m^2 and -7.30 dBW/m^2 for the no-coupler and full-array cases, respectively.

In Figure 4.47, the performance TC1 is further illustrated when it is utilized together with IC1 and IC2. As in the case of CCs, ICs significantly improve the power levels at the outputs. However, a significant amount of power escapes, whether there is an IC or not, unless TC1 is used at the junction region. As depicted in the entire power density distributions, more symmetric and powerful patterns are obtained at the output tips when the junction coupler is used. These result demonstrate that TC1 can be used together with ICs to achieve an excellent transmission performance.

To further investigate TC1, an importance graph analysis is performed by examining the importance of each nanocube on the overall performance of the coupler, as it is done for an IC in Section 4.3.3. The graph in Figure 4.48 shows that the performance of the coupler is extremely affected by the particles close to the nanowire segments in the junction region. Changing only one bit and removing the corresponding two nanocubes (shown with “+” sign in the graph) result in 7.393 dB decrease in the mean power density and dimmed outputs as depicted in the power density distributions.

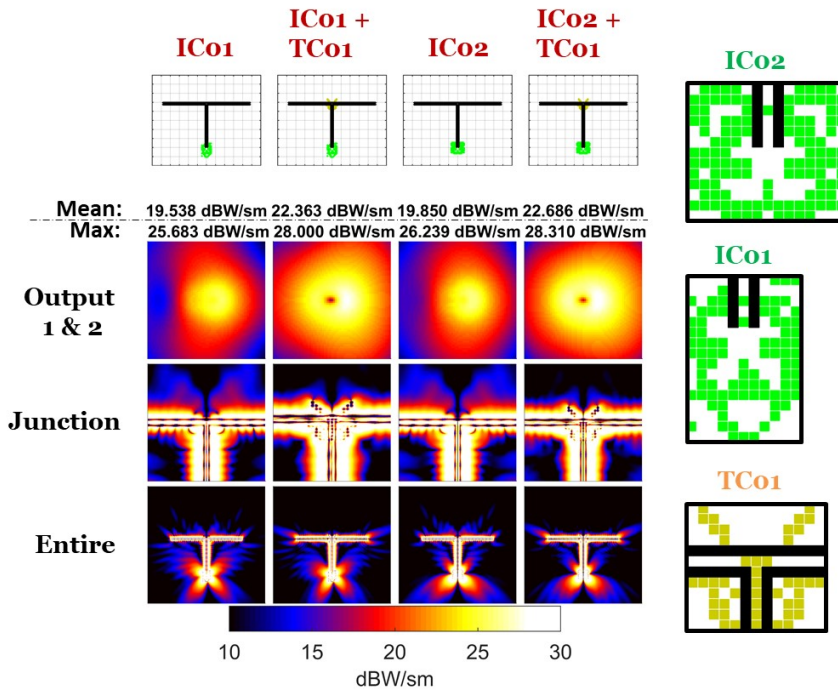


Figure 4.47: Performance of TC1 together with IC1 and IC2.

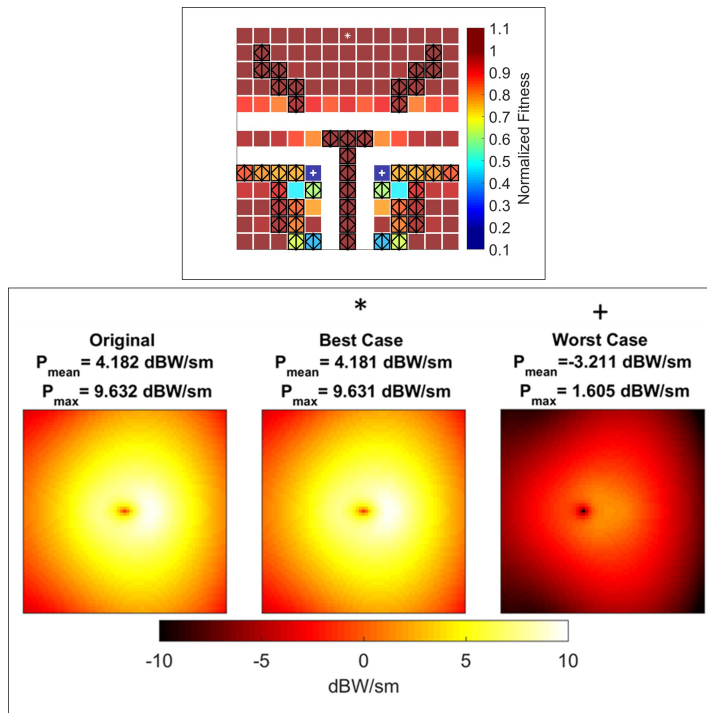


Figure 4.48: Importance graph for TC1. Power density distributions in one of the output frames are also shown for two modified couplers corresponding to the inversion of the least and most important bits, in comparison to the original case.

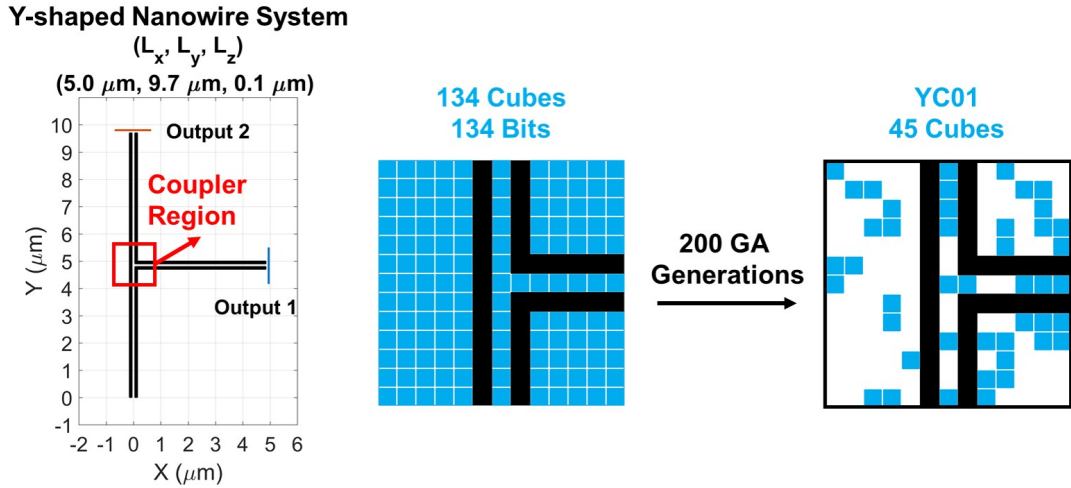


Figure 4.49: Y-shaped nanowire system involving a three-way junction with two differently oriented outputs. Full array layout used for the optimization of the junction coupler and the final design (YC1) are also shown.

4.6.3 Design of Couplers for a Three-way Junction with Two Differently Oriented Outputs

In this section, another coupler design is investigated for a nanowire system involving a three-way junction with two differently oriented outputs. As depicted in Figure 4.49, the nanowire system can be considered as a combination of three $5 \mu\text{m}$ segments to construct a transmission line from one input to two outputs oriented in perpendicular directions. Specifically, the coupler is designed to effectively transmit power from input nanowires equally towards nanowires in the same direction (y direction) and in the 90° direction (x direction). The balance for the power transmission to the outputs is achieved by using the cost function given in Equation 4.3. As the one used in the design of TC1, an 13×13 array containing 134 nanocubes is considered initially for the design of the coupler, and 200 generations are carried out to obtain the best distribution of the nanocubes such that the coupler equally divides electromagnetic power to the outputs. The initial layout and the final design for this Y-shaped junction coupler (YC1) are presented in Figure 4.49.

In Figure 4.50, power density distributions are again given for three different cases, i.e., no-coupler and full-array cases in addition to the YC-integrated case. As depicted

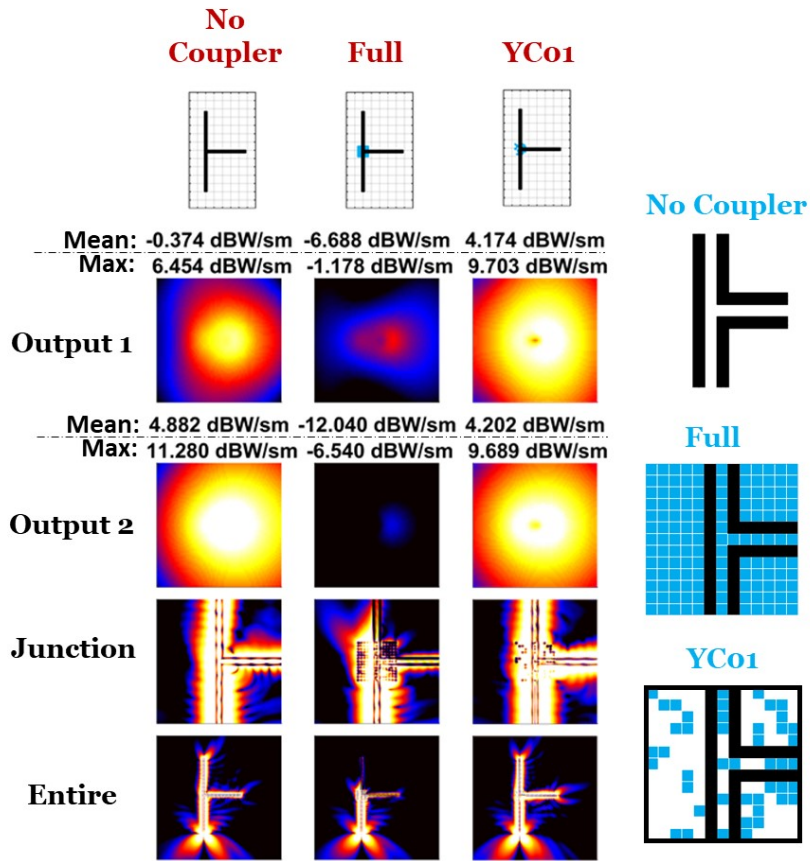


Figure 4.50: Performance of YC1 in comparison to the no-coupler and full-array cases. Power density distributions in three different frames and the geometries for all cases are shown.

in the no-coupler case, the plasmonic waves generated along the input segment are predominantly guided in the axial direction. As the significant inequality between the two outputs is clearly visible, output 2 has a mean power density of 4.882 dBW/m², which is approximately 5.2 dB larger than the one measured at output 1. Once YC1 is integrated, the difference between the power density values at the outputs is significantly minimized and similar power density distributions are achieved, which can be considered as a satisfactory result. It should be noted that this coupler is particularly designed to provide a balance between the powers transmitted to the outputs, i.e., the mean power density at one of the outputs decreases, while the other one increases when the coupler is integrated into the junction. The poor performance of the full array demonstrates the need for a well-designed coupler, as it is observed for all types of couplers.

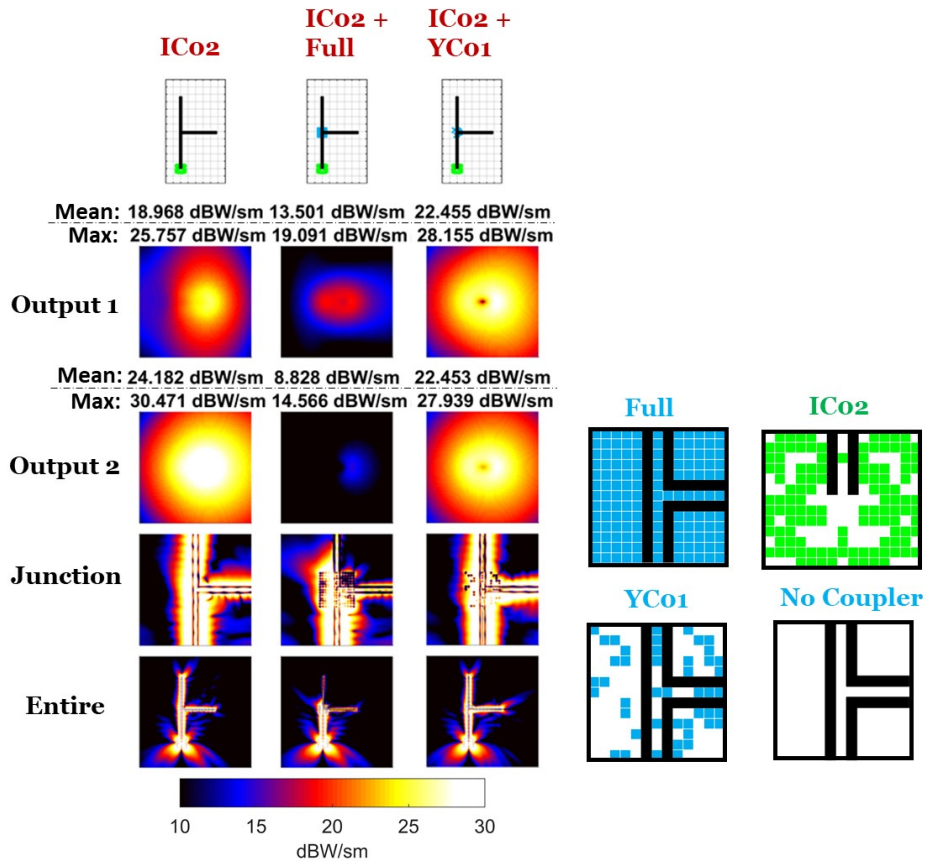


Figure 4.51: Performance of YC1 together with IC2.

In Figure 4.51, high compatibility of YC1 with ICs are presented, where IC2 is used as the IC to improve the overall power transmission. It is remarkable that the power density values at the outputs are significantly improved with the integration of IC2, while the balance between the outputs is provided by the use of YC1, whose excellent performance is not much affected by the integration of IC1.

Figure 4.52 presents the importance graph for YC1, which demonstrates that the performance of the coupler is highly sensitive to some of the elements, e.g., adding the particle shown with “+” sign results in significant deteriorations in the balance between the power density values at the two outputs.

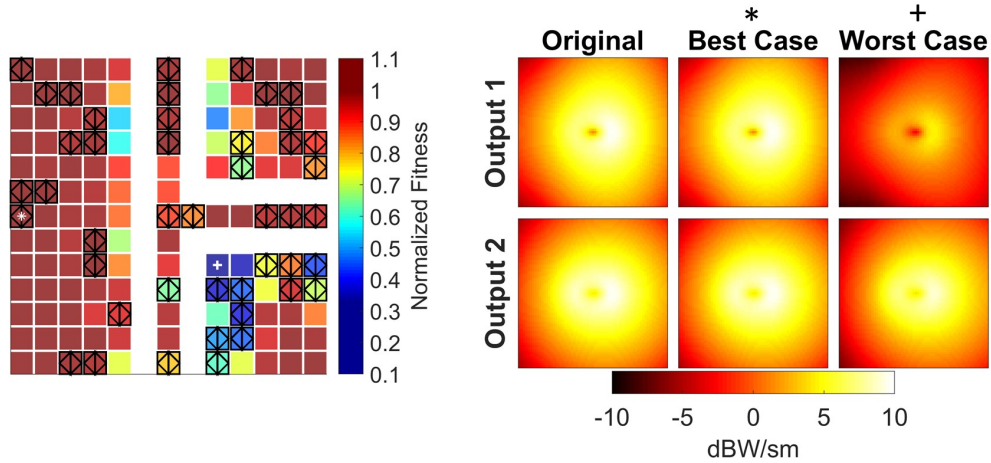


Figure 4.52: Importance graph for YC1. Power density distributions in the output frames are also shown for two modified couplers corresponding to the inversion of the least and most important bits, in comparison to the original case.

4.6.4 Design of Couplers for a Four-way Junction with Three Outputs

As the last coupler type for constructing nano-optical links, a coupler is designed for a nanowire system involving a four-way junction with three outputs. As illustrated in Figure 4.53, this nanowire system can be considered as a combination of four nanowire segments with 90° sharp bends. Hence, an efficient transfer of the power to the outputs requires a well-designed coupler, which can be called plus-shaped junction coupler (PC), to eliminate the power loss (due to reflections and diffractions) in the junction region. As in the designs of TC and YC, the coupler design is carried out to improve the power transmission to all outputs by adjusting the balance of the power levels. Using the cost function in Equation 4.3, an optimization trial is carried out by initially considering a layout for 125 bits. The final design (PC1) is depicted in Figure 4.53.

As demonstrated in Figure 4.54, using the designed coupler PC1, power levels at all outputs are significantly improved, while the differences between them are considerably minimized. Specifically, mean power density values of 1.721 dBW/m^2 , 1.737 dBW/m^2 , and 1.721 dBW/m^2 are achieved at outputs 1, 2, and 3, respectively. Moreover, the similarity of the output patterns can be seen in the power density distributions given for the output frames. It is remarkable that the propagation of the

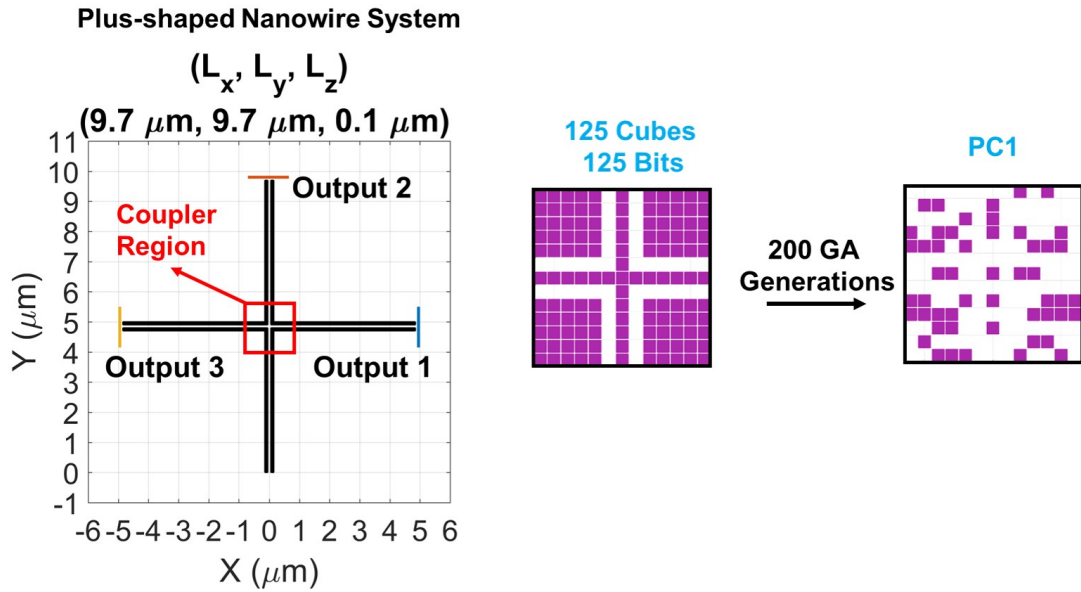


Figure 4.53: Plus-shaped nanowire system involving a four-way junction with three outputs. Full array layout used for the optimization of the junction coupler and the final design (PC1) are also shown.

plasmonic waves along the input segments is successfully manipulated by the coupler such that the electromagnetic power is transferred to all outputs as equal as possible. In Figure 4.55, the performance of PC1 is demonstrated when it is used together with an IC, i.e., IC2. As the results show, the power is equally delivered to the outputs, leading to a symmetric pattern thanks to the usage of PC1. It is also remarkable that the power density values in the output frames are not powerful when PC1 is not used. It can be stated that for efficient and well-balanced electromagnetic energy flow to all these outputs, both PC and IC should be used together.

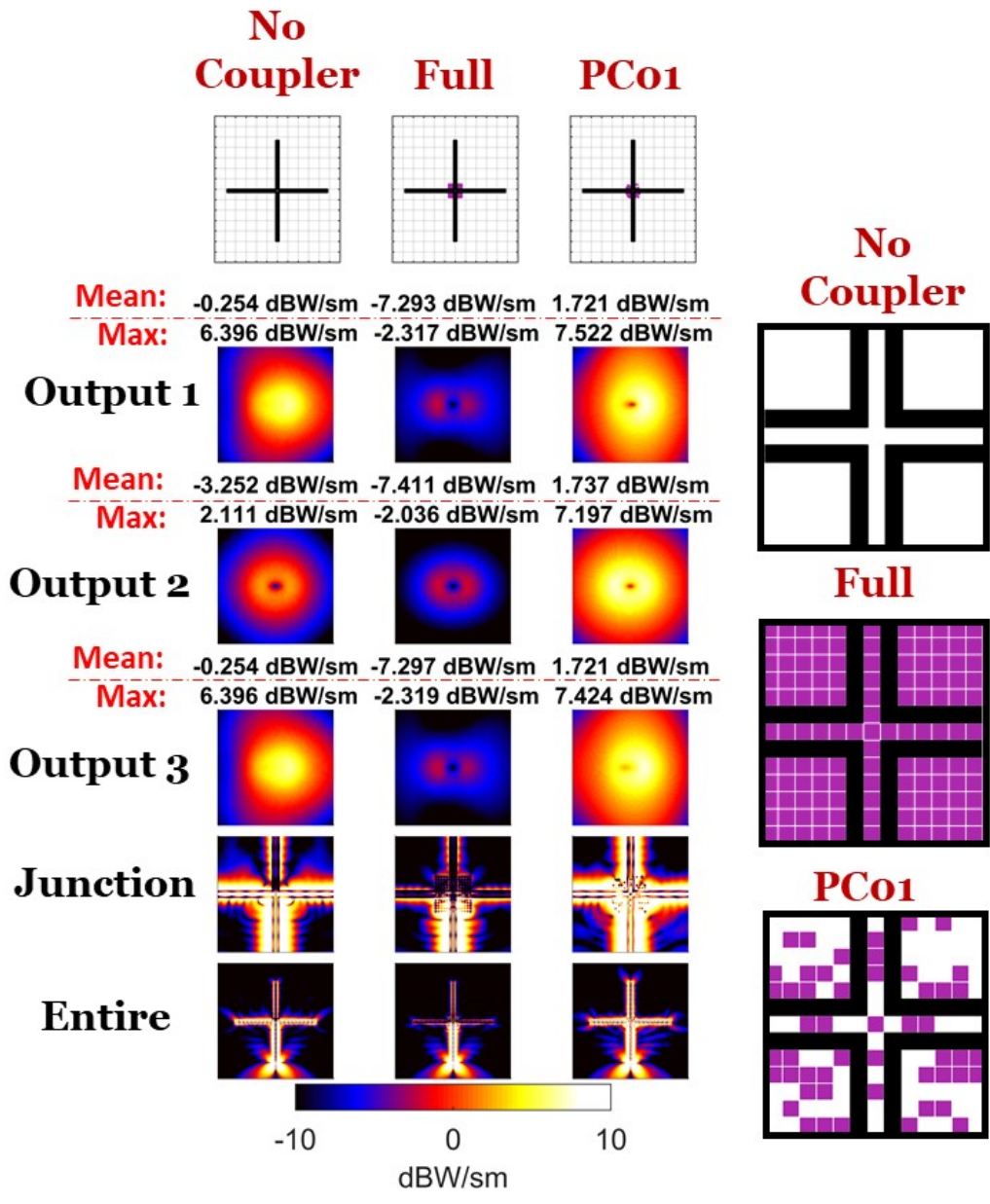


Figure 4.54: Performance of PC1 in comparison to the no-coupler and full-array cases. Power density distributions in three different frames and the geometries for all cases are shown.

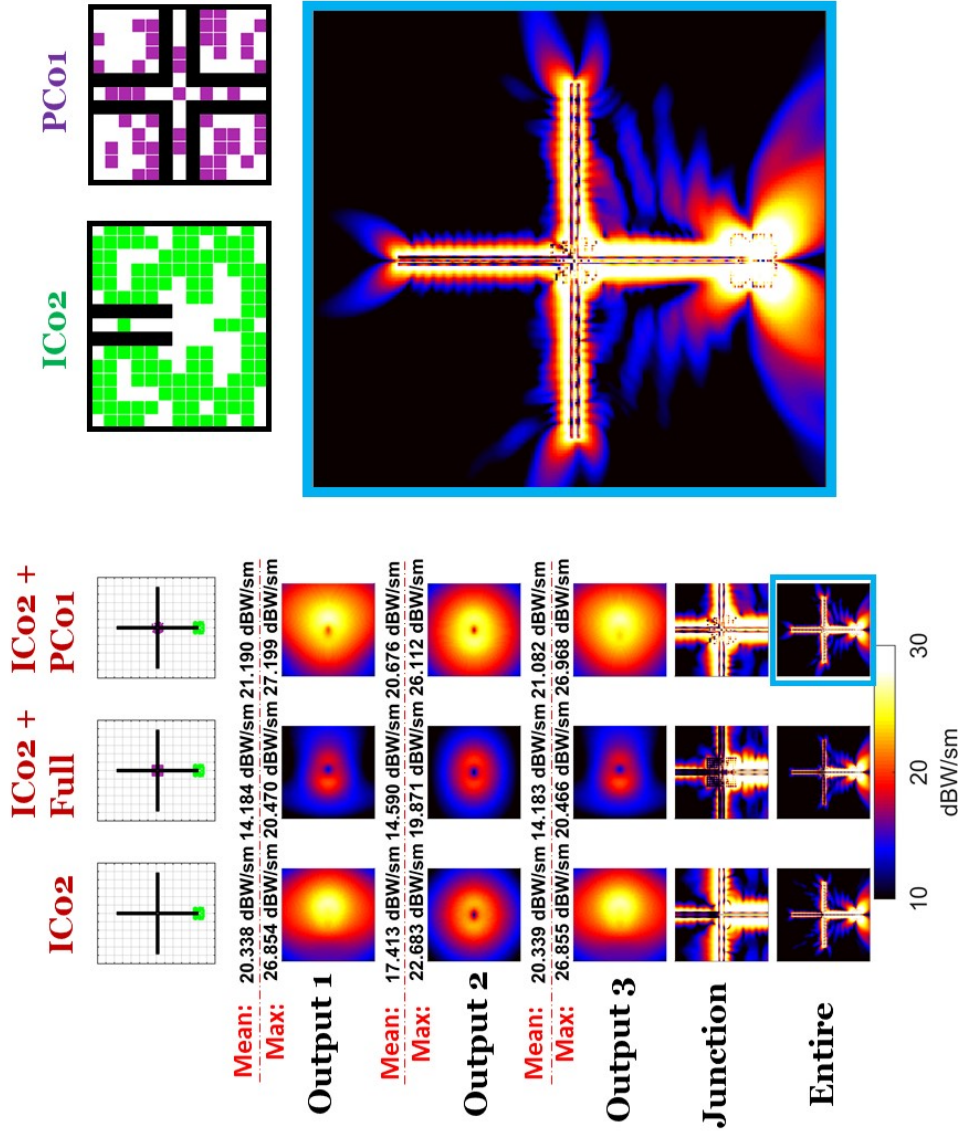


Figure 4.55: Performance of PC1 together with IC2. The power density distribution for the entire system involving both PC1 and IC2 is also shown.

4.7 Building Complex Nanowire Networks Involving Nanowires and Optimized Couplers

The efficiency and high performance of different types of couplers, i.e., ICs to increase the coupling between sources and nanowires, CCs to eliminate bending losses, and junction couplers to deliver electromagnetic energy from inputs to several outputs in well-balanced manners, are demonstrated in Section 4.3, Section 4.4, and Section 4.6, respectively. Moreover, in Section 4.5, it is shown that couplers designed for a specific case, such as ICs designed for straight nanowires, can be utilized to improve transmission abilities of other types nanowires, e.g., for bent nanowires. Based on these results, different types of couplers can be utilized to build large nano-optical systems involving connections of different types of nanowire segments together with suitable couplers. With the help of the designed couplers, electromagnetic energy flow through a large nano-optical system can be improved and an efficient power transfer can be achieved from the input to the desired output/outputs.

In this section, the designed couplers are employed to construct different types of nanowire networks. Different combinations of the couplers are studied in detail to understand the improvement provided by each coupler separately. By examining the results for different cases, we reach the rules and guidelines, which can be used to design different types of larger and more complex nanowire networks. The networks corresponding to the different scenarios presented in this section are excited by Hertzian dipoles at the operation frequency of 250 THz since the couplers are designed for this type of excitation. Performances of the couplers for different cases are examined by measuring the power density values in the measurement frames, which are placed 100 nm away from the nanowire tips, as usual. We particularly focus on couplers IC2 (Figure 4.11) , CC2 (Figure 4.19), TC1 (Figure 4.46), YC1 (Figure 4.50), and PC1 (Figure 4.54). The interpretations, guidelines, and the conclusions presented in this section are also obtained for other designs of couplers, such as IC1 and CC1, although they are not shown.

First, we consider an S-shaped system involving three $5 \mu\text{m}$ straight segments, as depicted in Figure 4.56. In this system, there are three separate regions for the integration of the designed couplers, i.e., an IC to the input and two CCs to the 90° sharp

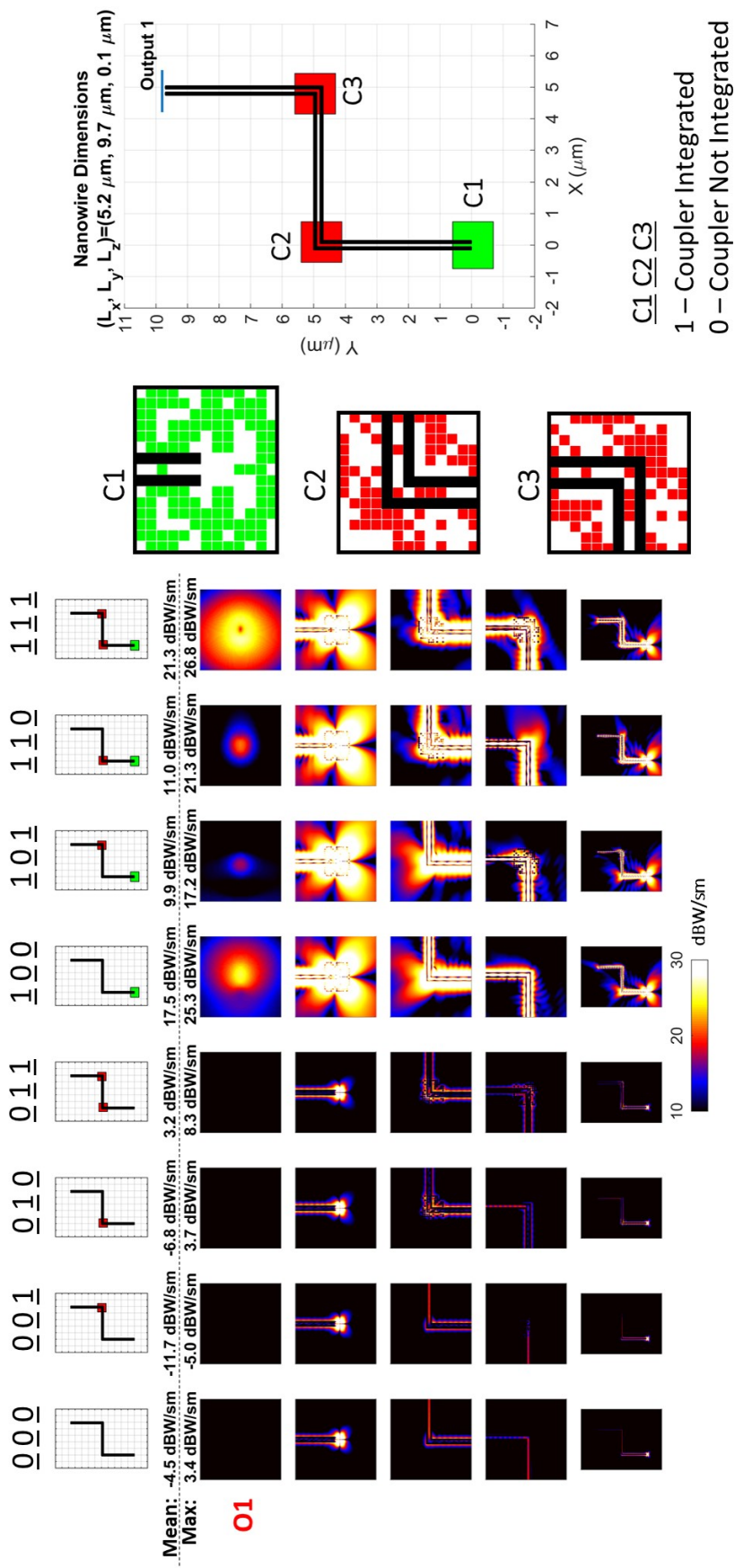


Figure 4.56: Results for the first nano-optical system. Power density distributions in different regions and in the output frame for different configurations of three couplers (IC2 and two CC2) are depicted. The geometry of the nanowire system and the used couplers are also shown.

corners with different orientations. Considering different combinations for the integration of one IC and two CCs into these regions, a total of eight different cases are examined. The power density distributions in different frames, which show the overall view, two corner regions, the input region, and the output region are also depicted in Figure 4.56. All plots are consistent with a [10,30] dBW/m² range for colors. Each case is labeled based on the names of the coupler regions, e.g., 000 corresponds to the no-coupler case and 111 corresponds to the case when all couplers are integrated. The geometries for all cases are also depicted in Figure 4.56. The efficiency of the couplers to improve the transmission ability can be understood by comparing the power density values achieved at the output for different cases. With the integration of all couplers into the corresponding coupler regions, the mean power density in the output frame increases from -4.5 dBW/m² to 21.3 dBW/m², which corresponds to more than 25 dBW/m² improvement with respect to the no-coupler case (000). A similar level of improvement is also obtained for the maximum power density, which increases from 3.4 dBW/m² to 26.8 dBW/m². When the results are examined further, it can be stated that very low power transmission levels are obtained if IC2 is not integrated into the input region. Even the use of only IC2 provides a significant increase in the power density values at the outputs, i.e., a mean power density of 17.5 dBW/m² is achieved for the 100 case in comparison to the value of -4.5 dBW/m² for the 000 case. On the other hand, a significant amount of escaping power from the corner regions occurs, unless both CC2 are integrated into the system, while the use of a single CC2 results in a significant deterioration in the output power. The best performance is obtained with the integration all couplers into necessary regions, for which an increase of 25.8 dBW/m² is obtained in the mean power density. To conclude, IC2 provides extreme improvements regardless of the existence of the other couplers, while further improvements can be achieved with the integration of the other couplers. For such a system involving multiple bends, all corner couples should be integrated into the necessary regions to achieve good transmission.

As the second example, a nanowire system involving four coupler regions is considered, as depicted in Figure 4.57. The system involves one input and two symmetrically located outputs. As the electromagnetic energy flow through this nanowire system, significant deteriorations occur in coupler region 2 (T-junction), as well as in

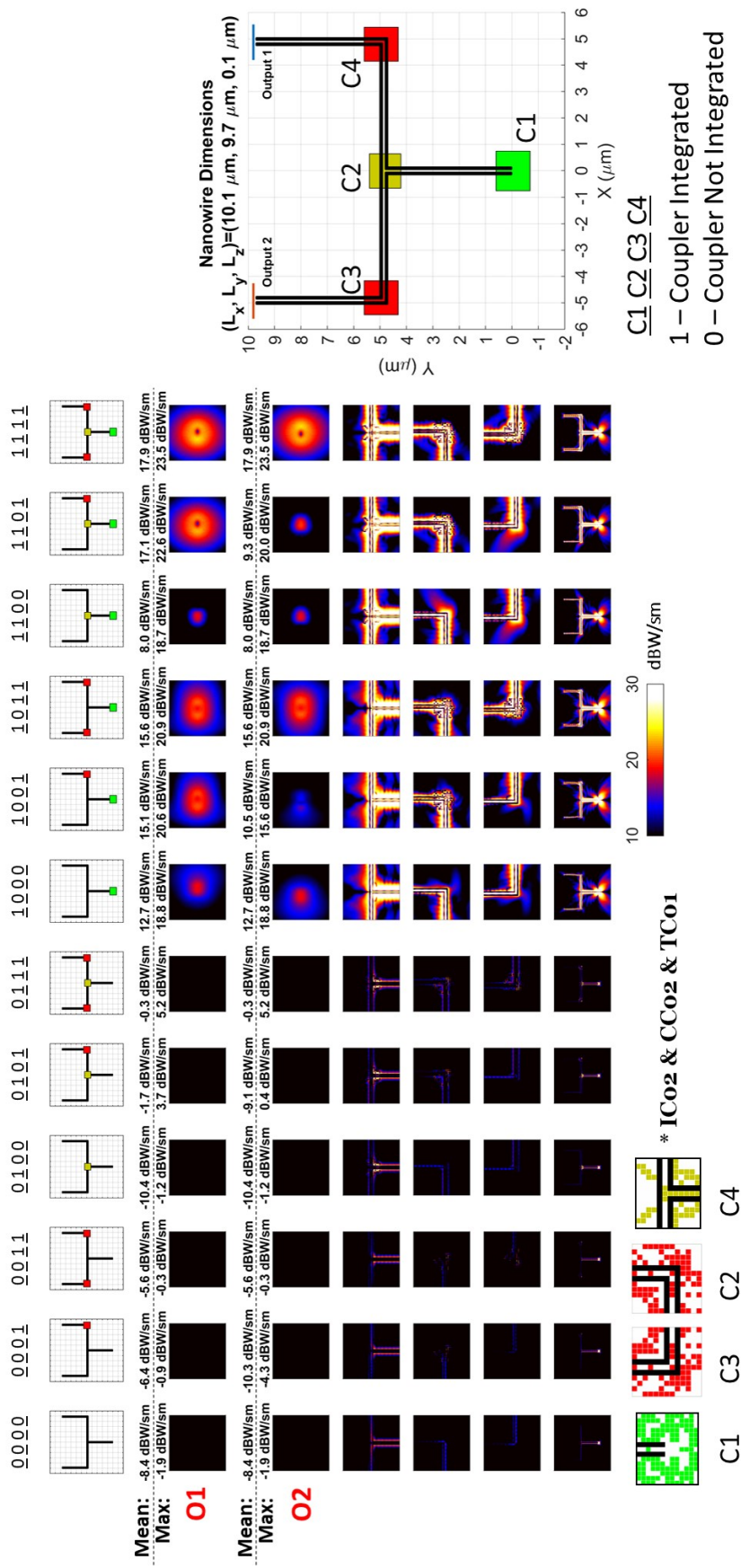


Figure 4.57: Results for the second nano-optical system. Power density distributions in different regions and in the output frames for different configurations of four couplers (IC2, TC1, and two CC2) are shown. The geometry of the nanowire system and the used couplers are also shown.

coupler regions 3 and 4 involving sharp bends. Considering the combinations for the integration of IC2, TC1, and two CC2 to the corresponding four coupler regions, a total of 12 cases are examined as given in Figure 4.57. According to the notation described above, the coupler combinations are represented by four bits, each of which corresponds to the existence of a coupler, e.g., 0000 corresponds to the no-coupler case and 1111 corresponds to the case when all couplers are integrated. As in the case of other nanowire systems, a major contribution to the output power is provided by IC2, while further improvements in terms of both balance and amplitude of the power transmission are provided by the use of other couplers. Specifically, the use of only IC2 increases the mean power density at both outputs from -8.4 dBW/m^2 (case 0000) to 12.7 dBW/m^2 (case 1000), while a further increase (approximately 5.2 dBW/m^2) is obtained once the other couplers are also integrated into the system (as the configuration changes from case 1000 to case 1111). In total, the couplers yield more than 26 dBW/m^2 improvement in the mean power density, while the maximum power density increases by nearly 25.7 dBW/m^2 . The working mechanism of the couplers can further be examined by comparing the integration of couplers in different scenarios, e.g., case 1000 and case 1100. As depicted in the figure, once TC1 is integrated into the nanowire system involving only IC2 (case 1100), the power density values at both outputs decrease, in comparison to case 1000. However, this does not mean that TC1 does not work properly for this nanowire system. On the contrary, as can be seen in the corner regions, with the integration of TC1, the amplitudes of the waves propagating along the segments of the T-junction are significantly improved, and the electromagnetic power arriving at the T-junction is guided towards the end of the segments to radiate into vacuum. As a result, the mean power density at the outputs deteriorates with the integration of TC1, since a significant amount of leakage occurs at the bends. Once the CCs are also integrated, however, the usage of TC1 provides a significant improvement in the mean power density at both outputs. This can be examined in more detail by comparing case 0111 with case 0011, which corresponds to the integration of coupler TC1 into the nanowire system involving CC2 at both bends. With the integration of TC1, the mean power density values at both outputs increase from -5.6 dBW/m^2 to -0.3 dBW/m^2 since bending losses are already reduced by the CCs. These observations lead to another rule and guideline for the building nano-optical links efficiently: Using a single coupler does not guarantee

an improvement for the overall power transmission since the efficiency of the system may be restricted by deficiencies at other regions and junctions. Hence, the performance of a coupler should be evaluated by comparing related cases, i.e., particularly when other parts of the system operate properly.

As the third example, the results and configurations corresponding to different cases are given in Figure 4.58 for a nanowire system involving three coupler regions and two outputs. Once again the best performance is achieved for the case that all couplers are integrated into the corresponding coupler regions. With the utilization of the couplers, the mean power density at output 1 and output 2 are improved by 29.6 dBW/m² and 25.6 dBW/m², respectively. It is remarkable that the power transmitted to the output, which initially has lower power density values, increases much more than the other one, leading to a balance between the outputs. Removing any of the couplers results in deterioration of both balance and levels of the power density values at the outputs, which demonstrates the efficiency and harmony of the couplers. It should be noted that the use of only YC1 without any other coupler significantly decreases the power transmitted to the outputs in comparison to the no-coupler case. Once CC2 is also integrated into the system, the performance of YC1 is revealed. This is because the deficiencies in the electromagnetic energy flow are eliminated by the use of CC2 such that YC1, which is optimized for a Y-shaped junction, can demonstrate its high performance.

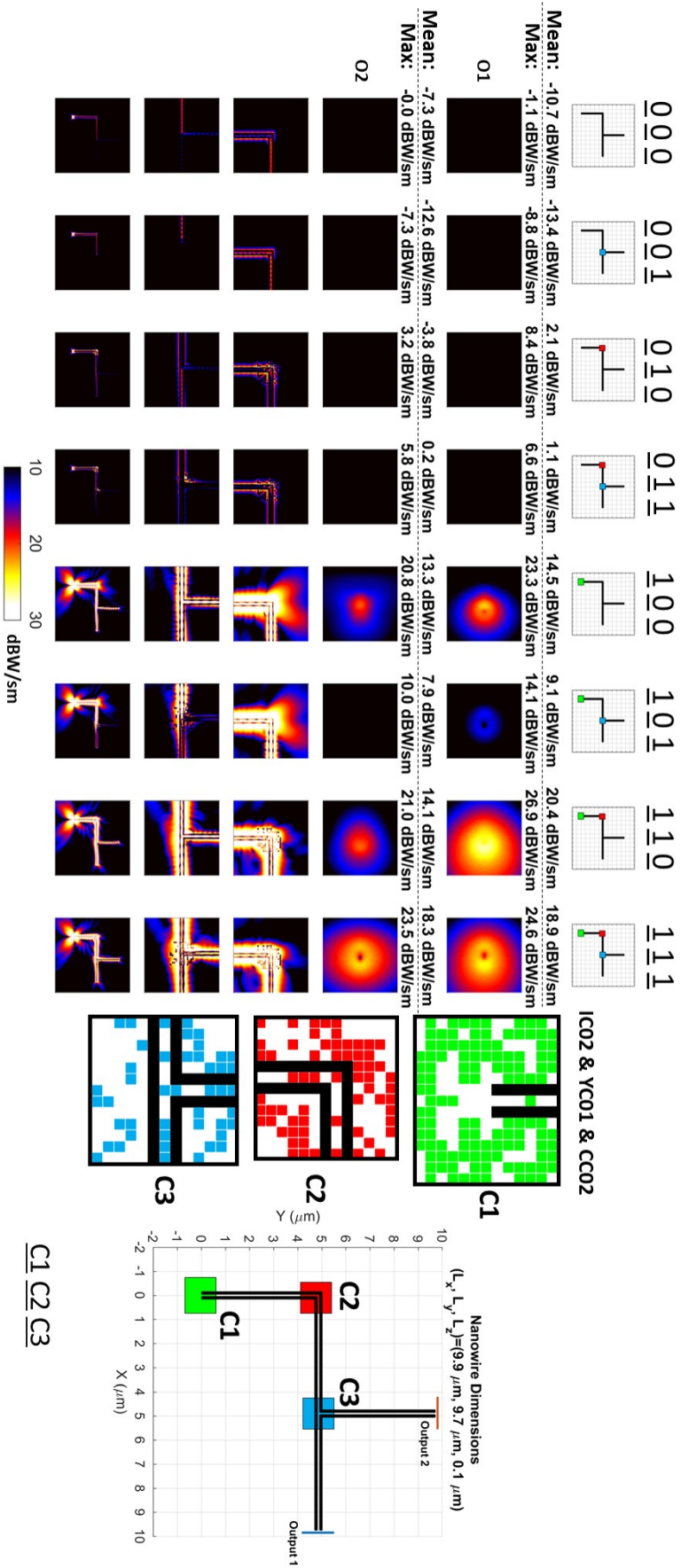


Figure 4.58: Results for the third nano-optical system. Power density distributions in different regions and in the output frames for different configurations of three couplers (IC2, YC1, and CC2) are shown. The geometry of the nanowire system and the used couplers are also shown.

The fourth example shown in Figure 4.59 involves a nano-optical system with five coupler regions that correspond to all coupler types investigated in the previous sections (IC, CC, TC, YC, and PC). In Figure 4.59, the power density distributions for five outputs and for the entire geometry are shown with eight different cases, including no-coupler (00000), all coupler (11111), and only-IC (10000) scenarios. In addition to these three cases, starting from the full geometry when all couplers are integrated, each coupler is removed one at a time and the corresponding analysis is performed to see the contribution provided by that coupler (01111, 10111, 11011, 11101, 11110). All plots are consistent with [10,30] dBW/m² ranges for colors. The results demonstrate the efficiency of the couplers to achieve good power transmission ability. The integration of all couplers to the corresponding regions results in improvements at all outputs, while the highest incrementation occurs at the output with the lowest power level initially. Specifically, the mean power density values at the outputs increase from [0.2, -15.1, -14.6, -14.8, 0.2] dBW/m² to [21.1, 10.8, 7.7, 8.2, 20.9] dBW/m². The individual contributions of the couplers to the overall response can be investigated by examining the corresponding cases involving the removal of each coupler individually from the full case. For example, when YC1 is removed from case 11111, the balance between outputs 3 and 4 is significantly destroyed, while the removal of PC1 results in a significant decrease in the mean power density values at all outputs. Similarly, when CC2 is extracted from the geometry of case 11111, a major decrease in the power density occurs at output 2 due to the increased bending losses. These results prove the significance of each coupler to the overall response of the nano-optical systems.

With the examples given in this section, it is demonstrated that, by efficiently connecting nanowires with the help of well-designed nano-couplers, it is possible to construct high-performance nano-optical systems with desired input/output locations. These initial examples and results show the feasibility of designing building blocks for nano-optical systems and even larger networks, where alternative coupler configurations can provide extensive control over power transmission. Some additional examples for six more nano-optical systems involving the designed couplers are given in Figures 4.60, 4.61, 4.62, 4.63, 4.64, and 4.65. It should be noted that, for each of these systems, power density distributions for four cases are presented and the final

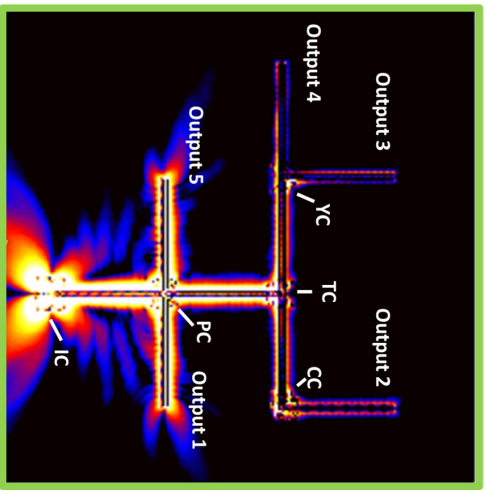
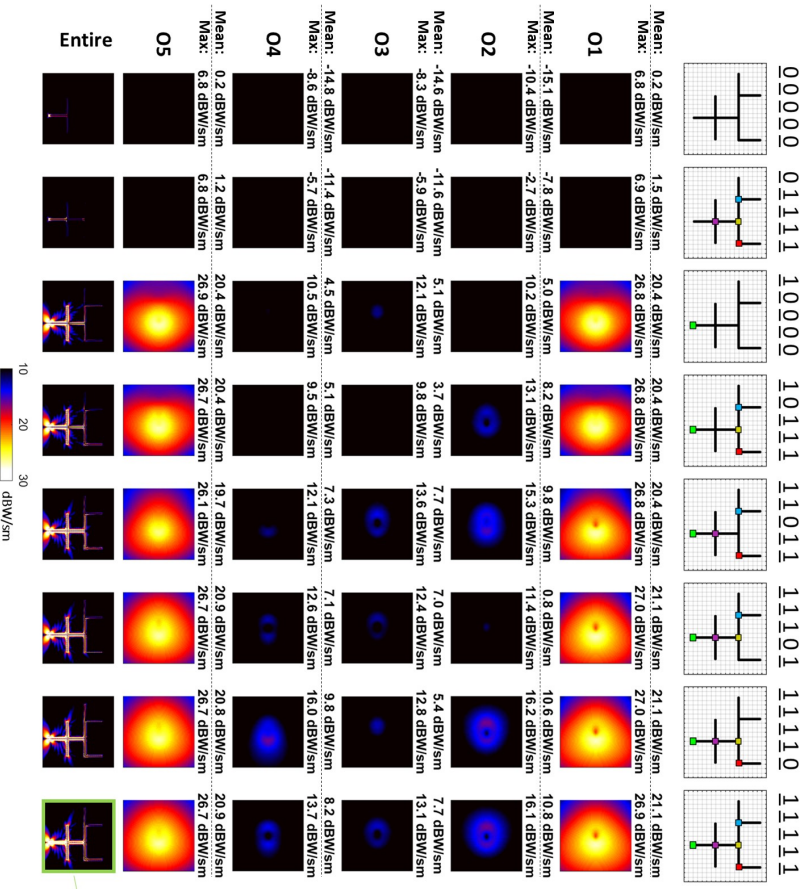


Figure 4.59: Results for the fourth nano-optical system. Power density distributions in different regions and in the output frames for different configurations of five couplers (IC2, YC1, PC1, TC1, and CC2) are shown. The entire system with the integration of all couplers is shown separately.

result obtained when all couplers are integrated is shown in detail. The coupler configurations used in the coupler regions are also depicted in the figures. Finally, for quantitative comparisons, the mean and maximum power density values are included for each output.

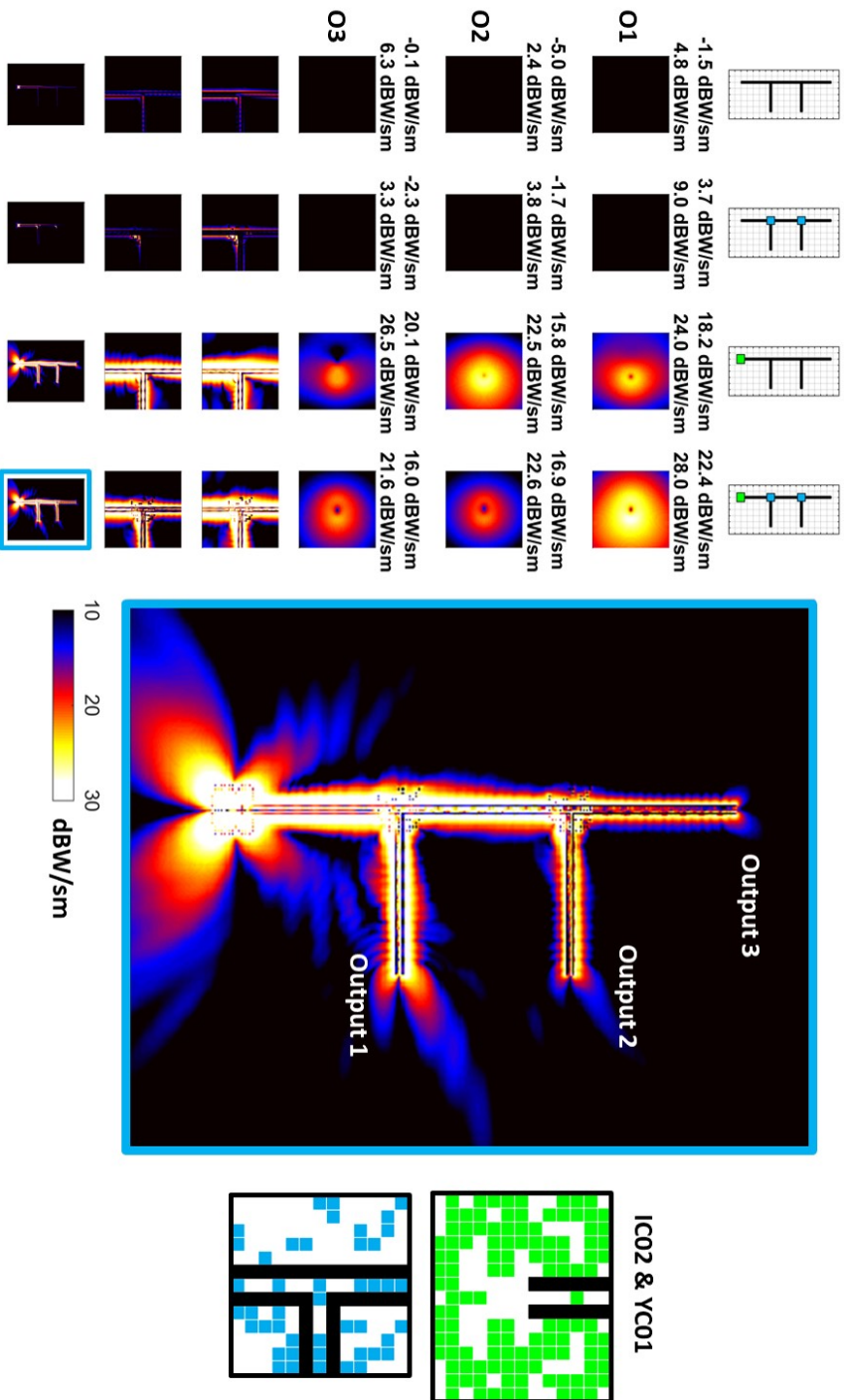


Figure 4.60: Results for the fifth nano-optical system. Power density distributions in different regions and in the output frames for different configurations of two couplers (IC2 and YC1) are shown. The entire system with the integration of both couplers is shown separately.

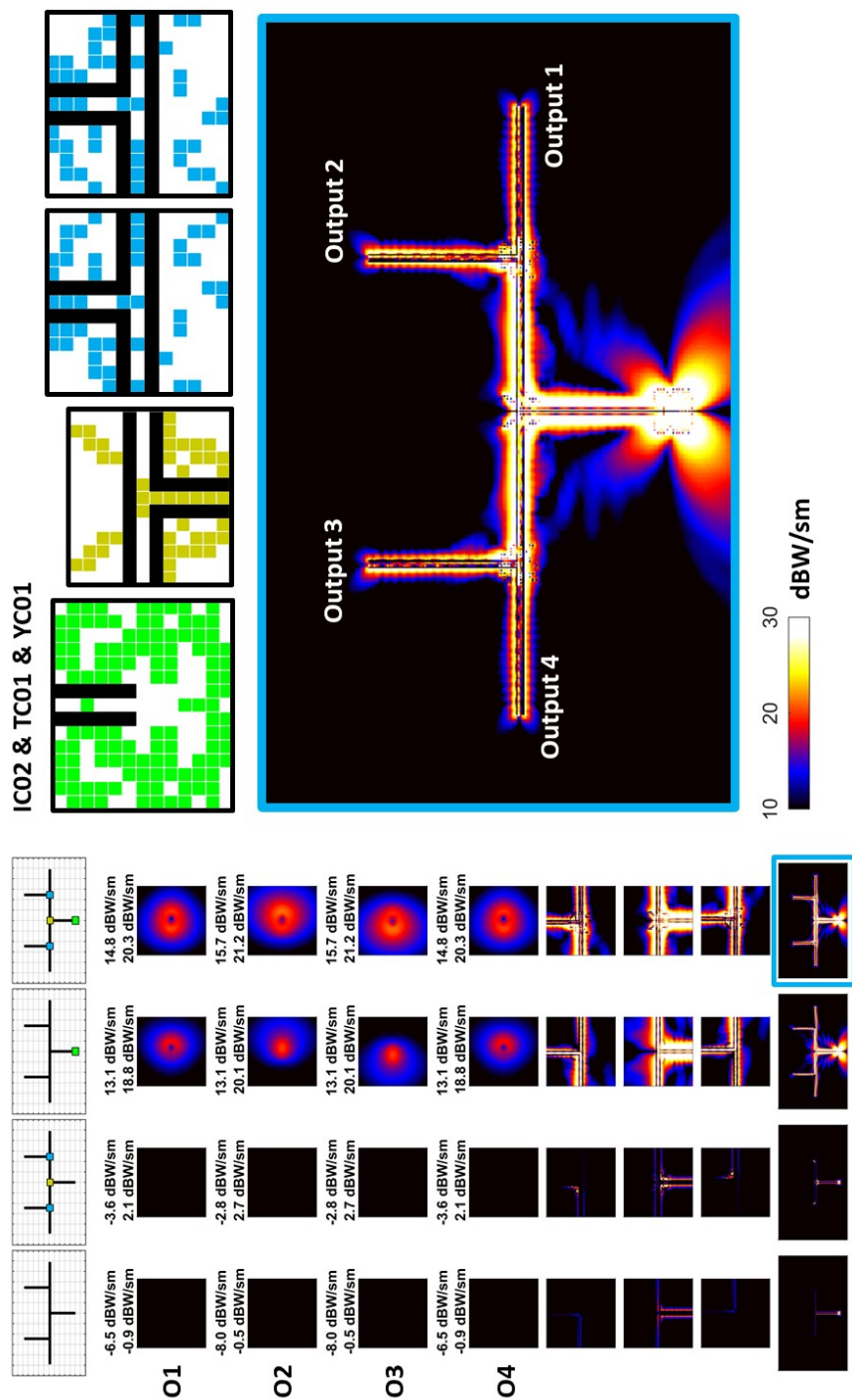


Figure 4.61: Results for the sixth nano-optical system. Power density distributions in different regions and in the output frames for different configurations of four couplers (IC2, TC1, and two YC1) are shown. The entire system with the integration of all couplers is shown separately.

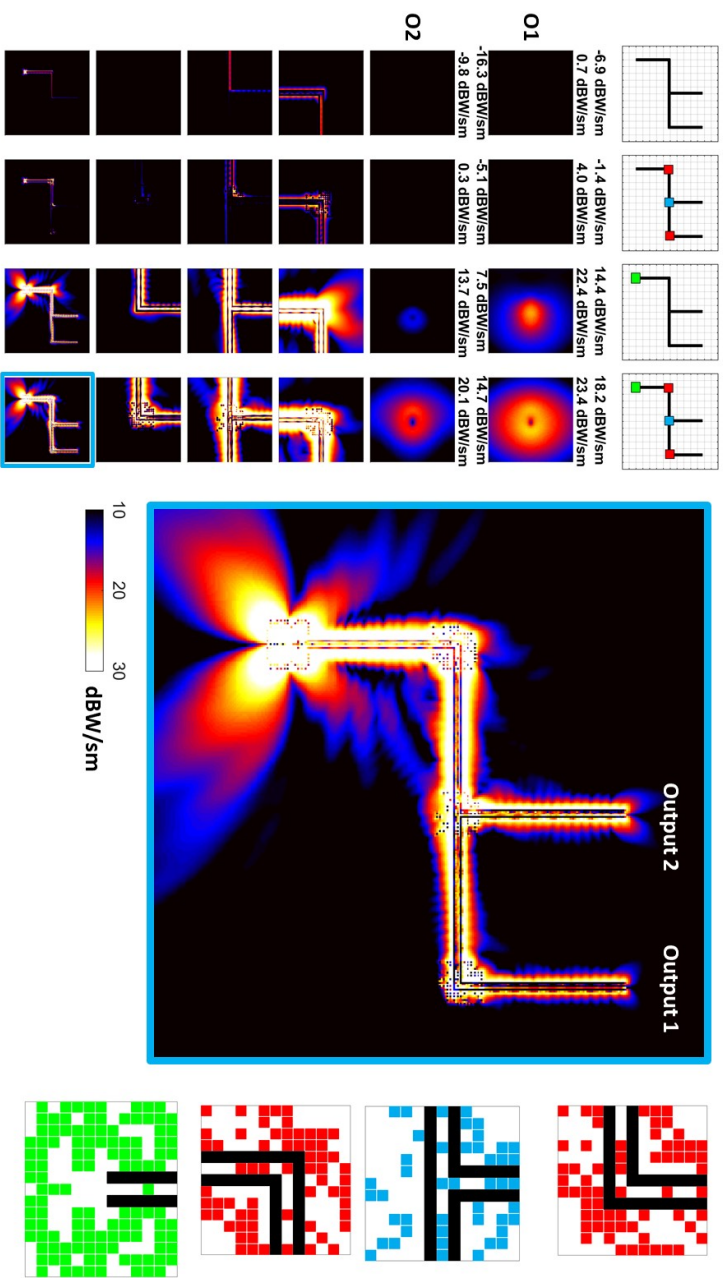


Figure 4.62: Results for the seventh nano-optical system. Power density distributions in different regions and in the output frames for different configurations of four couplers (IC2, YC1, and two CC2) are shown. The entire system with the integration of all couplers is shown separately.

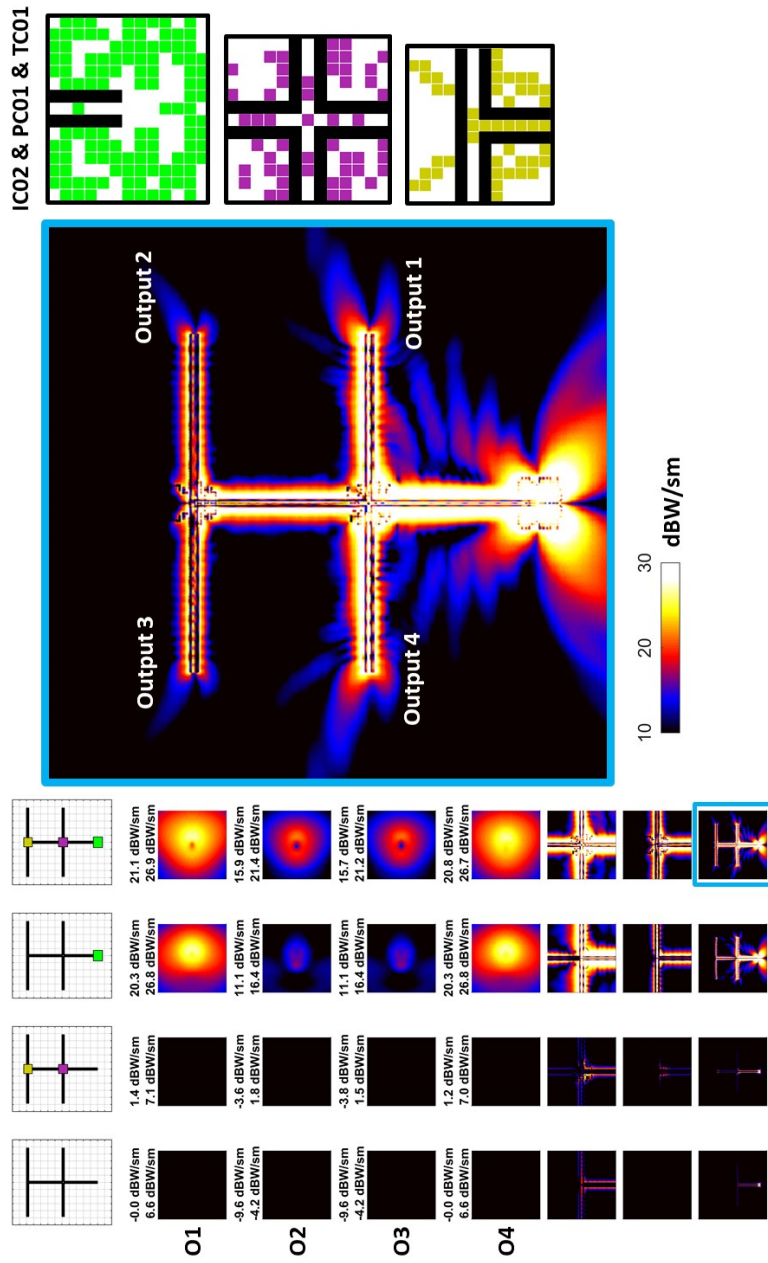


Figure 4.63: Results for the eighth nano-optical system. Power density distributions in different regions and in the output frames for different configurations of three couplers (IC2, PC1, and TC1) are shown. The entire system with the integration of all couplers is shown separately.

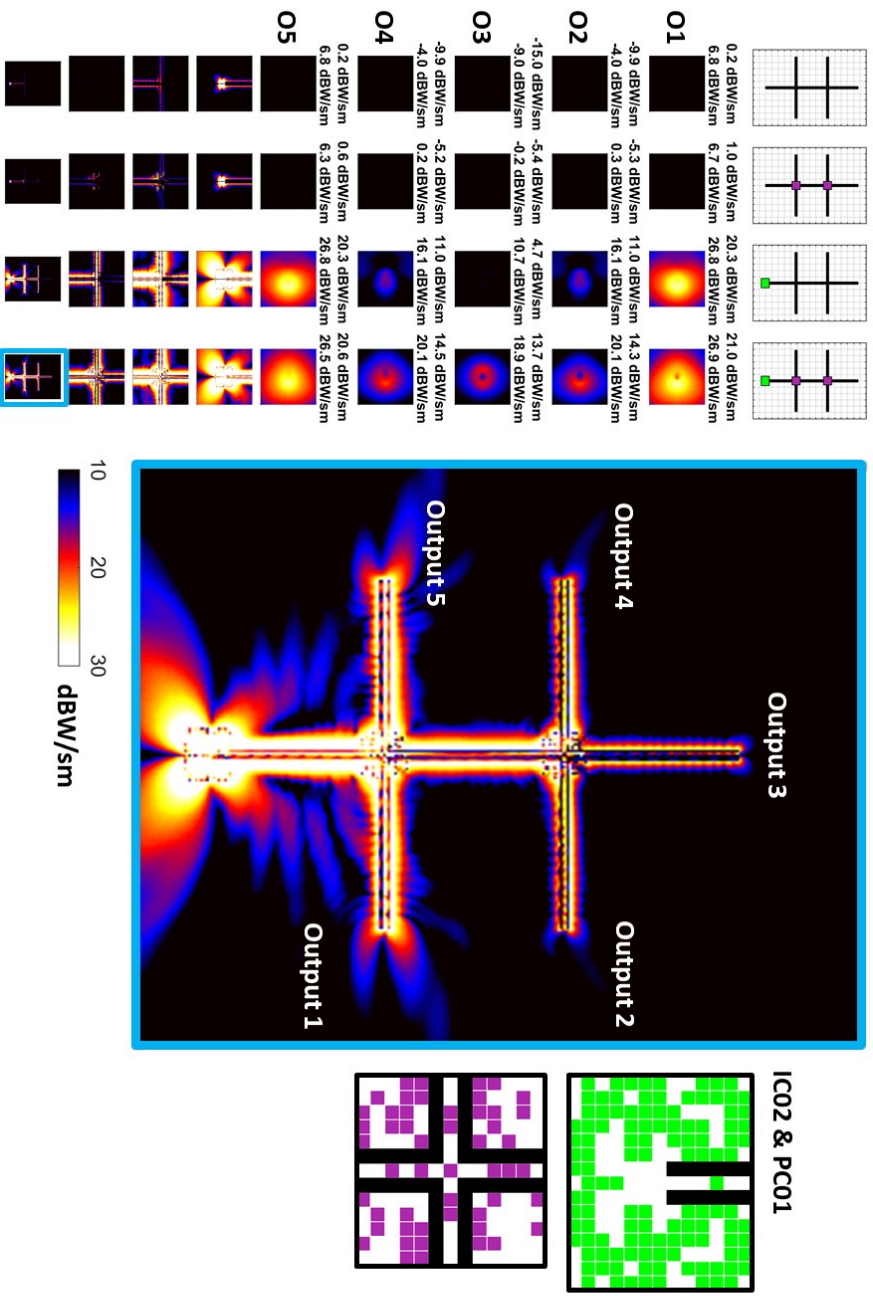


Figure 4.64: Results for the ninth nano-optical system. Power density distributions in different regions and in the output frames for different configurations of three couplers (IC2 and two PC1) are shown. The entire system with the integration of all couplers is shown separately.

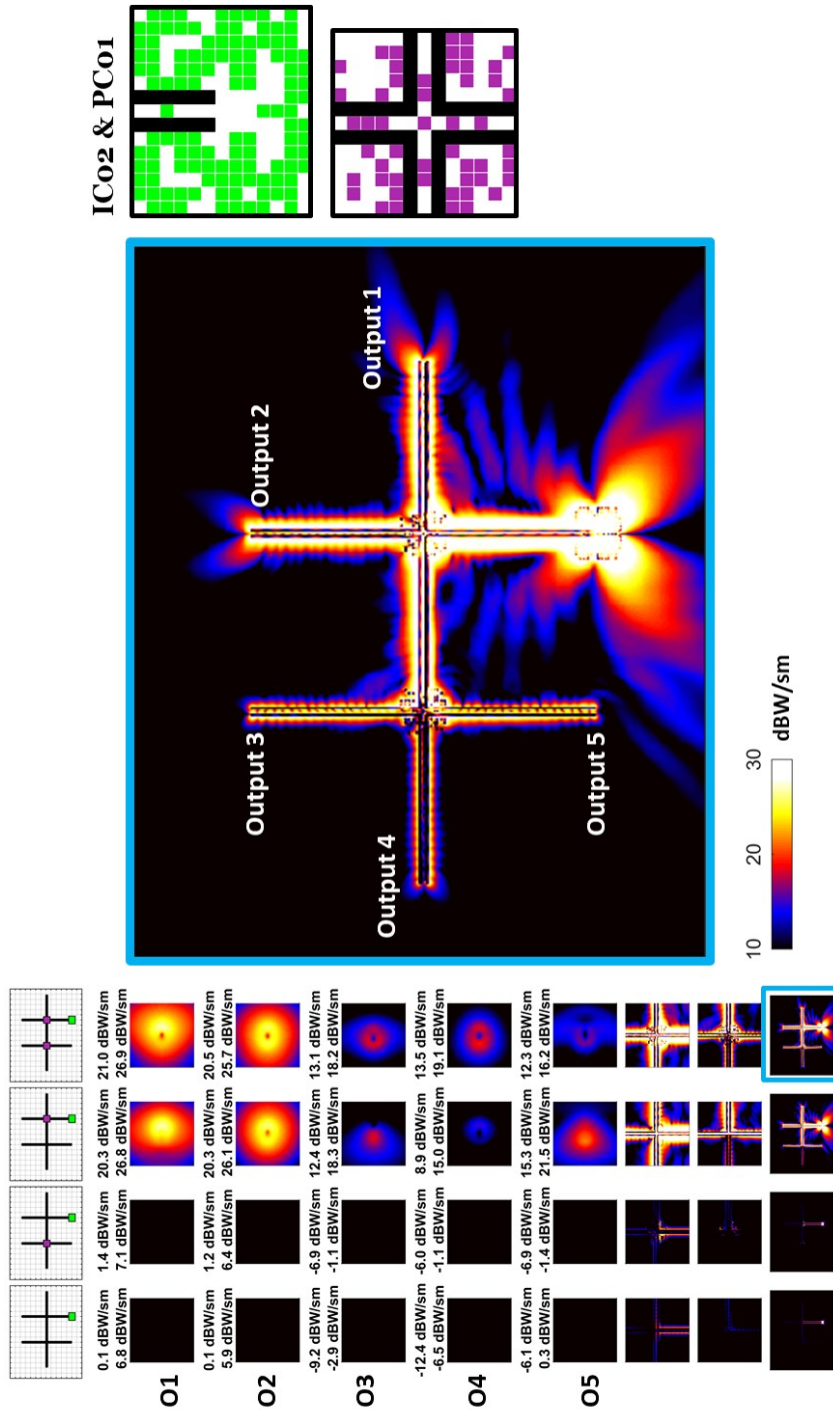


Figure 4.65: Results for the tenth nano-optical system. Power density distributions in different regions and in the output frames for different configurations of three couplers (IC2 and two PC1) are shown. The entire system with the integration of all couplers is shown separately.

4.8 Sensitivity Analysis for the Optimized Couplers

To investigate the tolerances of the couplers to undesired geometric faults that may occur during their fabrications, sensitivity analysis is performed for the couplers IC2, CC2, PC1, TC1, and YC1. For each coupler, three different scenarios are considered, i.e., surface corrugations, rotations of the particles around the x , y , and z axes, and misplacements of the particles with coordinate shifts in the x , y , and z directions. Consistency of the results is checked by performing two independent trials for each case. For the values of the shifts, corrugations, and rotations, Gaussian-distributed random variables are used, while the upper limits are restricted to avoid intersecting particles. The results presented in Tables 4.5, 4.6, 4.7, 4.8, and 4.9 demonstrate the robustness of the couplers to the geometric faults, i.e., the mean and maximum power density values at the outputs are generally very close to the ones obtained with the ideal couplers.

Table 4.5: The Results For the Sensitivity Analysis of IC2

	Output	Power Density	Original (dBW/sm)	Trial 1 (dBW/sm)	Trial 2 (dBW/sm)
Surface Corrugation	1	Mean	29.542	29.325	29.430
		Maximum	34.420	34.222	34.405
Particle Shift	1	Mean	29.542	29.707	29.213
		Maximum	34.420	34.626	34.150
Particle Rotation	1	Mean	29.542	29.676	29.670
		Maximum	34.420	34.566	34.558

Table 4.6: The Results For the Sensitivity Analysis of CC2

	Output	Power Density	Original (dBW/sm)	Trial 1 (dBW/sm)	Trial 2 (dBW/sm)
Surface Corrugation	1	Mean	7.160	7.093	6.969
		Maximum	12.026	12.023	11.715
Particle Shift	1	Mean	7.160	7.001	7.096
		Maximum	12.026	11.740	11.860
Particle Rotation	1	Mean	7.160	7.176	7.185
		Maximum	12.026	12.018	12.036

Table 4.7: The Results For the Sensitivity Analysis of YC1

	Output	Power Density	Original (dBW/sm)	Trial 1 (dBW/sm)	Trial 2 (dBW/sm)
Surface Corrugation	1	Mean	4.174	4.299	3.977
		Maximum	9.703	9.742	9.481
	2	Mean	4.202	4.353	3.759
		Maximum	9.689	9.833	9.295
Particle Shift	1	Mean	4.174	3.940	3.989
		Maximum	9.703	9.423	9.514
	2	Mean	4.202	4.797	4.442
		Maximum	9.689	10.216	9.926
Particle Rotation	1	Mean	4.174	4.182	4.166
		Maximum	9.703	9.707	9.708
	2	Mean	4.202	4.103	3.968
		Maximum	9.689	9.604	9.487

Table 4.8: The Results For the Sensitivity Analysis of TC1

	Output	Power Density	Original (dBW/sm)	Trial 1 (dBW/sm)	Trial 2 (dBW/sm)
Surface Corrugation	1	Mean	4.182	4.336	4.176
		Maximum	9.632	9.902	9.706
Particle Shift	1	Mean	4.182	4.472	4.158
		Maximum	9.632	10.019	9.742
Particle Rotation	1	Mean	4.182	4.135	4.148
		Maximum	9.632	9.597	9.614

Table 4.9: The Results For the Sensitivity Analysis of PC1

	Output	Power Density	Original (dBW/sm)	Trial 1 (dBW/sm)	Trial 2 (dBW/sm)
Surface Corrugation	1	Mean	1.721	1.763	1.134
		Maximum	7.522	7.463	6.641
	2	Mean	1.737	1.899	1.967
		Maximum	7.197	7.329	7.439
	3	Mean	1.721	1.723	1.945
		Maximum	7.424	7.476	7.697
Particle Shift	1	Mean	1.721	1.442	1.540
		Maximum	7.522	7.260	7.408
	2	Mean	1.737	0.660	1.626
		Maximum	7.197	6.222	7.221
	3	Mean	1.721	2.059	1.151
		Maximum	7.424	7.814	6.803
Particle Rotatation	1	Mean	1.721	1.813	1.797
		Maximum	7.522	7.601	7.566
	2	Mean	1.737	1.769	1.722
		Maximum	7.197	7.230	7.164
	3	Mean	1.721	1.760	1.817
		Maximum	7.424	7.373	7.396

4.9 Remarks

In this chapter, an optimization tool, which is an efficient and integrated combination of a heuristic optimization method (an implementation of GAs), and a full-wave solver based on surface integral equations and MLFMA, is used for rigorous designs of couplers involving nanoparticles to improve transmission abilities of complex nanowire networks with junctions and bends. The high-quality performances of the designed couplers are demonstrated for different parameters, such as grid size, frequency, particle shape, and dimensions. Significant advantages of the designed couplers against a classical approach in the literature, i.e., smoothing for bent nanowires, are presented. An efficient optimization strategy of division into sub-systems is demonstrated to improve power transmission in nanowire systems involving multiple coupler regions. Finally, the sensitivity of the designed couplers to various fabrication errors are examined in different scenarios, such as surface corrugation, particle shift, and particle rotation. All results demonstrate the feasibility of complex nano-optical networks that consist of nanowire segments and efficient couplers that can be useful in a plethora of applications.

CHAPTER 5

CONCLUSIONS

In this thesis, we present rigorous optimization and design of efficient couplers to improve power transmission in nano-optical networks that are built using nanowires. Detailed analyses of nano-optical couplers are provided by investigating different parameters in alternative scenarios. The designs are obtained via GAs, while the optimization trials are performed accurately and efficiently by using MLFMA. Nano-optical couplers are designed to generate desired responses in various cases, such as straight nanowires, bent nanowires, and nanowires involving junctions. In all these scenarios, excellent performances are provided by the designed couplers, in comparison to reference results obtained with only nanowires. The designed couplers are used to build electrically large and complex nano-optical systems and networks to demonstrate efficient power transfer from inputs to desired outputs. Based on optimization and computational test results, the main conclusions are as follows.

- Power transmissions along different types of plasmonic nanowires can significantly be improved by using well-designed couplers based on optimal arrangements of nanoparticles.
- A source for major losses in the transfer of electromagnetic energy in nanowire systems is the poor coupling between sources and nanowires. Electromagnetic energy coupled to nanowires can significantly be improved by using well-designed ICs at around sources and nanowire tips.
- Without a proper treatment, transmission abilities of bent nanowires are typically very limited due to reflections and diffractions at the bending regions. Symmetric patterns transferred along nanowires can also be destroyed due to such reflections and diffractions. These deficiencies can be eliminated by using

well-designed CCs at around sharp corners of nanowires, while the compactness of the overall system is preserved. Although the classical approach of curving bends can also improve the power transmissions along bent nanowires, the curvature radius must be very large (at the cost of reduced compactness) to compete with the designed couplers. In fact, despite their relatively small sizes, the designed couplers are so effective that curving within the coupler region does not further improve the power transmission ability.

- Electromagnetic energy flow through different types of junctions can also be controlled and improved by using well-designed couplers to efficiently transfer optical power from an input to desired output/outputs.
- Basically, increasing the number of nanoparticles leads to better coupler designs, while a saturation occurs after reaching a certain value. The optimum array layout for couplers can be chosen by considering the tradeoff between the compactness and performances of the couplers.
- The designed couplers maintain their performances for different nanowire lengths and they are robust against fabrication errors (different heights, surface corrugations, particle shifts, and particle rotations), while they are sensitive to the core geometry of particles.
- It is possible to design couplers with different particle shapes, while cubic particles provide the best results for compact regular arrangements in wide ranges of frequencies.
- Once designed, nanoparticles can be removed from a coupler to improve its compactness at the cost of the reduced performance. The best selections of nanoparticles to be removed can be based on an analysis of importance graph that is obtained by a post-processing on the design.
- Design of couplers depends on nanowires, i.e., the optimal design may change depending on the nanowire type and the existence of another coupler on the transmission line.
- For a given nanowire system, a simultaneous optimization of multiple couplers may not be necessary. Instead, couplers can be designed consecutively, i.e.,

once a coupler is optimized, it can be fixed on the transmission line while the other couplers are designed. If a coupler is designed individually considering a sub-system (as done in most of the designs in this thesis), the choice of the geometry of the nanowires can be critical. In most cases, it is useful to assume proper operations in the other parts of the super-system, e.g., assuming straight nanowires when designing ICs, while the best selection depends on the topology of the nano-optical network to be designed at the end.

- It is demonstrated that, by efficiently connecting nanowires with the help of the designed nano-couplers, it is possible to construct nano-optical systems with desired input/output locations. The examples and results show the feasibility of designing building blocks for nano-optical systems and even larger networks, where alternative coupler configurations can provide extensive control over power transmission.

Based on the results and conclusion of this thesis, constructing much larger nano-optical networks with the designed couplers remains as an exciting step to be considered in a future work.

REFERENCES

- [1] J. Takahara, S. Yamagishi, H. Taki, A. Morimoto, and T. Kobayashi, “Guiding of a one-dimensional optical beam with nanometer diameter,” *Optics Letters*, vol. 22, no. 7, pp. 475–477, 1997.
- [2] R. M. Dickson and L. A. Lyon, “Unidirectional plasmon propagation in metallic nanowires,” *The Journal of Physical Chemistry B*, vol. 104, no. 26, pp. 6095–6098, 2000.
- [3] K. Leosson, T. Nikolajsen, A. Boltasseva, and S. I. Bozhevolnyi, “Long-range surface plasmon polariton nanowire waveguides for device applications,” *Optics Express*, vol. 14, no. 1, pp. 314–319, 2006.
- [4] X. Wang, C. J. Summers, and Z. L. Wang, “Large-scale hexagonal-patterned growth of aligned ZnO nanorods for nano-optoelectronics and nanosensor arrays,” *Nano Letters*, vol. 4, no. 3, pp. 423–426, 2004.
- [5] A. W. Sanders, D. A. Routenberg, B. J. Wiley, Y. Xia, E. R. Dufresne, and M. A. Reed, “Observation of plasmon propagation, redirection, and fan-out in silver nanowires,” *Nano Letters*, vol. 6, no. 8, pp. 1822–1826, 2006.
- [6] H. Wei, D. Pan, S. Zhang, Z. Li, Q. Li, N. Liu, W. Wang, and H. Xu, “Plasmon waveguiding in nanowires,” *Chemical Reviews*, vol. 118, no. 6, pp. 2882–2926, 2018.
- [7] W. Wang, Q. Yang, F. Fan, H. Xu, and Z. L. Wang, “Light propagation in curved silver nanowire plasmonic waveguides,” *Nano Letters*, vol. 11, no. 4, pp. 1603–1608, 2011.
- [8] S. M. Bergin, Y.-H. Chen, A. R. Rathmell, P. Charbonneau, Z.-Y. Li, and B. J. Wiley, “The effect of nanowire length and diameter on the properties of transparent, conducting nanowire films,” *Nanoscale*, vol. 4, no. 4, pp. 1996–2004, 2012.

- [9] A. Yılmaz, B. Karaosmanoğlu, and Ö. Ergül, “Computational electromagnetic analysis of deformed nanowires using the multilevel fast multipole algorithm,” *Scientific Reports*, vol. 5, no. 8469, pp. 1996–2004, 2015.
- [10] H. Şatana, B. Karaosmanoğlu, and Ö. Ergül, “A comparative study of nanowire arrays for maximum power transmission,” in *Nanowires: New Insights* (K. Maaz, ed.), pp. 233–253, Intech, 2017.
- [11] P. Bharadwaj, A. Bouhelier, and L. Novotny, “Electrical excitation of surface plasmons,” *Physical Review Letters*, vol. 106, no. 22, p. 226802, 2011.
- [12] M. W. Knight, N. K. Grady, R. Bardhan, F. Hao, P. Nordlander, and N. J. Halas, “Nanoparticle-mediated coupling of light into a nanowire,” *Nano Letters*, vol. 7, no. 8, pp. 2346–2350, 2007.
- [13] A. V. Akimov, A. K. Mukherjee, C. L. Yu, D. E. Chang, A. S. Zibrov, P. R. Hemmer, H. Park, and M. D. Lukin, “Generation of single optical plasmons in metallic nanowires coupled to quantum dots,” *Nature*, vol. 450, pp. 402–406, 2007.
- [14] A. Huck and U. Andersen, “Coupling single emitters to quantum plasmonic circuits,” *Nanophotonics*, vol. 5, no. 3, pp. 483–495, 2016.
- [15] J. R. Krenn, B. Lamprecht, H. Ditlbacher, G. Schider, M. Salerno, A. Leitner, and F. R. Aussenegg, “Non-diffraction-limited light transport by gold nanowires,” *Europhysics Letters*, vol. 60, no. 5, pp. 663–669, 2002.
- [16] V. J. Sorger, R. F. Oulton, R.-M. Ma, and X. Zhang, “Toward integrated plasmonic circuits,” *MRS Bulletin*, vol. 37, no. 8, pp. 728–738, 2012.
- [17] Y. Tunçyürek, B. Karaosmanoğlu, and Ö. Ergül, “Computational design of optical couplers for bended nanowire transmission lines,” *Applied Computational Electromagnetics Society Journal*, vol. 32, no. 7, pp. 562–568, 2017.
- [18] H. Lange, B. H. Juárez, A. Carl, M. Richter, N. G. Bastús, H. Weller, C. Thomsen, R. von Klitzing, and A. Knorr, “Tunable plasmon coupling in distance-controlled gold nanoparticles,” *Langmuir*, vol. 28, no. 24, pp. 8862–8866, 2012.

- [19] W. Rechberger, A. Hohenau, A. Leitner, J. Krenn, B. Lamprecht, and F. Aussenegg, "Optical properties of two interacting gold nanoparticles," *Optics Communications*, vol. 220, no. 1, pp. 137–141, 2003.
- [20] C. Forestiere, A. J. Pasquale, A. Capretti, G. Miano, A. Tamburrino, S. Y. Lee, B. M. Reinhard, and L. Dal Negro, "Genetically engineered plasmonic nanoarrays," *Nano Letters*, vol. 12, no. 4, pp. 2037–2044, 2012.
- [21] Ö. Ergül and L. Gürel, *The Multilevel Fast Multipole Algorithm (MLFMA) for Solving Large-Scale Computational Electromagnetics Problems*. Wiley-IEEE Press, 2014.
- [22] R. F. Harrington, *Field Computation by Moment Methods*. Wiley-IEEE Press, 1993.
- [23] W. C. Gibson, *The Method of Moments in Electromagnetics*. Chapman and Hall/CRC, 2007.
- [24] S. Rao, D. Wilton, and A. Glisson, "Electromagnetic scattering by surfaces of arbitrary shape," *IEEE Transactions on Antennas and Propagation*, vol. 30, no. 3, pp. 409–418, 1982.
- [25] R. Coifman, V. Rokhlin, and S. Wandzura, "The fast multipole method for the wave equation: a pedestrian prescription," *IEEE Antennas and Propagation Magazine*, vol. 35, no. 3, pp. 7–12, 1993.
- [26] V. Rokhlin, "Rapid solution of integral equation of scattering theory in two dimensions," *Journal of Computational Physics*, vol. 86, no. 2, pp. 414–439, 1989.
- [27] J. Song, C.-C. Lu, and W. C. Chew, "Multilevel fast multipole algorithm for electromagnetic scattering by large complex objects," *IEEE Transactions on Antennas and Propagation*, vol. 45, no. 10, pp. 1488–1493, 1997.
- [28] B. Karaosmanoğlu, A. Yılmaz, and Ö. Ergül, "A comparative study of surface integral equations for accurate and efficient analysis of plasmonic structures," *IEEE Transactions on Antennas and Propagation*, vol. 65, no. 6, pp. 3049–3057, 2017.

- [29] B. Karaosmanoğlu, A. Yılmaz, U. M. Gür, and Ö. Ergül, “Solutions of plasmonic structures using the multilevel fast multipole algorithm,” *International Journal of RF and Microwave Computer-Aided Engineering*, vol. 26, no. 4, pp. 335–341, 2016.
- [30] C. Önoğlu, B. Karaosmanoğlu, and Ö. Ergül, “Efficient and accurate electromagnetic optimizations based on approximate forms of the multilevel fast multipole algorithm,” *IEEE Antennas and Wireless Propagation Letters*, vol. 15, pp. 1113–1115, 2016.
- [31] W. C. Chew, E. Michielssen, J. Song, and J.-M. Jin, *Fast and Efficient Algorithms in Computational Electromagnetics*. Artech House, 2001.
- [32] C. Forestiere, A. J. Pasquale, A. Capretti, G. Miano, A. Tamburrino, S. Y. Lee, B. M. Reinhard, and L. Dal Negro, “Genetically engineered plasmonic nanoarrays,” *Nano Letters*, vol. 12, no. 4, pp. 2037–2044, 2012.
- [33] G. Karaova, A. Altınoklu, and Ö. Ergül, “Full-wave electromagnetic optimization of corrugated metallic reflectors using a multigrid approach,” *Scientific Reports*, vol. 8, no. 1267, 2018.
- [34] A. Altınoklu and Ö. Ergül, “Computational analysis and full-wave optimizations of nanoantenna arrays for desired scattering and radiation characteristics,” in *2017 XXXIInd General Assembly and Scientific Symposium of the International Union of Radio Science (URSI GASS)*, 2017.
- [35] R. L. Johnston, “Evolving better nanoparticles: genetic algorithms for optimizing cluster geometries,” *Dalton Transactions*, pp. 4193–4207, 2003.
- [36] J. M. Johnson and Y. Rahmat-Samii, “Genetic algorithms in engineering electromagnetics,” *IEEE Antennas and Propagation Magazine*, vol. 39, no. 4, pp. 7–21, 1997.
- [37] D. S. Weile and E. Michielssen, “Genetic algorithm optimization applied to electromagnetics: a review,” *IEEE Transactions on Antennas and Propagation*, vol. 45, no. 3, pp. 343–353, 1997.

- [38] A. Hoorfar, “Evolutionary programming in electromagnetic optimization: A review,” *IEEE Transactions on Antennas and Propagation*, vol. 55, no. 3, pp. 523–537, 2007.
- [39] D. Zingg, M. Nemeč, and T. Pulliam, “A comparative evaluation of genetic and gradient-based algorithms applied to aerodynamic optimization,” *European Journal of Computational Mechanics/Revue Européenne de Mécanique Numérique*, vol. 17, no. 1, 2008.
- [40] R. Haupt, “Comparison between genetic and gradient-based optimization algorithms for solving electromagnetics problems,” *IEEE Transactions on Magnetics*, vol. 31, no. 3, pp. 1932–1935, 1995.
- [41] D. E. Goldberg, *Genetic Algorithms in Search, Optimization and Machine Learning*. Addison-Wesley, 1989.
- [42] C. Önoł, “Optimizations of antennas using heuristic algorithms supported by the multilevel fast multipole algorithm,” Master’s thesis, Middle East Technical University, September 2015.
- [43] K. E. Kinnear, Jr., ed., *Advances in Genetic Programming*. MIT Press, 1994.
- [44] P. B. Johnson and R. W. Christy, “Optical constants of the noble metals,” *Physical Review B*, vol. 6, pp. 4370–4379, 1972.
- [45] K. Vahala, “Optical microcavities,” *Nature*, vol. 424, pp. 839–846, 2003.
- [46] H. Wei, Z. Wang, X. Tian, M. Käll, and H. Xu, “Cascaded logic gates in nanophotonic plasmon networks,” *Nature Communications*, vol. 2, p. 387, 2011.
- [47] D. J. Dikken, M. Spasenović, E. Verhagen, D. Oosten, and L. Kuipers, “Characterization of bending losses for curved plasmonic nanowire waveguides,” *Optics Express*, vol. 18, no. 15, pp. 16112–16119, 2010.
- [48] H. Yu, S. Wang, J. Fu, M. Qiu, Y. Li, F. Gu, and L. Tong, “Modeling bending losses of optical nanofibers or nanowires,” *Applied Optics*, vol. 48, no. 22, pp. 4365–4369, 2009.